

**Exploration of the Effects of Electrospray Deposition Spraying  
Parameters and Incident Laser Wavelength on Matrix Assisted  
Laser Desorption Ionization Time-of-Flight Mass Spectrometry**

A Thesis

Submitted to the Faculty

of

Drexel University

by

Jonathan R. Haulenbeek

in partial fulfillment of the

requirements for the degree

of

Doctor of Philosophy

May 2012

©Copyright 2012

Jonathan R. Haulenbeek. All Rights Reserved.

## Acknowledgements

I thank my thesis committee members from Drexel University; Dr. Peter Wade, Dr. Joe Foley, Dr. Reinhard Schweitzer-Stenner, Dr. Frank Ji, and Dr. Daniel King for their support and guidance. I also thank Dr. Catherine Bentzely, from the University of the Sciences, Philadelphia, for being a part of my thesis committee and for her enthusiasm and support. I thank Wolfgang Nadler, Maryann Fitzpatrick and Tim Wade, from Drexel University for their technical guidance and help during tenure at Drexel. I also thank all other faculty and staff that I have interacted with at Drexel University.

I thank Bristol-Myers Squibb Company (BMS) for their financial support. Specifically, I thank Dr. John Wasyluk and Dr. Anne Kelly of BMS for their encouragement and invaluable insights, without which I may not have chosen this path. I also thank Dr. Stephen Sckypinski, Dr. Mark Powell, Dr. Binodh Desilva, Dr. John Grosso and Dr. Pankaj Shah for their support and guidance.

I thank all the current and past graduate students I have interacted with at Drexel, especially Dr. Christopher Castillo, Nicholas Papariodamis, and Arben Kojtari for stimulating scientific conversations and helping me to stay sane during my journey toward a doctorate degree. Their friendship and support has been invaluable. I also thank Francsico Guevara for his contributions to the work described in Chapter 6.

I thank the current and past group members who I have interacted with; Dr. Renata Szyszka, Andy Mahan, Runbo Li, Dr. Bill Erb and Dr. Drew Hoetling for their guidance and support. I especially thank Dr. April Holcomb for her friendship and support during my first years in the group. Her knowledge and sense of humor were invaluable during my transition into the research group.

I thank Dr. Gary Kinsel and Dr. Richard Knochenmuss for their enthusiasm toward my research projects and their guidance and insight. I thank John Pratt, from Buker Daltonics, for providing me with instrumentation that allowed for key finding during my research. I thank Fred Poelzing, from Keyence, for donating his time and expertise that enabled key measurements presented in Chapter 4.

I thank my family for their unwavering support and encouragement over the years. To my parents, Bob and Carol Haulenbeek, thank you for supporting my dreams and believing in me. I also thank my grandmother, Edna Haulenbeek, though she is unable to share in this accomplishment, her endless encouragement and support will never be forgotten. Finally, I especially thank my wife, Andrea, and son, Kyan, for their unconditional love and support. At my darkest hours, you were both there to put a smile on my face and provide the extra encouragement needed to move forward. I would not have made it through this journey without you.

Lastly, I thank my advisor, Dr. Kevin Owens, for his guidance and patience through the years. I would not be the scientist I am today without his tutelage. I entered his group with an idea about what I wanted to study and he allowed me to shape my own research. In this manner, and with his valuable input, I learned how to design meaningful experiments and objectively interpret their results. I also thank him for the intriguing and informative scientific discussions.

## Table of Contents

List of Tables .....	vii
List of Figures .....	viii
Abstract .....	xiv
Chapter 1. Introduction and Overview .....	1
MALDI-TOFMS .....	1
Organization of the Thesis .....	3
References .....	4
Chapter 2. Experimental .....	6
Introduction .....	6
Instrumentation .....	6
Bruker AutoFlex III MALDI TOF .....	6
Bruker Reflex III MALDI TOF .....	7
Atomic Force Microscope .....	9
3D Laser Scanning Confocal Microscope .....	10
UV/Visible Absorption Spectrophotometer .....	10
SpeedVac™ Concentrator .....	10
Quartz Crystal Microbalance .....	11
Scanning Electron Microscope .....	11
Statistical Analyses .....	11
Sample Deposition Methods .....	11
Dry Drop Method .....	11
Electrospray Deposition Method .....	11
Materials .....	14
MALDI Matrix Materials .....	14
Analytes .....	15
Solvents .....	15
Chapter 3. Description and Characterization of Electrospray Deposition as used for the Preparation of MALDI-TOFMS Samples .....	17
Introduction .....	17
Spraying Modes .....	19

Experimental .....	24
Spraying Pure Solvents.....	24
Spraying Preparation .....	24
Matrix and Sample Preparation.....	25
AFM Sample Preparation .....	25
Results and Discussion .....	25
Electric Field Measurements using Pure Solvents .....	25
Sprayed Sample Morphology.....	32
Conclusions .....	43
References .....	44
Chapter 4.    Development and Characterization of a Controlled Electrospray Deposition	
Sample Preparation Method .....	47
Introduction .....	47
Experimental .....	52
Sample Preparation for the Angiotensin I/PEG 3400 and CHCA Systems .....	52
Electrospray Deposition Conditions.....	52
Results and Discussion .....	53
Optimization of Spraying Conditions .....	53
Characterization of the Controlled Electro spraying Technique.....	58
Matrix Identity and Concentration Effects on Controlled ESD .....	63
Conclusions .....	85
References .....	87
Chapter 5.    Exploring the Effects of Laser Wavelength on Matrix and Analyte Signal in MALDI-TOFMS.....	89
Motivation .....	89
Introduction .....	91
Desorption .....	91
Ionization .....	93
Chapter Organization.....	96
Experimental .....	96
Matrix Studies .....	96
Solution-Phase UV-Visible Spectroscopy .....	98

Solid-State UV-Visible Spectroscopy .....	98
Matrix-to-Analyte Plots.....	98
QCM Experiments .....	99
Results and Discussion .....	99
Matrix Absorption Spectra.....	99
QCM Desorption Studies.....	104
Matrix-to-Analyte (M/A) Plots for Angiotensin I in CHCA.....	109
Effect of Wavelength on Cationization .....	111
Matrix Background Spectra .....	116
Conclusions .....	120
References .....	120
Chapter 6. Investigation into the Effect of Solvent Composition on MALDI Signal.....	124
Introduction .....	124
Experimental .....	128
Solubility Measurements .....	129
Results and Discussion .....	129
Conclusions .....	137
References .....	138
Chapter 7. Future Work.....	140
Chapter 3.....	140
Chapter 4.....	142
Chapter 5.....	147
Chapter 6.....	148
References .....	152
Appendix A. List of Abbreviations .....	154
Appendix B. Solution and Solid State UV Spectra of Common Matrix Compounds .....	156
VITA.....	162

## List of Tables

Table 2.1: A List of the MALDI matrix materials used in this thesis. The common names or abbreviations for each matrix are provided along with the purity. ....	15
Table 3.1: Factors effecting the sample morphology of electrosprayed MALDI samples. This list has been collected from various articles <sup>23, 27, 30, 32, 33</sup> . ....	34
Table 4.1: List of commercial electrical tapes used to test in the controlled electrospray deposition apparatus and their stated properties.....	49
Table 4.2: Analysis of 4 independent sprays of Angiotensin I and PEG 3400. Each spray is an average of 5 mass spectra of 500 accumulations.....	58
Table 5.1: Experimentally determined slopes for the calibration curves of porcine Insulin using MALDI with incidence wavelengths of 337nm and 355nm. Table reproduced from Zhang and Kinsel <sup>4</sup> .....	91
Table 5.2: Table of relevant MALDI laser parameters reproduced from Dreisewerd <sup>7</sup> .....	92
Table 5.3: List of common MALDI matrix compounds analyzed by solution phase UV-Vis spectroscopy. The absorbance at 266, 337, and 355nm are reported. The absorption coefficients for both 337 and 355nm have been calculated and their ratios compared. It is important to note that these measurements were made in MeOH and their absorbance are likely influenced by the dissolution solvent. ....	100
Table 5.4: List of common MALDI matrix compounds measured by diffuse reflectance UV-Vis spectroscopy at 266, 337, and 355nm. The relative absorbance values are presented as well as the ratio of the absorbance values for each compound at 337 and 355nm. ....	101
Table 5.5: A Comparison between the solution phase and solid state UV-Vis absorbance at 337 and 355nm for common UV-MALDI matrix compounds. The data herein is a summary of Tables 5.4 and 5.5. ....	104
Table 5.6: A list of the critical values calculated for the determination of the mass desorbed as a function of wavelength for CHCA. ....	108
Table 5.7: Table showing the ratios of various CHCA background matrix ion peaks compared between 337nm and 355nm wavelength incident light.....	117
Table 5.8: Table showing the ratios of various SA background matrix ion peaks compared between 337nm and 355nm wavelength incident light.....	119
Table 6.1: Solubility values for 2,5-DHB in MeOH, MeCN, Chloroform and mixtures. Values for the % saturation at the relevant spraying concentrations are given in the last column. The * denotes the azeotrope if it exists for the solvent mixtures. This data was produced by Francisco Guevara.....	130



## List of Figures

Figure 2.1: Diagram of the Reflex III light box as fitted with both a 337nm Nitrogen laser and a 355nm Nd:YAG laser. ....	8
Figure 2.2: Diagram of the Reflex III light box as fitted with both a 337nm Nitrogen laser and a 355nm Nd:YAG laser illustrating the location of alternate paths for both lasers. ....	9
Figure 2.3: Diagram of the home-built ESD apparatus used in this thesis. The diagram includes a current transducer and oscilloscope. ....	13
Figure 2.4: Diagram of the home-built ESD apparatus used in this thesis. The diagram includes a Teflon crystal holder attached to the RQCM. ....	14
Figure 3.1: Images of sprayed material resulting from the three major electro spraying modes. Pulsing jet mode (a), multi-jet mode (b), and cone jet mode (c). ....	19
Figure 3.2: Picture of a spray in the cone jet mode. Cones that visually looked like this were considered to be "good" cones for spraying. ....	20
Figure 3.3: Examples of the current measurements reproduced from Jurashek et al <sup>22</sup> for pulsing jet mode (a) and the cone jet mode (b). ....	21
Figure 3.4: Example measurement made while spraying pure methanol a flow rate of 2.0 $\mu\text{L}/\text{min}$ from a height of 20 mm with an applied voltage of 5.4 kV, demonstrating the cone-jet mode of spraying. ....	22
Figure 3.5: Illustration of cone shape for stable con-jet mode electro sprays reprinted from Cloupeau et al <sup>23</sup> ....	22
Figure 3.6: High speed camera image of the formation of initial droplets at the tip of a Taylor cone in the cone jet spraying mode. Reproduced from Nemes <sup>28</sup> . ....	24
Figure 3.7: Graph showing the effect of spraying distance on the electric field required to maintain a spray in cone-jet mode. Data was collected by spraying pure MeOH at three differing flow rates. ....	27
Figure 3.8: Graph showing the change in the electric field as the spraying distance is adjusted for pure solvent MeOH or 10% mixture of water or isopropyl alcohol (IPA) in MeOH. All data were collected by spraying at a constant flow rate of 5.0 $\mu\text{L}/\text{min}$ . ....	27
Figure 3.9: A graph of the current measured at the grounded electrode of the spraying apparatus as a function of the square root of the flow rate flow rate ( $\mu\text{L}/\text{min}$ ) for solutions of pure solvents and solutions of MeOH containing the MALDI matrix CHCA at 0.1 and 0.01M concentrations. A stable spray for the solutions containing 0.1M CHCA in MeOH was unable to be reached, consequently the data point is not captured in the plot. ....	29

Figure 3.10: Graph showing the interactions of electric field (blue diamonds) and sprayed diameter (red squares) as the spraying height is adjusted. Sprays were made using a 0.01M solution of CHCA in MeOH with a flow rate of 2.5 $\mu\text{L}/\text{min}$ .....	31
Figure 3.11: Graph showing the effect of the square root of the flow rate on the observed sprayed diameter. The data are presented at three spraying flow rates 2.5, 5.0, and 10.0 $\mu\text{L}/\text{min}$ and three spraying heights 20, 25, and 30mm. The spraying solution was 0.01M CHCA in MeOH. ....	35
Figure 3.12: AFM images of 0.02M 2,5-DHB in methanol sprayed from 20mm at flow rates of a) 2.0 $\mu\text{L}/\text{min}$ and b) 5.0 $\mu\text{L}/\text{min}$ . ....	38
Figure 3.13: AFM images of 0.02M CHCA in Methanol using a flow rate of 2.0 $\mu\text{L}/\text{min}$ and sprayed from a) 20 mm and b) 30mm.....	38
Figure 3.14: Graph showing the height distribution of particles deposited from electro spraying samples of 0.02M DHB in MeOH from 20mm and 30mm.....	40
Figure 3.15: Atomic Force Microscopy (AFM) images of electro sprayed samples. The samples of 0.02M 2,5-DHB dissolved in a) MeOH, b) MeCN, c) MeOH:CHCl <sub>3</sub> (1:1), and d) MeOH:MeCN (1:1) were sprayed at a flow rate of 2.0 $\mu\text{L}/\text{min}$ from a distance of 20mm.....	41
Figure 3.16: AFM images of a 0.02M DHB sprayed from a MeOH:Chloroform solution. Images a-f were taken at different locations on the spot. Image a) represents the center of the spot and the images progress outward to f, which is the outer most edge of the spot.....	43
Figure 4.1: Images of two individual controlled ESD experiments using CHCA as a matrix showing a) a probe that was not sufficiently insulated with a single layer of electrical tape and b) a probe with multiple layers of tape with sufficient insulation to direct the sprayed material onto the exposed metal surface and not the taped area.....	50
Figure 4.2: Plot of average peak area of Angiotensin I as a function of repeat spraying. Angiotensin I in 0.02M CHCA at M/A of $\sim 1300:1$ was sprayed for 1 minute intervals. The data points represent the average of 5 independent 500 shot accumulations for each time point. The sample needle was not reloaded between sprays for this study. ....	54
Figure 4.3: Plot of average peak area of Angiotensin I as a function of repeat spraying. Angiotensin I in 0.02M CHCA at M/A of $\sim 1300:1$ was sprayed for 2 minute intervals. The data points represent the average of 5 independent 500 shot accumulations for each time point. The sample needle was not reloaded between sprays for this study. ....	55
Figure 4.4: Plot of average peak area of Angiotensin I as a function of repeat spraying. Angiotensin I in 0.02M CHCA at M/A of $\sim 1300:1$ was sprayed for 4 minute intervals. The data points represent the average of 5 independent 500 shot accumulations for each time point. The sample needle was not reloaded between sprays for this study. ....	56
Figure 4.5: AFM image of a solution of 0.02M CHCA in MeOH sprayed from a height of 20mm and 2.0 $\mu\text{L}/\text{min}$ for 2 minutes using the controlled electro spray deposition technique. ....	59

Figure 4.6: SEM images of controlled and uncontrolled electrospray deposition of 0.02M CHCA in MeOH sprayed from a height of 20mm at 2.0uL/min for 2 minutes. a) Controlled ESD at 5k magnification, b) Controlled ESD at 15K magnification, c) Uncontrolled ESD at 5k magnification, d) Uncontrolled ESD at 15k magnification. The inset micrographs in a) and c) are to demonstrate the gross differences in the size and shape of the resulting sprayed material using each ESD method..... 60

Figure 4.7: Laser confocal micrographs of a controlled electrosprayed sample contained to an area of 1.5mm x 3mm. The Solution sprayed was 0.02M CHCA in MeOH at a flow rate of 2.0uL/min for 2.0 minutes from a height of 20mm. The sample also contained Angiotensin I in a M/A ratio of ~1300:1. The blue arrows in the long axis profile image show surface defects that are from laser sampling of the spot in a MALDI-TOF instrument..... 62

Figure 4.8: Laser confocal micrographs analyzing the edge of a controlled spot sample. The images show a steep rise of the sample edge to a height of ~3um from the metal surface over a distance of ~20um. .... 63

Figure 4.9: SEM images of 0.02M sprays of 2,5-DHB and CHCA in MeOH. Samples were sprayed from a height of 20mm and a flow rate of 2.0uL/min. a) 2,5-DHB sprayed for 30 seconds, b) 2,5-DHB sprayed for 2.0 minutes, c) CHCA sprayed for 30 seconds, d) CHCA sprayed for 2.0 minutes. Images are magnified 30k X..... 65

Figure 4.10: SEM images of CHCA sprayed for 30 seconds at a height of 20mm with a concentration in MeOH of a) 0.01M (5% saturation), b) 0.02M (10% saturation), c) 0.05M (25% saturation) and d) 0.1M (50% saturation). Images are magnified 30K X..... 66

Figure 4.11: SEM images of 0.02M CHCA sprayed at a flow rate of 2.0uL/min for 30 seconds from heights of a) 15mm, b) 20mm, c) 25mm and d) 35mm. Images are magnified 30k X. .... 70

Figure 4.12: Illustration of the modes of particle formation of drying droplets. Reproduced from Leong<sup>9</sup>. .... 72

Figure 4.13: SEM images of 0.02M CHCA sprayed at a flow rate of 2.0uL/min for 30 seconds and a height of 35mm. a) center of sprayed area at 30k X magnification, b) edge of sprayed area at 30k X magnification, c) center of sprayed area at 15k X magnification, d) edge of sprayed area at 15k X magnification..... 74

Figure 4.14: Graph of average peak area as a function of spray height for samples analyzed over two days. Each data point was sprayed from a solution of 0.02M CHCA at 2.0uL/min for 2 minutes. The blue diamonds are samples run on the first day. Pink squares were analyzed on a different day and include two repeated heights at 30 and 40mm. Each data point is the average of three independent sprays from each height. .... 75

Figure 4.15: Total summed areas of the Angiotensin I molecular ion for sprays made from 0.02M CHCA and Angiotensin I (M/A ~1300:1) at 2.0uL/min for 2 minutes from varying spraying heights..... 76

Figure 4.16: Average summed areas of the first 500 laser shots of sprayed solutions of 0.02M CHCA and Angiotensin I (M/A ~1300:1) sprayed at 2.0uL/min for 2 minutes from varying heights. ....	77
Figure 4.17: Averaged peak areas per shot for the first 100 shots of solutions of 0.02M CHCA and Angiotensin I (M/A ~1300:1) sprayed at 2.0uL/min for 2 minutes from varying spray heights. The fitted lines were generated by excel as the best fit linear regression for the data points. The equations are presented here for comparisons only, and are not meant to be a quantitative model for desorption or ionization. Note that this graph is an expansion of the graph presented in Figure 16. ....	78
Figure 4.18: Average summed peak areas for Angiotensin I molecular ion as a function of number of laser shots in a fixed location on the sample. The samples were sprayed from a solution of 0.02M CHCA and Angiotensin I (M/A ~1300:1) at 2.0uL/min at a height of 20mm. ....	80
Figure 4.19: Graph of the average peak area for Angiotensin I molecular ion as a function of the number of shots for the first 100 shots on a clean sample. The samples sprayed were 0.02M CHCA and Angiotensin I (M/A ~1300:1) sprayed at 2.0uL/min from a height of 20mm. ....	81
Figure 4.20: Average peak areas for Angiotensin I molecular ion as a function of spraying time. Samples were prepared on two days from separate solutions of 0.02M CHCA and Angiotensin I (M/A ~1300:1) at a flow rate of 2.0uL/min and a height of 20mm. The data points represent the averages of three independently prepared samples for each spraying height. ....	84
Figure 5.1: A sketch of the proposed processes occurring in the lucky survivor ionization theory adapted from Knochenmuss' 2006 review article <sup>15</sup> . ....	94
Figure 5.2: An illustration of the pooling mechanism for MALDI ionization. This figure is reproduced from Knochenmuss <sup>15</sup> . ....	95
Figure 5.3: Solid state diffuse reflectance and solution phase UV-Vis spectra of four MALDI matrix compounds, a) CHCA, b) 2,5-DHB, and c) SA. The spectra were plotted without normalization; no quantitative data can be discerned from the solid state spectra. ....	103
Figure 5.4: Optical micorgprah of the laser spot profile for the 337nm nitrogen laser and the 355nm Nd:YAG laser. The YAG laser produced a spot that was ~6% larger than that of the nitrogen laser spot. ....	106
Figure 5.5: QCM data for the change in mass per unit area vs time when irradiated with 337nm laser light. The slope of the fitted line was used for the calculation of material removed per laser shot. ....	107
Figure 5.6: QCM data for the change in mass per unit area vs time when irradiated with 355nm laser light. The slope of the fitted line was used for the calculation of material removed per laser shot. ....	107
Figure 5.7: Matrix to analyte plots of Angiotensin I and CHCA analyzed at 337nm and 355nm wavelengths for desorption. Each data point is an average of the protonated molecular ion of	

Angiotensin I for 5 individual accumulations of 50 laser shots randomly acquired over the sprayed sample area.....	110
Figure 5.8: Plot of the relative sodium cationized analytes signal as a function of matrix to analyte ratio at two commonly used MALDI wavelengths, 337 and 355nm. The sodium ratios are calculated against the total analyte signal for angiotensin I. ....	113
Figure 5.9: MALDI mass spectra of Angiotensin I using CHCA as a matrix collected on a Bruker Reflex III instrument using two different wavelengths. The M/A ratio for both samples is ~1300:1. The samples were prepared using the controlled ESD technique.....	115
Figure 5.10: Positive polarity mass spectra of CHCA at both 337 and 355nm wavelengths. The table below the spectra illustrate the relative peak area differences for the same matrix compound that the two wavelengths.....	117
Figure 5.11: Positive polarity mass spectra of CHCA at both 337 and 355nm wavelengths. The table below the spectra illustrate the relative peak area differences for the same matrix compound that the two wavelengths.....	119
Figure 6.1: Stern-Volmer plots of arginine with NaCl, NaBr, and NaI from 1-25mM concentrations. Error bars are calculated for the 95% confidence intervals. Reproduced from Holcomb <sup>2</sup> .....	125
Figure 6.2: The fluorescence emission spectra of 2,5-DHB when excited at 337nm. 6ppm solutions of 2,5-DHB were made in pure MeOH, MeCN and Chloroform. The intensity of the emission at 445nm is given in the tabular inset. These spectra were collected as part of the undergraduate research of Francisco Guevara. ....	128
Figure 6.3: Plot of the average peak area for Angiotensin I molecular ion as measured by MALDI using a controlled ESD sample preparation technique. Solutions of 2,5-DHB and Angiotensin I were prepared in four different solvent compositions for spraying denoted in the legend.....	131
Figure 6.4: Plot of the average peak area of Angiotensin I molecular ion from MALDI samples prepared from different solvent conditions. The samples were prepared by controlled ESD....	134
Figure 6.5: Stern-Volmer plot of Angiotensin I peak area as a function of volume percent MeCN in the sample preparation. ....	135
Figure 7.1: Picture of the novel MALDI target plate set inside of a Bruker MTP TLC Adapter that had been modified to accommodate the target. The arrow indicates the location of a controlled ESD sample preparation. ....	144
Figure 7.2: MALDI TOFMS spectrum of Ang I using CHCA as a matrix from the surface of the novel PCB MALDI sample target. The inset is an expansion of the $[M + H]^+$ Ang I peak demonstrating the mass resolution.....	145
Figure 7.3: MALDI TOFMS spectra (a) of a clean metal pad where sample had not been sprayed; and (b) a metal pad directly adjacent to a metal pad that had been sprayed onto using a solution of Ang I and CHCA in MeOH.....	145

Figure 7.4: MALDI-TOFMS spectrum taken from the insulating material on the PCB sample target. The peak observed in this spectrum is a system peak of the instrument. ....	146
Figure 7.5: A plot of the mass collected on the QCM crystal as a function of time. Note that the slope of the line for this plot will have units of $\mu\text{g}/\text{cm}^2$ .....	151
Figure B.1: Solution and Solid State UV-Vis spectra of the matrix compound ANP .....	156
Figure B.2: Solution and Solid State UV-Vis spectra of the matrix compound ATT .....	157
Figure B.3: Solution and Solid State UV-Vis spectra of the matrix compound 1,5-diaminonaphthalene.....	157
Figure B.4: Solution and Solid State UV-Vis spectra of the matrix compound dithranol .....	158
Figure B.5: Solution and Solid State UV-Vis spectra of the matrix compound FA .....	158
Figure B.6: Solution and Solid State UV-Vis spectra of the matrix compound HABA.....	159
Figure B.7: Solution and Solid State UV-Vis spectra of the matrix compound IAA.....	159
Figure B.8: Solution and Solid State UV-Vis spectra of the matrix compound 4-NA .....	160
Figure B.9: Solution and Solid State UV-Vis spectra of the matrix compound THAP .....	160
Figure B.10: Solution and Solid State UV-Vis spectra of the matrix compound vanillic acid .....	161

## Abstract

Exploration of the Effects of Electrospray Deposition Spraying Parameters and Incidence Laser Wavelength on Matrix Assisted Laser Desorption Ionization Time-of-Flight Mass Spectrometry

Jonathan R. Haulenbeek

Kevin G. Owens, Ph.D.

This thesis investigates the use of electrospray deposition (ESD) as a sample preparation technique for matrix assisted laser desorption ionization time-of-flight mass spectrometry (MALDI-TOFMS) and laser wavelength effects on the MALDI-TOFMS signal. A brief description of critical ESD parameters is provided and studies aimed at understanding the parameters that define the spraying diameter are presented. The experimental data suggest that the solvent and solute identity, solute concentration, spraying flow rate and spraying distance all affect the final sprayed sample diameter and the morphology of the amorphous particles deposited on the sample surface. The invention of a controlled ESD technique is described and both the gross sample morphology and sprayed particle morphology are discussed. Key spraying parameters of the controlled ESD technique are investigated using a combination of scanning electron microscopy, laser confocal microscopy and MALDI-TOFMS. Samples sprayed for longer time periods and sprayed from a larger spraying distance yielded MALDI samples with increased analyte sensitivity.

A MALDI-TOFMS instrument equipped with two lasers operating at 355 and 337nm was used to investigate analyte response at the two wavelengths. Solid state and solution phase UV-visible absorption spectroscopy and a quartz-crystal micro-balance were also used to investigate the differences in absorption and desorption of MALDI matrix compounds at both wavelengths. Common MALDI matrix compounds were shown to have similar absorbance at both wavelengths in the solid state, however, the mass of desorbed material per laser shot was

shown to be greater when using a 355nm laser. The absolute analyte signal at the optimal matrix-to-analyte molar ratio is greater when using an incidence wavelength of 355nm.

The effect of dissolution solvent on MALDI signal was investigated using the ESD technique. The addition of acetonitrile into solutions of methanol was shown to decrease the observed analyte signal. A mixture of chloroform and methanol produced analyte signals greater than those generated by a solution of methanol alone. The data suggest that acetonitrile quenches the MALDI signal when using ESD as a sample preparation technique. The addition of chloroform as a co-solvent may affect the particle morphology of the sprayed samples leading to the increased analyte signal.





## Chapter 1. Introduction and Overview

### MALDI-TOFMS

Matrix assisted laser desorption ionization (MALDI) was first presented in the late 1980's as a soft ionization technique for the analysis of intact large molecular species<sup>1, 2</sup>. The technique uses laser energy to desorb the analyte, which is first embedded in a light absorbing matrix, from a solid sample surface. The result of this process is generally the production of intact molecular ions of the analyte. Since MALDI tends to generate intact singly protonated analyte ions, it is typically coupled with a time-of-flight (TOF) mass analyzer. TOF analyzers are theoretically not mass-to-charge ( $m/z$ ) limited and pair well with the pulsed lasers used to interrogate MALDI samples. Since its discovery, MALDI has been used to analyze various chemical species, including proteins and peptides<sup>3-5</sup>, polymers<sup>6, 7</sup>, inorganic complexes<sup>8</sup>, and intact bacteria<sup>9</sup>.

The MALDI process can be broken into four main steps: sample preparation, desorption, ionization and mass analysis<sup>10</sup>. The first step is the only process that is not carried out in the instrument. Sample preparation is of critical importance to the success of the MALDI experiment. Among the parameters that must be considered are the identity of the matrix and dissolution solvent. The analyte of interest must be miscible in the dissolution solvent as well as the matrix. For the experiment to be successful the matrix and analyte must be closely associated in the dried sample mixture.<sup>11</sup> The molar ratio of the matrix and analyte have also been shown to be important, as too much or too little matrix will result in the suppression of analyte ions<sup>11, 12</sup>. There are many examples where solvent free sample preparations<sup>13</sup> have been used, but generally the analyte and matrix are mixed in a solvent and then deposited as a liquid

on the MALDI sampling plate. The solution is then dried in some manner in order to remove the solvent, leaving behind a solid mixture of the matrix and analyte. The removal of solvent is a critical step as it will affect the morphology of the solid sample left behind. The main goal of sample preparation is to produce a thin layer of a homogeneous mixture of matrix and analyte on the surface of the MALDI probe<sup>11</sup>. Preparation techniques for accomplishing this task will be further discussed in later chapters of this thesis.

After the samples have been prepared and dried to a solid they are placed into the ion source of the mass spectrometer. A focused laser beam is directed at the sample where it induces desorption of the solid, the second step in the MALDI process. The matrix molecules absorb the laser light which promotes the breaking of intermolecular bonds and disintegration of the matrix molecules. At the site of the laser pulse, matrix and the analyte molecules closely associated with the matrix are accelerated away from the surface in the form of a supersonic jet<sup>14</sup>. The material being accelerated from the surface forms an initially dense plume of molecules that interact chemically to form ionized analytes<sup>15</sup>. These ionization processes are the third step in the MALDI experiment and the result of these chemical reactions are then mass analyzed by the TOF mass spectrometer (MS).

In a TOF analyzer the mass-to-charge ( $m/z$ ) ratio of an ion is related to the time it takes to travel a fixed distance. The drift region is a field free evacuated drift tube and the velocity of the ion is related to the kinetic energy of the ion upon introduction into the tube. A comprehensive review of TOF has been written by Cotter<sup>16</sup>. Due to the fact that the  $m/z$  of an ion is being indirectly measured calibration of the TOF analyzer is critical to obtaining accurate mass information.<sup>17</sup> Understanding each of the four steps in the MADLI process is important for a successful experiment.

## Organization of the Thesis

The main goal of this thesis is to explore the critical parameters in the electrospray deposition (ESD) sample preparation process as used for creating homogeneous samples for MALDI sample analysis. Using the knowledge gained from these investigations, the effects of using 337 versus 355nm wavelength lasers for sample desorption will also be investigated. A brief discussion on the impact of sample dissolution solvent when using ESD will also be presented.

Chapter 2 describes the analytical instrumentation, materials, and sample preparation methodologies used in the four main projects presented. Additional experimental details are given in each of chapters 3 through 6 where applicable to better explain the theory and goals of the specific experiments described there.

Chapter 3 focuses on exploring the critical measurable variables in the ESD process. The effects of flow rate, matrix concentration and spraying distance on the sprayed diameter of the spot are discussed. A current transducer is incorporated into the ESD apparatus to control the spraying mode. Current measurements made using the transducer also aid in the interpretation of the experimental results. Finally, preliminary investigations into the microscopic morphology of the sprayed particles are performed.

Chapter 4 details the development of a new controlled ESD technique. The new technique reduces the sprayed area of the sample by ~95% as compared to the uncontrolled ESD method. The effect of matrix concentration and solubility on the deposited particle morphology is also investigated. The spraying parameters explored in Chapter 3 are revisited to determine their effects on the solid droplet morphology as well as the MALDI performance of the samples. These studies demonstrate that using the controlled ESD technique analyte ion signal could be increased by optimizing the spray flow rate, spraying distance and spraying time.

Chapter 5 details experiments performed to elucidate differences between the use of 337nm and 355nm laser light for sample desorption. Solution phase UV-visible absorption and solid state diffuse reflectance spectra are collected for numerous common MALDI matrix compounds. The absorption of the two wavelengths in the solid state deviated significantly from that in the solution phase for many of the matrix compounds analyzed. Further studies are then conducted to determine the amount of material desorbed from the surface per laser shot at 337nm and 355nm. M/A plots of CHCA and Angiotensin I are prepared using the controlled ESD technique and analyzed at the two wavelengths. The plots show a dependence on the wavelength for analyte signal saturation. An increase in cationization of the analyte is also observed when 355nm light is used for desorption. Background matrix MALDI spectra are also discussed in the chapter as a function of incidence wavelength.

Chapter 6 investigates the effect of solvent identity on the MALDI analyte signal when ESD is used as the sample preparation technique. Signal suppression is observed when acetonitrile is used in the dissolution solvent. The possible mechanisms for analyte suppression are discussed. The possible effects of matrix concentration and saturation limit in the spraying process are also touched on in the context of sample droplet morphology.

Finally, chapter 7 describes future work that should be performed to further investigate the findings detailed in the earlier chapters.

## References

1. Tanaka, K.; Waki, H.; Ido, Y.; Akita, S.; Yoshida, Y.; Yoshida, T.; Matsuo, T., Protein and polymer analyses up to  $m/z$  100 000 by laser ionization time-of-flight mass spectrometry. *Rapid Communications in Mass Spectrometry* 1988, 2 (8), 151-153.
2. Karas, M.; Hillenkamp, F., Laser desorption ionization of proteins with molecular masses exceeding 10,000 daltons. In *Analytical Chemistry*, 1988; Vol. 60, pp 2299-2301.
3. Bansal, S. S.; Halket, J. M.; Fusova, J.; Bomford, A.; Simpson, R. J.; Vasavda, N.; Thein, S. L.; Hider, R. C., Quantification of hepcidin using matrix-assisted laser desorption/ionization time-

- of-flight mass spectrometry. *Rapid Communications in Mass Spectrometry* 2009, 23 (11), 1531-1542.
4. Bizzarri, M.; Cavaliere, C.; Foglia, P.; Guarino, C.; Samperi, R.; Lagana, A., A label-free method based on MALDI-TOF mass spectrometry for the absolute quantitation of troponin T in mouse cardiac tissue. *Analytical and Bioanalytical Chemistry* 2008, 391 (5), 1969-1976.
  5. Zhang, N.; Doucette, A.; Li, L., Two-layer sample preparation method for MALDI mass spectrometric analysis of protein and peptide samples containing sodium dodecyl sulfate. *Analytical Chemistry* 2001, 73 (13), 2968-2975.
  6. Szyszka, R.; Hanton, S. D.; Henning, D.; Owens, K. G., Development of a Combined Standard Additions/Internal Standards Method to Quantify Residual PEG in Ethoxylated Surfactants by MALDI TOFMS. *Journal of the American Society for Mass Spectrometry* 2011, 22 (4), 633-640.
  7. Hanton, S. D.; Hyder, I. Z.; Stets, J. R.; Owens, K. G.; Blair, W. R.; Guttman, C. M.; Giuseppetti, A. A., Investigations of electrospray sample deposition for polymer MALDI mass spectrometry. *Journal of the American Society for Mass Spectrometry* 2004, 15, 168-179.
  8. Hunsucker, S. W.; Watson, R. C.; Tissue, B. M., Characterization of inorganic coordination complexes by matrix-assisted laser desorption/ionization mass spectrometry. *Rapid Communications in Mass Spectrometry* 2001, 15 (15), 1334-1340.
  9. Smole, S. C.; King, L. A.; Leopold, P. E.; Arbeit, R. D., Sample preparation of Gram-positive bacteria for identification by matrix assisted laser desorption/ionization time-of-flight. *Journal of Microbiology Methods* 2002, 48 (2-3), 107-115.
  10. Hanton, S. D., Owens, K. G., Conventional MALDI Sample Preparation. In *MALDI Mass Spectrometry for Synthetic Polymer Analysis*, Li, L., Ed. John Wiley & Sons, Inc.: New York, 2010.
  11. Hanton, S. D., Owens, K. G., MALDI MS Applications for Industrial Polymers. In *MALDI Mass Spectrometry for Synthetic Polymer Analysis*, Li, L., Ed. John Wiley & Sons, Inc.: New York, 2010.
  12. Knochenmuss, R.; Karbach, V.; Wiesli, U.; Breuker, K.; Zenobi, R., The matrix suppression effect in matrix-assisted laser desorption/ionization: Application to negative ions and further characteristics. *Rapid Communications in Mass Spectrometry* 1998, 12 (9), 529-534.
  13. Hanton, S. D.; McEvoy, T. M.; Stets, J. R., Imaging the Morphology of Solvent-Free Prepared MALDI Samples. *Journal of the American Society for Mass Spectrometry* 2008, 19, 874-881.
  14. Dreisewerd, K., The desorption process in MALDI. *Chemical Reviews* 2003, 103 (2), 395-425.
  15. Knochenmuss, R.; Zenobi, R., MALDI ionization: The role of in-plume processes. *Chemical reviews* 2003, 103 (2), 441-452.
  16. Cotter, R. J., *Time-of Flight Mass Spectrometry*. American Chemical Society: Washington, DC, 1994.
  17. Erb, W. J. Exploration of the fundamentals of matrix assisted laser desorption/ionization time-of-flight mass spectrometry. PhD thesis, Drexel University, Philadelphia, 2007.

## Chapter 2. Experimental

### Introduction

Information about the instrumentation, materials and sample preparation methods used for the entire thesis are covered in this chapter. Sample preparation details will be described in separate experimental sections in each chapter, as will specific details about specific instrumental operations where applicable.

### Instrumentation

#### ***Bruker AutoFlex III MALDI TOF*** - Chapters 4 and 6

Mass spectra were collected on a Bruker (Bremen, Germany) AutoFlex III MALDI TOFMS running FlexControl version 3.0 (Build 183) flex-series 1.2 SP 1 Patch 3 software. The instrument was operated in the reflectron mode with a 30 nanosecond pulsed ion extraction (PIE) delay. The instrument is equipped with a pulsed (200Hz maximum repetition rate) frequency tripled neodymium-doped yttrium aluminum garnet (Nd:YAG) laser operating at 355nm. The laser energy was adjusted to just above the threshold for ion production for the first sample analyzed in each experiment. The energy was then held constant for all other samples for that experiment. The repetition rate of the laser was 100Hz for all samples. Typical voltage values used for the TOFMS were 19.0kV on IS1, 16.8kV on IS2 and 21.0kV on the reflector. The voltage applied to the microchannel plate detector was 1.65kV. The voltage on the lens was set to 7.9kV. The voltages for IS2 and the lens were adjusted to obtain the highest resolution of the collected mass spectra. Internal mass calibration was performed using FlexAnalysis v3.0.92.0 for flex-series 1.2 ServicePack 1. Data processing and peak area calculations were also performed in the FlexAnalysis software.

***Bruker Reflex III MALDI TOF*** - Chapter 5

Mass spectra were acquired on a Bruker (Bremen, Germany) Reflex III MALDI TOFMS instrument running Bruker XACQ version 4.0 software running on a Sun (Sunnyvale, CA) Sparcstation 5 workstation. Internal mass calibration was performed using FlexAnalysis v3.0.92.0 for flex-series 1.2 ServicePack 1. Data processing and peak area calculations were also performed in the FlexAnalysis software.

The analyses were performed in positive ion reflectron mode using a medium PIE delay. The instrument was equipped with a Laser Science Inc. (Franklin, MA), Model VSL-337ND nitrogen laser at 337nm and a Continuum, Inc. (Santa Clara, CA), Minilite I Nd-YAG (frequency tripled) laser at 355nm. A diagram of the modified light box on the Reflex instrument used for the two wavelength studies described in Chapter 5 is found in Figure 2.1. The standard nitrogen laser was aligned into the instrument prior to the alignment of the Nd:YAG laser. The beam shape on the probe surface and the ion signal were optimized for the nitrogen laser. The YAG laser beam was passed through a 2X Galilean telescope beam expander consisting of a 1" diameter fused silica plano-concave lens with a 25mm focal length (fl) followed by a 1" diameter fused silica plano-convex lens with a 75mm fl connected with 1" beam tubes all from ThorLabs, Inc. (Newton, NJ) to equalize the beam diameters. A set of 1" diameter UV enhanced aluminum mirrors (ThorLabs), including a model M355-FR45-ID-MB 1" dichroic mirror from Princeton Instruments (Trenton, NJ, used to filter out residual 1<sup>st</sup> and 2<sup>nd</sup> harmonic light) were used to align the beam co-linearly with the nitrogen laser beam. The spot size of the YAG laser was adjusted to be within ~10% of the area of the nitrogen beam using an iris. The intensity of each beam was measured prior to entering the instrument by reflecting the beam into a model RJ-7610 Energy Radiometer, equipped with a model RJP-735 pyroelectric energy probe from Laser



Precision Corp. (Glennedale, CA). The mass spectrometer instrument parameters were optimized for the best mass resolution at 1297 Da for the M/A experiments and at 1000 Da for the matrix background spectra by adjustment of the IS2 and lens voltages. All mass spectra were recorded at the maximum 1Gs/s data sampling rate of the installed digitizer. For studies of the matrix background ions, the laser fluence of the nitrogen laser at 337nm and YAG laser at 355nm were selected to be just above threshold for the observation of MALDI ions. For the M/A experiments the laser fluence was set to just above threshold for the sample containing the highest M/A ratio and then held constant for the remaining M/A samples. Each individual mass spectrum was the sum of 50 shots acquired by manually rastering the laser spot across the sample surface. An average of five mass spectra were obtained from every sample.

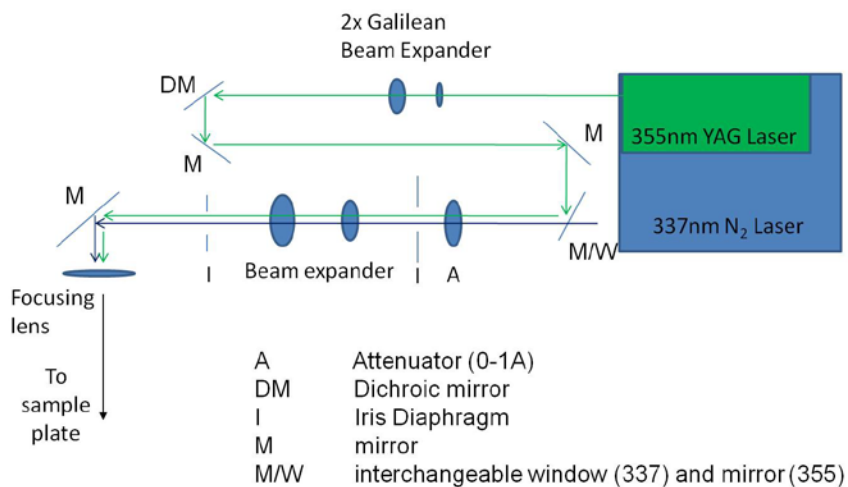


**Figure 2.1: Diagram of the Reflex III light box as fitted with both a 337nm Nitrogen laser and a 355nm Nd:YAG laser.**

Figure 2.2 illustrates the location of the power meter and additional optics that were used to focus the two lasers onto the quartz crystal microbalance (QCM) crystal as described in Chapter 5. Mirrors and lenses matching those found in the Reflex III were used to direct and focus the laser beams onto the QCM crystal. The reflectance/transmission of all mirrors and

lenses used in the instrument were measured using a Perkin-Elmer Lambda-950 UV-visible absorption spectrometer (described below) to ensure no significant differences in the reflection/ transmission properties existed that would lead to energy deposition discrepancies. The Teflon QCM crystal holder was positioned near the focal length of the lasers in the light box and connected to the QCM externally.

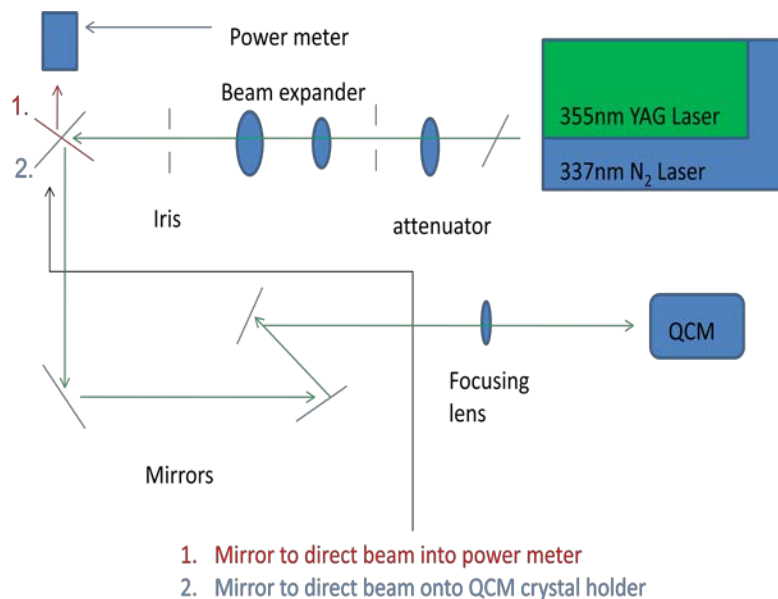


**Figure 2.2:** Diagram of the Reflex III light box as fitted with both a 337nm Nitrogen laser and a 355nm Nd:YAG laser illustrating the location of alternate paths for both lasers.

### ***Atomic Force Microscope (AFM)*** – Chapter 3 and 4

AFM images were obtained on a Veeco Metrology Inc. (Santa Barbara, CA) MultiMode NanoScope IIIa scanning probe microscope SPM. Tapping mode was utilized at 0.5Hz scan rate. Height images were obtained with an oscillating frequency of 336Hz, the integral gain and proportional gain were adjusted for each image to maximize the resolution of the images. Antimony (n) doped Si cantilevers, model TESP of 312- 347kHz frequency from Veeco were utilized for the measurements. Samples were imaged from the surface of 0.5” gold coated

mirrors with a  $\lambda/10$  surface flatness and 6.0 mm thickness (part No. PF05-03-M01) purchased from ThorLabs. AFM images were captured with Nanoscope Control V6.13rR1(R) software. The captured images were then analyzed using Research Nanoscope V7.30 (Build R1Sr3.55790).

### ***3D Laser Scanning Confocal Microscope*** – Chapter 4

Image and height information of Angiotensin I and CHCA samples prepared by controlled electrospray deposition onto a Bruker 10 spot multiprobe plate were acquired on a Keyence, Inc. (Elmwood Park, NJ) VK-X 200 3D laser scanning confocal microscope. The measurements were made using a violet laser diode operating at 408nm. The microscope was equipped with 16-bit photomultiplier detection system.

### ***UV/Visible Absorption Spectrophotometer*** – Chapter 5

All spectrophotometric measurements were performed on Perkin-Elmer, Inc. (Shelton, CT) Lambda-950 UV/visible/NIR absorption spectrometer equipped with a Labsphere, Inc. (North Sutton, NH) 60mm diffuse reflectance sphere controlled by Perkin-Elmer UV WinLab version 5.35 software. Absorption scans were taken over the 200 nm to 850 nm wavelength range at a 1 nm slit width and 480 nm/min scan speed, and saved at a 1 nm data interval.

### ***SpeedVac™ Concentrator*** – Chapter 6

A SpeedVac™ Concentrator (Savant Instruments Inc., Farmingdale, NY) was used to remove solvent from the solute-solvent mixture for the matrix solubility measurements. A Branson 1510 ultrasonic cleaner (Branson Ultrasonic Corporation, Danbury, CT) was used to help dissolve samples.

### ***Quartz Crystal Microbalance*** – Chapter 5

An Inficon, Inc. (East Syracuse, NY) Research Quartz Crystal Microbalance (R-QCM) equipped with a 5MHz AT cut crystal and a model CHT-100 teflon crystal holder was used for the desorption studies. The sensitivity of the instrument is  $0.4\text{ng}/\text{cm}^2$ . Mass changes were monitored using the Maxtek data logging software (version 2.0.3)

### ***Scanning Electron Microscope*** – Chapter 4

Scanning electron micrographs were obtained on a Zeiss Supra VP50 microscope from Carl Zeiss International.

### ***Statistical Analyses*** – Chapters 3, 4, 5, and 6

The error bars in all plots represent 95% confidence intervals.

## **Sample Deposition Methods**

### ***Dry Drop Method***

The dried-drop technique was used to prepare samples for the background matrix spectra described in Chapter 5. The technique was performed by dissolving the matrix in a solvent.  $2.0\ \mu\text{L}$  of the resultant solution mixture were then applied with an Eppendorf pipette onto a Bruker 10 spot multiprobe plate and allowed to dry at room temperature prior to insertion into the mass spectrometer.

### ***Electrospray Deposition Method***

A schematic of the custom-built electrospray deposition (ESD) apparatus used in this work is presented in Figure 2.3. The apparatus consists of a Harvard Apparatus Inc. (Holliston, MA) model 22 infusion pump and a custom-built high voltage power supply (based on a Bertan,

Inc. (Hauppauge, NY) model PMT-75CP-3 0 250  $\mu$ A precision PMT power supply module, output voltage 0–7.5 kV). The electrospray (ES) needle is a 100 mm length of 1.6 mm o.d. x 0.25 mm i.d. stainless steel (SS) HPLC tubing (Alltech, Inc., Deerfield, IL) mounted in a Delrin holder. A 1000  $\mu$ L gas-tight syringe (Hamilton, Inc., Reno, NV) mounted in the infusion pump is connected to the ES needle by a 0.5 m length of 0.125 mm i.d. teflon tubing using a Hamilton three port 90° flow path manual valve (Hamilton Company, Reno, NV). The sample flow rate is set between 2.5 and 10  $\mu$ L/min while a potential in the range of 4.9 to 6.5kV is applied to the needle. The sample target was placed onto a current transducer made of two resistively coupled 1/16" aluminum plates the approximate diameter of the sample target separated by a 0.75" thick Lucite insulator. The current transducer was connected co-axially to a Tektronics Inc. (Beaverton, OR) model TDS 220, 2 channel digital real-time oscilloscope with a 1GS/s sampling rate. The sample target and current transducer are held at ground potential at a specified distance from the needle.

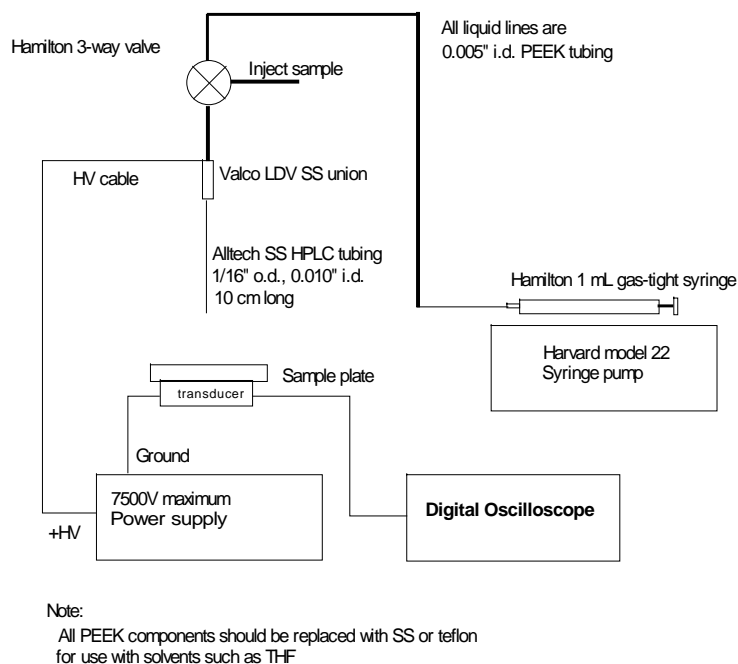


**Figure 2.3: Diagram of the home-built ESD apparatus used in this thesis. The diagram includes a current transducer and oscilloscope.**

A modified version of the ESD apparatus described above is presented in Figure 2.4. The key difference in the configuration shown in Figure 2.4 is that the current transducer and oscilloscope have been replaced with the Teflon crystal holder connected to the RQCM. This apparatus was used for the coating of the QCM crystals for the desorption experiments described in Chapter 5.

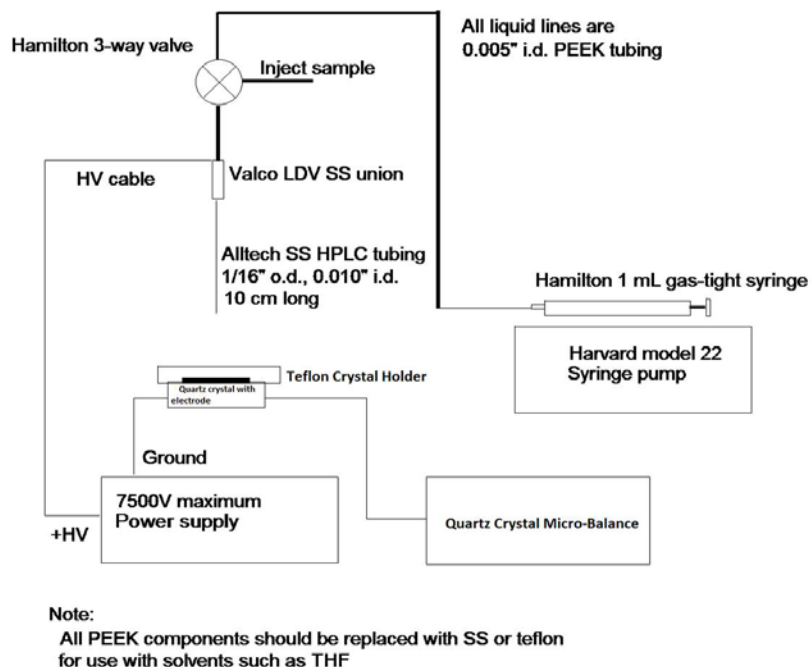


Figure 2.4: Diagram of the home-built ESD apparatus used in this thesis. The diagram includes a Teflon crystal holder attached to the RQCM.

## Materials

### *MALDI Matrix Materials*

All matrix materials used in this thesis are listed in Table and were used as received. The matrix materials were obtained from Aldrich Chemical Company (Milwaukee, WI) with the exception of dithranol, which was obtained from Fluka chemical Company (Milwaukee, WI).

**Table 2.1:** A List of the MALDI matrix materials used in this thesis. The common names or abbreviations for each matrix are provided along with the purity.

Compound Name	Common Name / Abbreviation	Purity
2,5-dihydroxybenzoic acid	2,5-DHB	98%
alpha-cyano-4-hydrocinnamic acid	CHCA	99%
1,8-dihydroxyanthracen-9(10H)-one	Dithranol	≥98.5%
3,5-dimethoxy-4-hydrocinnamic acid	Sinapinic Acid	98%
3-methoxy-4-hydroxycinnamic acid	Ferulic Acid	99%
2,4,6-trihydroxyacetophenone	THAP	98%
2-(4-hydroxyphenylazo)-benzoic acid	HABA	NA
trans-3-indoleacrylic acid	IAA	99%
4-hydroxy-3-methobenzoic acid	Vanillic Acid	NA
6-aza-2-thiothymine	ATT	99%
2-amino-4-methyl-5-nitropyridine	ANP	98%
4-nitroaniline	4-NA	99+%
1,5-diaminonaphthalene	1,5-DAN	97%

### ***Analytes***

Human Angiotensin I (AngI) was purchased from Genway Biotech Inc. (San Diego, CA). The material was diluted to a concentration of 1.0 mg/mL in deionized water. 50 and 100uL aliquots of the 1.0mg/mL solution were placed into 1.5 mL polypropylene microcentrifuge tubes. The tubes were then placed in a SpeedVac<sup>TM</sup> Concentrator to remove the water. The dried peptide was then stored at -20C until use. Commercial poly(ethylene glycol) (PEG 3600) with an average molecular weight of 3600 was purchased from Aldrich Chemical Company.

### ***Solvents***

Deionized water was prepared using a Barnstead E-Pure purification system equipped with a 0.2µm filter. Inhibitor free Tetrahydrofuran (THF) and HPLC grade acetonitrile (MeCN) and methanol (MeOH) were purchased from Aldrich Chemical Company. Trifluoroacetic acid



(TFA) was purchased from EMD Chemicals (Gibbstown, NJ). Chloroform (ethanol stabilized) was purchased from Fisher Scientific (Pittsburgh, PA). Isopropyl alcohol (IPA) was purchased from Spectrum Chemical Mfg. Corp. (Gardena, CA).

## **Chapter 3. Description and Characterization of Electrospray Deposition as used for the Preparation of MALDI-TOFMS Samples**

### **Introduction**

Matrix Assisted Laser Desorption Ionization Time-of-Flight Mass spectrometry (MALDI-TOFMS) is often described as a qualitative technique. There are, however, many examples in the literature detailing quantitative MALDI methods for the analysis of peptides and proteins<sup>1-3</sup>, sugars<sup>4</sup> and synthetic polymers<sup>5</sup>. Upon examination of these methods it becomes clear that the issue of sample preparation is of paramount importance. For quantitation to be possible a uniform layer or layers of well mixed matrix and analyte must be deposited on the MALDI probe<sup>6</sup>. To accomplish this task varying techniques for matrix and analyte deposition have been conceived and tested. Such methods include: fast evaporation<sup>7</sup>, thin layer<sup>8</sup>, two-layer<sup>9,10</sup>, and three-layer techniques<sup>11</sup>, as well as oscillating-capillary nebulization preparation<sup>12</sup>. A modified aerospray device based on a hybrid design of the oscillating-capillary nebulizer and aerospray technique presented by Wilkins<sup>13</sup> has also been used for homogeneous sample preparation<sup>14,15</sup>. All have been shown to be effective to varying degrees. Previous work in our group has focused on the development of electrospray deposition<sup>16-18</sup>.

Electrospray deposition creates a thin layer of amorphous solid particles on the surface of the MALDI probe. The samples are believed to be homogeneous<sup>19</sup> and form layers of nanometer size amorphous solid particles on the surface that leads to an increase in precision in the MALDI experiment<sup>17</sup>. The deposited particles are formed when a solution of pre-mixed matrix and analyte are allowed to flow through a conductive needle, to which a sufficient voltage is applied,

while the MALDI probe or target is held at ground potential. The applied electric field forms a Taylor cone at the end of the needle or metal tubing. The cone is stabilized by the hydrodynamic pressure applied by a pump and backing solvent and the tangential forces of the electric field on the cone<sup>20</sup>. As the electrostatic forces at the tip of the cone become too large, charged droplets of the solution are released and then accelerated toward the grounded plate.

The goal of electrospray deposition is to deposit nearly dry particles onto the sample plate surface. Droplets that are too wet can cause “splashing” on the surface<sup>21</sup>; further, wet droplets allowed to dry on the surface form crystalline structures on the surface of the probe. On-probe crystallization would be similar to the classic “dried drop” sample preparation method, and would not lead to a uniform and homogenous surface to be interrogated in the MALDI experiment. Previous work in our group suggests that the central area of the deposited material produces the most precise MALDI spectra<sup>16</sup>. Most commercial MALDI targets contain machined circles that are 1-3mm in diameter. The area sprayed during ESD sample preparation using our home-built system creates sample diameters in the 10-30mm range. The center of these larger radius samples are not easily directed into the pre-machined sample spots on the targets. This makes finding and then sampling the central area of the ESD spot difficult in commercial MALDI instruments.

Experiments to optimize the precision of the sprayed samples have been performed in our lab. The results of these studies suggested that pumping flow rate and spraying height are key variables<sup>17</sup>. The work described in this chapter will detail further attempts to characterize and define the key parameters affecting the morphology of the deposited particles and their subsequent impact on MALDI sample precision. The first parameters that will be looked at are those that define the size of the sprayed material on the surface.

## Spraying Modes

In order to understand the size of the deposited area it is important to define the spraying regimes in electrospray. The electrospraying phenomenon is known to consist of various regimes of spray modes<sup>22, 23</sup>. Classically these can be broken into three simple categories: pulsing jet mode, cone jet mode and multi-jet mode. There are finer divisions within these broader categories<sup>24</sup>, but for the purposes of these studies one need only distinguish between the three main modes mentioned above. Examples of samples generated from each of these major regimes can be found in Figure 3.1.

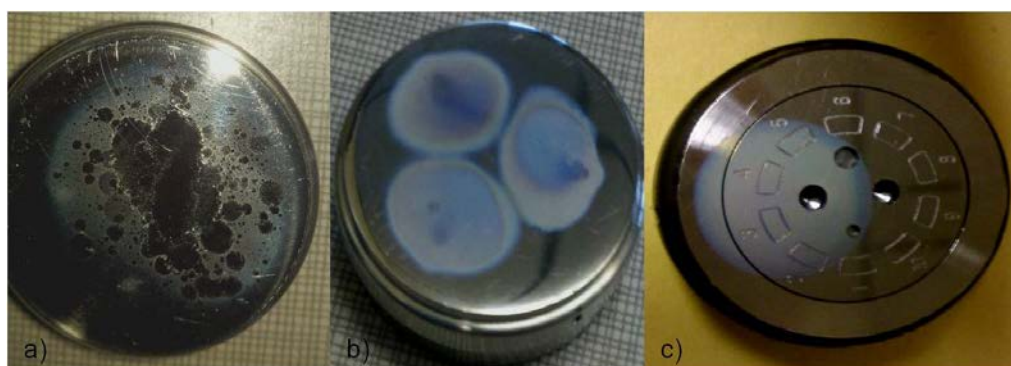


**Figure 3.1:** Images of sprayed material resulting from the three major electrospraying modes. Pulsing jet mode (a), multi-jet mode (b), and cone jet mode (c).

The pulsing mode is not a continuous spraying regime, and as such often creates large droplets that are pulsed from an unstable cone. This regime does not produce quality surfaces of particles for MALDI experiments, as it leads to “spotty” coverage of the sprayed material and sprays of this kind can be rejected by visual inspection (Figure 5a). The multi-jet mode is reached at voltages well above that needed for cone jet spraying and results in two or more Taylor cones being formed at the end of the needle. The electrostatic repulsion of charged droplets of the same polarity produced by the multi-jet mode results in numerous non-overlapping circles on

the target surface; this spraying mode is generally not used for ESD (Figure 5b)<sup>25</sup>. Finally, the cone jet mode is considered to be a stable continuous spraying mode that forms a single cone at the end of the electrospray needle. It is important to note here that cones in this mode can form in differing ways. Elongated cones can be formed if a voltage near onset of the cone jet mode is used; however, these elongated cones eventually become unstable and result in sample spitting. Skewed cones can be formed by crystallization in the tubing or at the ends and edges of the tubing which cause spraying in directions that are not orthogonal to the MALDI target. The cone jet mode produces samples that exhibit highly reproducible MALDI signals (~3-15% CV) in previous work<sup>17</sup>. The spraying mode for a given sample is usually confirmed visually using a video camera fitted with a telescopic lens. Figure 3.2 shows a typical Taylor cone formed under “good” spraying conditions.

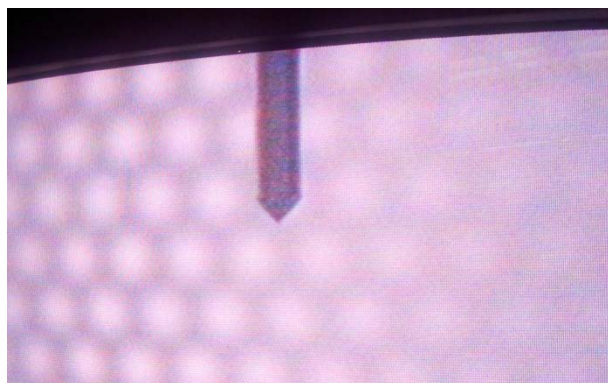


**Figure 3.2: Picture of a spray in the cone jet mode. Cones that visually looked like this were considered to be "good" cones for spraying.**

Changes between the modes can be subtle and for our experiments it was important to ensure that the spraying modes were the same for all samples. Jurashek et al.<sup>22</sup>, measured the differences between spraying modes using an oscilloscope to monitor the current deposited on

the grounded sample plate. Figure 3.3 shows the current measurements made in their study for the pulsing mode (a) and the cone jet mode (b).

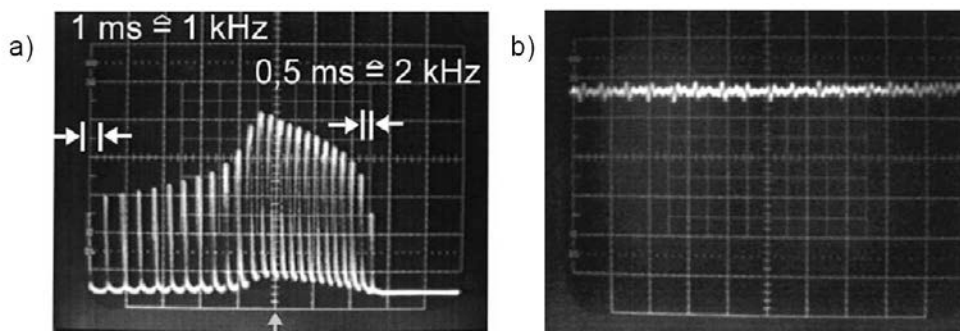


**Figure 3.3:** Examples of the current measurements reproduced from Jurashek et al<sup>22</sup> for pulsing jet mode (a) and the cone jet mode (b).

In order to make similar measurements and to gain insight into the current being generated by different spraying conditions, a current transducer was constructed and used to monitor the current generated at the grounded MALDI target plate by the impinging charged droplets. To ensure that the electrospray was in the correct spray mode, the applied high voltage was adjusted until a nearly flat signal was achieved on the oscilloscope, where there were no large or elongated peaks in the signal as demonstrated in Figure 3.4. In Figure 3.4 the voltage from the scope is measured to be 0.04V. Since the oscilloscope has an input resistance of 1M $\Omega$ , the current generated at the probe would be 40nA according to Ohm's Law.

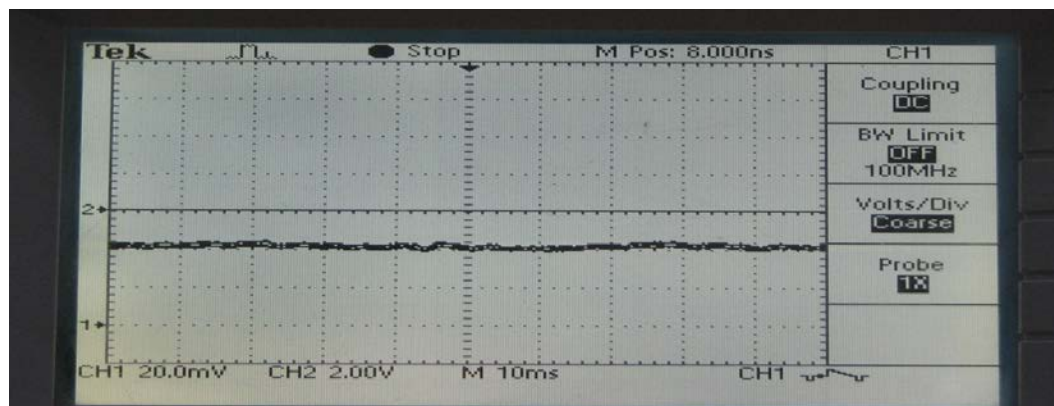


Figure 3.4: Example measurement made while spraying pure methanol a flow rate of 2.0  $\mu\text{L}/\text{min}$  from a height of 20 mm with an applied voltage of 5.4 kV, demonstrating the cone-jet mode of spraying.

It should be noted that from day-to-day or even between subsequent loadings of the syringe needle, a flat response could be generated for more than one specified voltage, flow rate and spraying distance combination; Cloupeau et al<sup>23</sup> have described this phenomenon. This is believed to be due to the inherent hysteresis in the electro spraying system. An illustration of different forms of stable sprays in the cone-jet regime is shown in Figure 3.5.

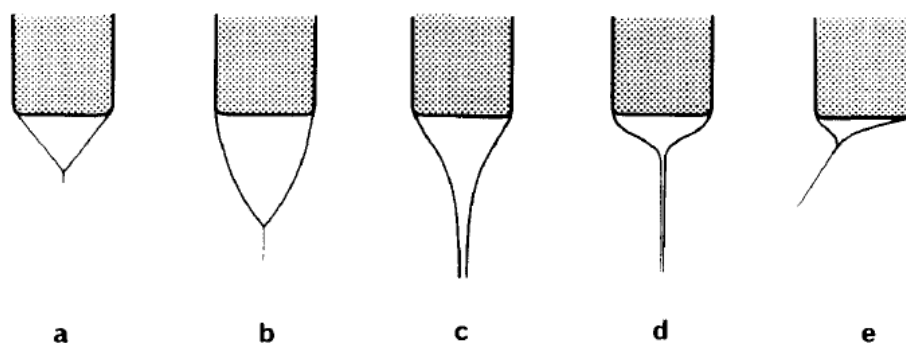
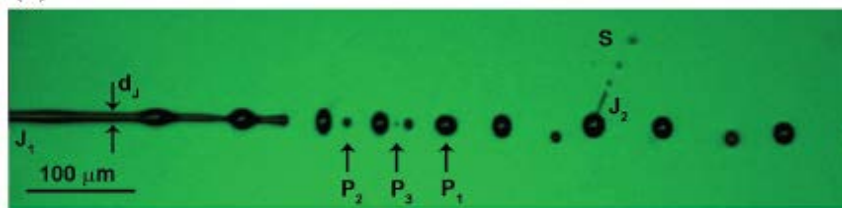


Figure 3.5: Illustration of cone shape for stable cone-jet mode electro sprays reprinted from Cloupeau et al<sup>23</sup>.

Figure 3.5 illustrates various regimes within the cone jet spraying mode. These regimes do not have clear boundaries and experimentally stable electro sprays can be made from all of them,

however, the voltages required for each regime are not the same. From experience it seems that some of these regimes exist together and certain sprays can pass back and forth between two or more of these regimes. In Figure 3.5, the cones depicted in (9b) and (9c) are generally linked. When a stable spray, like the one drawn in (9a) is formed, one can decrease the applied voltage to the spraying needle to produce a cone that resembles (9b) which is elongated with respect to (9a). If the voltage is decreased further or the cone is allowed to remain elongated, the center of this cone will begin to break down. The hydrodynamic pressure of the solvent flow through the needle causes the central area of the cone to allow more material to be ejected<sup>26</sup>. Cone breakdown results in rapid spitting by the cone that leads to spray instability and eventually into the pulsing jet regime. The cone drawn as (9d) is a result of applying more than sufficient voltage to the spraying needle and can eventually lead to the multi-jet mode. Finally, the off center spray depicted in (9e) generally arises from crystallized material in and on the needle or when the voltage is applied before a droplet is formed that covers the exposed outer diameter of the spraying needle. The overall Taylor cone size is determined by the electric field and the inner and outer diameter of the spraying needle. This combination also impacts the initial droplet size of the ejected material from the tip of the cone<sup>20, 26</sup>. An image of the formation of charged droplets at the tip of a Taylor cone in the cone jet mode is given in Figure 3.6 for the reader as reference. Of note in Figure 3.6 is the presence of small satellite droplets (10 P<sub>2</sub> and P<sub>3</sub>). These satellite droplets have been shown to have the same charge as the larger droplets (10 J<sub>2</sub>), and therefore have a greater charge density<sup>27</sup>. Figure 3.6 also shows the Coulombic fission (S) that occurs in the droplets.





**Figure 3.6: High speed camera image of the formation of initial droplets at the tip of a Taylor cone in the cone jet spraying mode. Reproduced from Nemes<sup>28</sup>.**

The main goal of this chapter is to explore the interactions of flow rate, spraying distance, spray current and electric field on the resulting ESD MALDI samples. Pure solvents and solutions containing matrix or matrix and analyte were used to make current, electric field and spray diameter measurements for samples sprayed at varying spray distances and flow rates. AFM images of the particles resulting from some of the experiments will be analyzed to visually determine the impact of the studied variables on the deposited particles.

## Experimental

Details regarding the instrumentation used in the experiments for this chapter can be found in Chapter 2. The specific details regarding sample preparation are presented here.

### *Spraying Pure Solvents*

Methanol was mixed with deionized water (18MΩcm) or isopropyl alcohol to make 100mL each of 90:10 methanol:water and 90:10 methanol:isopropyl alcohol solutions. A 1.0mL gastight syringe fitted with a luer-lock adapter (Hamilton) was used to flush the spraying tubing prior to spraying.

### *Spraying Preparation*

Two volumes of backing solvent of 1.0mL were passed through the tubing prior to spraying with different solutions and at the beginning of each experimental day. The syringe was then

filled and placed in a Harvard 22 syringe pump for controlled delivery through the spraying needle. Care was taken to ensure no air bubbles were in the tubing of the spraying system. Air bubbles in the spraying system lead to inconsistent spraying and eventual breakdown of the Taylor cone.

### ***Matrix and Sample Preparation***

DHB and CHCA were used without further purification. Stock solutions of the matrices were made at 0.1M in the final solvent composition to be sprayed. Dilutions of these stock solutions were made to obtain the final concentrations used for the spraying experiments if they were different from 0.1M.

### ***AFM Sample Preparation***

Samples for AFM analysis were sprayed onto a 10 lambda flatness gold coated front-surface mirror. The metal surface of the mirror was held at ground potential using aluminum foil to make contact between the gold surface and the grounded sample holder. A hole punch was used to create a circular area in the aluminum foil. This hole was then positioned in the center of the metal surface of the mirror and ensured that it contacted the grounded current transducer. Sprays were made for 1 minute from the specified height and at the specified flow rate. The foil was then removed and the mirror was affixed to an AFM metal probe using double sided tape.

## **Results and Discussion**

### ***Electric Field Measurements using Pure Solvents***

The first experiments conducted were aimed at understanding the effects of spraying distance and flow rate on the voltage required to form and maintain a stable cone-jet mode spray. Three solutions were sprayed from distances of 17, 25, 27, 30 and 37mm. The solutions

contained no analytes or matrix and consisted of pure methanol, methanol and water (90:10 v/v), or methanol and isopropyl alcohol (90:10 v/v). The solutions were sprayed at three different flow rates: 2.5, 5.0 and 10.0  $\mu\text{L}/\text{min}$ . The criteria used for a stable spray was a relatively flat response on the oscilloscope as previously shown in Figure 3.4.

In order to avoid the more complicated cone jet modes discussed above, the samples were allowed to flow until a droplet formed that covered the entire outer diameter of the spraying needle. Once this droplet was observed the voltage on the needle was increased from a voltage that does not induce spraying until a stable cone was formed and the oscilloscope indicated a flat response. The current was calculated from the oscilloscope once these conditions were met.

Figure 3.7 illustrates the changes in electric field observed for sprays of a MeOH solution as a function of spraying distance for three flow rates. Note that there is little difference in the electric field required for a particular spraying height when flow rates of 2.5, 5.0, and 10  $\mu\text{L}/\text{min}$  are used. This trend was consistent for all three of the solvent combinations tested. Due to this consistency, only the data for all three solvents sprayed at 5.0  $\mu\text{L}/\text{min}$  are presented in Figure 8.

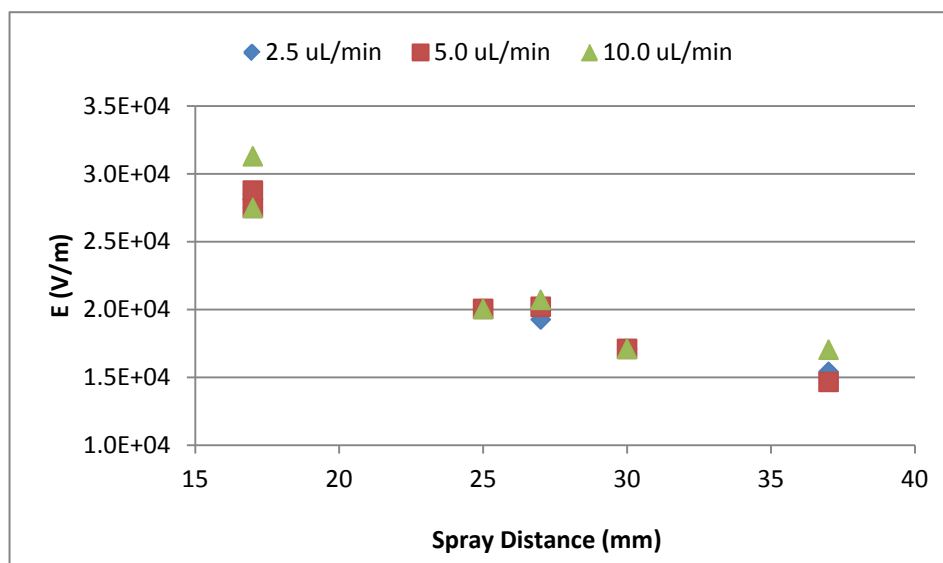


Figure 3.7: Graph showing the effect of spraying distance on the electric field required to maintain a spray in cone-jet mode. Data was collected by spraying pure MeOH at three differing flow rates.

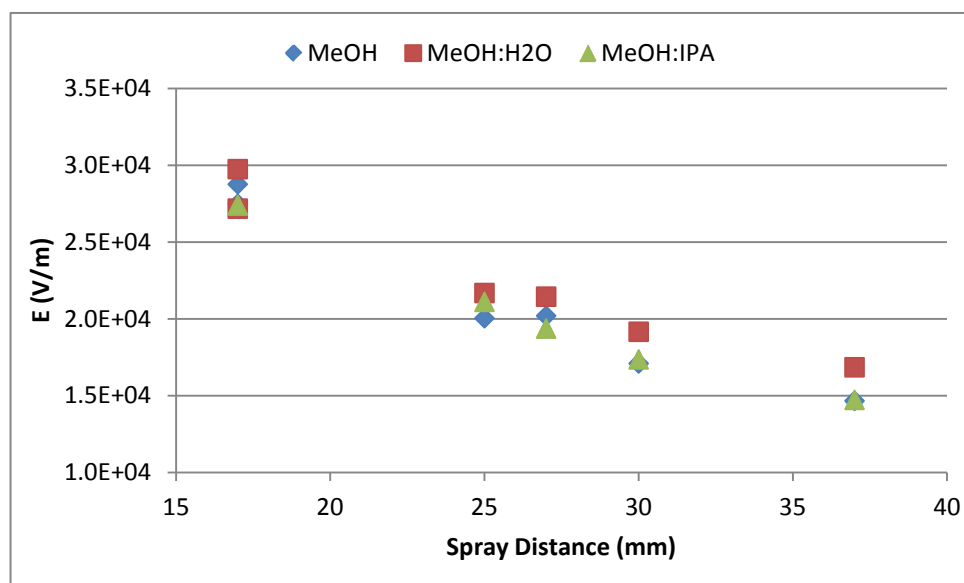
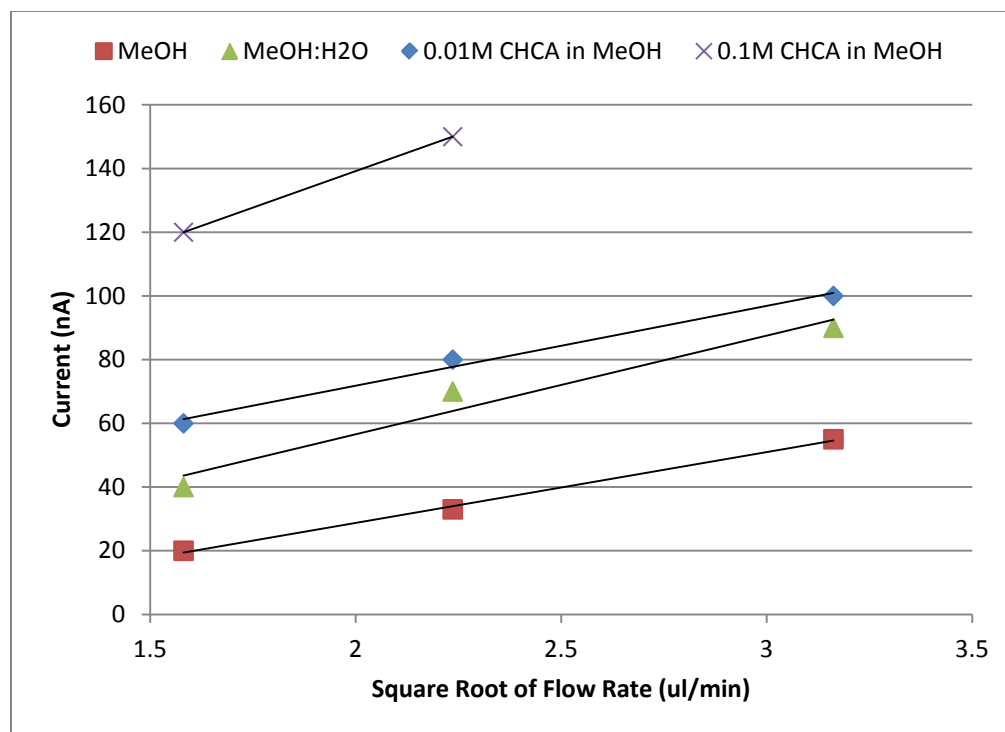


Figure 3.8: Graph showing the change in the electric field as the spraying distance is adjusted for pure solvent MeOH or 10% mixture of water or isopropyl alcohol (IPA) in MeOH. All data were collected by spraying at a constant flow rate of 5.0 uL/min.

An examination of Figure 3.8 shows that for all three sets of solvents and distances the electric field required to maintain a stable cone jet decreases with an increase in the spraying distance. What is also of interest is that the electric field values for the three solvents are similar and within the range of experimental differences that can be observed when electrospraying. As mentioned previously, there is a range of voltages that can produce a seemingly stable cone-jet for a given combination of spraying distance and flow rate. Figure 3.7 illustrates this trend for the MeOH case, where it is found that there is little difference in the electric field value required at each flow rate for a given spraying distance. Figures 11 and 12 suggest that the flow rate does not have a clear effect on the electric field required for spraying when no analyte or matrix are present. The findings from these studies will be of use if it can be shown that these observations hold constant when a matrix solution is sprayed in our apparatus. While it was expected that this would not be the case for solutions containing relatively high concentration of matrix ( $\geq 0.1\text{M}$ ), there could be some concentration level where solutions containing matrix would behave in a manner similar to a pure solvent system. To test this general hypothesis sprays containing two concentrations of analyte were made in addition to sprays of MeOH and MeOH:water solutions without analyte or matrix present. Figure 3.9 shows the results from this experiment. Note that these sprays were made from a constant height and therefore the current is plotted to aid in the visualization of the results.



**Figure 3.9:** A graph of the current measured at the grounded electrode of the spraying apparatus as a function of the square root of the flow rate flow rate ( $\mu\text{L}/\text{min}$ ) for solutions of pure solvents and solutions of MeOH containing the MALDI matrix CHCA at 0.1 and 0.01M concentrations. A stable spray for the solutions containing 0.1M CHCA in MeOH was unable to be reached, consequently the data point is not captured in the plot.

The graph in Figure 3.9 captures the current dependence of the solutions tested at three commonly used flow rates used for ESD in our group<sup>17, 21, 29</sup>. The square root of the flow rate is plotted in order to draw conclusions for the data based on equation 1 presented below. A solution of pure MeOH generates the least current at the counter electrode for our spraying apparatus, while the 0.1M CHCA solution in MeOH generates the highest current. The current generated for the 0.1M CHCA solution was not captured for the highest flow rate as a stable cone jet spray could not be produced using the voltage supply in our lab. What is of note in Figure 3.9 is that the slopes for the linear fits to the data with the exception of the 0.1M CHCA solution are similar. The differences in the slopes could be attributed to differences in the

conductivity and surface tension of the solutions. Fernandez de la Mora and Loscertales<sup>30</sup> have proposed an equation for current in an electrospray that re-enforces this observation:

$$I = f\left(\frac{\epsilon}{\epsilon_0}\right) \left(\gamma K V_t \frac{\epsilon}{\epsilon_0}\right)^{\frac{1}{2}} \quad (1)$$

In equation (1)  $I$  denotes the current observed,  $\gamma$  is the surface tension of the solvent,  $\epsilon/\epsilon_0$  is the ratio of the dielectric constant of the solvent to that of vacuum,  $K$  is the conductivity of the solution,  $V_t$  the flow rate, and  $f(\epsilon/\epsilon_0)$  is a numerical function tabulated by the authors. This equation is valid when the spray is operated in the cone jet mode with polar solvents (MeOH, water, acetonitrile, etc.) containing solutes that dissociated completely and at flow rates less than the microliter per minute range. If an assumption is made that the conductivity of the solution is determined solely by the concentration of the CHCA in solution and that all other variables were equivalent, equation 1 would predict a 3 fold increase in current in going from a solution containing 0.01M CHCA to one of 0.1M CHCA for identical flow rates. Considering the difficulty in determining the exact cone jet spraying regime one is working in and that it has already been demonstrated that a range of voltages can be found for a stable spray the graph is in decent agreement with equation 1, showing a dependence of current generated on flow rate at the counter electrode. The importance of this finding is that for a given concentration of matrix in the spraying solution Equation 1 can be used to predict the current generated at different flow rates. Further, the differences in the slopes of the lines in Figure 3.9 can be attributed to the combination of conductivity, surface tension and the dielectric constant of the solution being sprayed. Conductivity, surface tension and dielectric constants are difficult to

measure on the small volume scale used for the solutions sprayed in our laboratory. Using the slopes generated from similar plots of current as a function of flow rate for matrix compounds at various concentrations may provide insight into the similarity or differences of the spraying solutions physio-chemical properties (i.e., conductivity, surface tension, dielectric constant).

Although an understanding of the effects of flow rate and spraying distance on current generated at the counter electrode are important for our understanding and control of the electrospray deposition process, our main goal is to control the spraying diameter in order to make sample analysis by MALDI easier. In an attempt to better understand the effects of spraying distance on the spraying diameter a solution of 0.01M CHCA in MeOH was sprayed from heights of 20, 25 and 30mm at a flow rate of 2.5 $\mu$ L/min. The electric field required for a stable spray and the resultant spray diameter of those sprays are recorded in Figure 3.10. CHCA solutions were chosen for these studies in order to visualize the spray area after spraying.

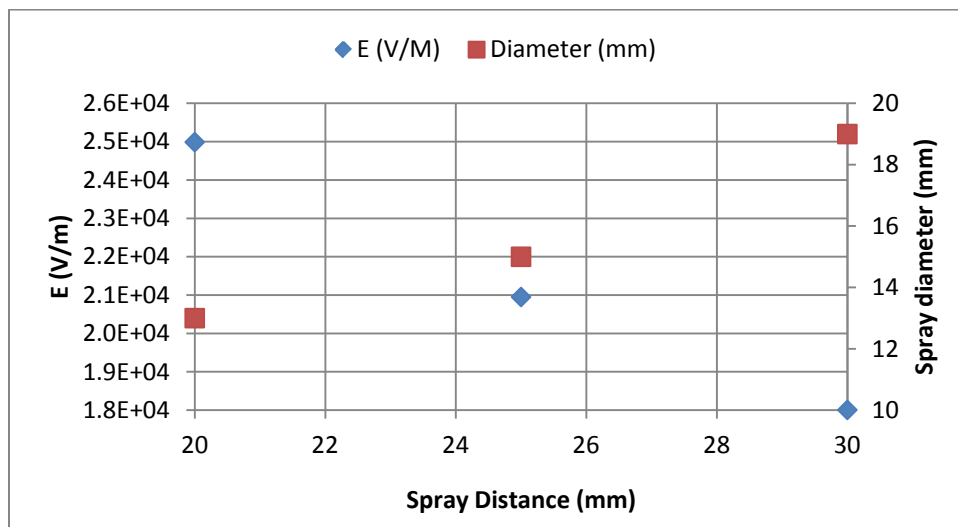


Figure 3.10: Graph showing the interactions of electric field (blue diamonds) and sprayed diameter (red squares) as the spraying height is adjusted. Sprays were made using a 0.01M solution of CHCA in MeOH with a flow rate of 2.5  $\mu$ L/min.



The graph in Figure 3.10 indicates interactions between the required electric field for a stable spray, the spraying distance and the spraying diameter of the spray. By increasing the electric field used one can decrease the diameter of the resulting spray. It should be noted that the values for these two parameters are likely to be different for other solutes and solvent combinations at the same concentration. We conclude from these data that smaller spraying diameters can be generated for sprays made from relatively small spraying distances whereby a higher electric field is required for a stable cone jet spray. With this concept in mind the following section will begin to investigate the morphology of the deposited particles as a function of spraying flow rate, spraying distance and solvent/solute identity.

### ***Sprayed Sample Morphology***

The uniformity of the sample surface of a MALDI sample is critical to the quality of the data<sup>6</sup>. The shot-to-shot reproducibility of a MALDI sample should be maximized when the interrogated surface is comprised of a homogenous coating of the dried solution on the sample probe. In order to control and reduce the spraying diameter during sample preparation one needs to spray from a shorter distance to the sample probe. The process of the liquid droplets drying into solid particles while travelling towards the sample probe is of critical importance. The voltage used for spraying, along with the flow rate, solute concentration and spraying distance, influence the size and charge of the initial droplets formed at the end of the Taylor cone<sup>31, 32</sup>. These variables along with the spraying chamber gas identity, temperature and relative humidity in the spraying chamber are then expected to affect the “dryness” of the particles that collect on the MALDI sample target. In the studies presented here the spraying atmosphere was not controlled for temperature or humidity, though it is the experience of our lab that high humidity conditions lead to higher variability in the sprayed samples as measured by the MALDI signal response. The dryness of the particles deposited on the target plate will

determine the resulting morphology of the particles on the surface<sup>33-35</sup>. For the purposes of this thesis, the term “morphology” will be used in two different contexts. The first will be termed “gross morphology”, which will refer to the shape and size of the total sprayed sample. The second term, “particle morphology”, will refer to the size, shape and distribution of the dried particles on the sample surface.

To begin, it is first necessary to define the experimental factors believed to affect the particle morphology by affecting the initial electrospray droplet diameter<sup>32, 33, 36</sup>. **Error!** **Reference source not found.** details the factors that can be attributed to the spraying apparatus and those that are largely dominated by the spraying solution and its chemical characteristics<sup>27</sup>. Voltage and spraying mode will not be investigated here, as noted in the earlier parts of this chapter, the current output at the grounded electrode is monitored to assure the spray is in the cone-jet mode. Similarly the shape of the cone was held constant by visual inspection. Further, voltage is easily quantifiable yet as has been noted, there is a range of acceptable voltages for the generation of a stable cone jet spray. The voltage for these studies was set near the onset of a stable spray, but was not optimized for each solution or held constant for all solutions. The reason for the omission of these parameters as well as many of the solution variables arose from the difficulties in obtaining the measurements on limited volume samples (1.0mL or less) and the variability of voltage measurements and cone shapes and sizes. Finally the spray needle diameter (both inner and outer) and composition were held constant for all experiments. The diameter is of critical importance to the size of the cone formed and therefore the initial droplet size<sup>27</sup>, thus the data presented here should be taken in context with the apparatus used as described in Chapter 2.

**Table 3.1: Factors effecting the sample morphology of electrosprayed MALDI samples. This list has been collected from various articles<sup>23, 27, 30, 32, 33</sup>.**

Spray Apparatus	Flow rate
	Spraying distance
	Voltage
	Spraying mode
	Spray Time
	Diameter of the spraying needle
	Composition of the spraying needle
	Humidity in spraying chamber
	Identity of the gas in the spraying chamber
	Temperature of chamber
Solution Variables	Solvent identity
	Solute concentration
	Viscosity
	Vapor Pressure of the solvent
	Conductivity
	Surface tension
	Permittivity

The diameter of the droplet defines the volume of liquid that is contained within the droplet. Therefore, the droplet size or diameter will affect the resulting solute particle morphology and the sprayed diameter<sup>31, 33</sup>. An experimentally derived equation for the initial droplet diameter formed in the cone jet mode has been presented by Ganan-Clavo<sup>32</sup>.

$$d = 3.78 * 0.6\pi^{\left(-\frac{2}{3}\right)} * Q^{\frac{1}{2}} * \left(\frac{\rho\epsilon_0}{\gamma K}\right)^{\frac{1}{6}} \quad (2)$$

In equation 2,  $d$ ,  $\rho$ ,  $\epsilon_0$ ,  $Q$ ,  $\gamma$ , and  $K$  are the initial droplet diameter at the needle tip, density of the spraying solution, electrical permittivity of vacuum, flow rate, surface tension and conductivity of the solution, respectively. In this equation the experimental term with the most influence on the resulting droplet diameter is the flow rate. It is important to note that the solution properties also affect the droplet diameter, but as shown in Figure 3.8, solutions

containing different solute concentrations and solvent identities could be made to perform similarly if the conductivity, dielectric constant and surface tensions for the sprayed solutions were similar. An investigation was made to determine if Equation 2 could also be used to predict the resultant sprayed diameter from sprays made at differing heights and flow rates. Larger droplets would have smaller velocities in the electric field as their velocity is determined by the electric field between the needle and sample plate. Therefore any droplet emitted from the tip at an angle not at  $90^\circ$  from the sample surface may be translated further from the center of the spray resulting in a larger observed spray diameter. A solution of 0.01M CHCA in MeOH was sprayed from heights of 20, 25 and 30mm at flow rates of 2.5, 5.0 and 10.0 $\mu$ L/min. The sprays were maintained for  $\sim$ 1.0 minute and then the diameter in millimeters of the resulting visual spray was measured using a standard ruler. The results of this study are shown in Figure 3.11.

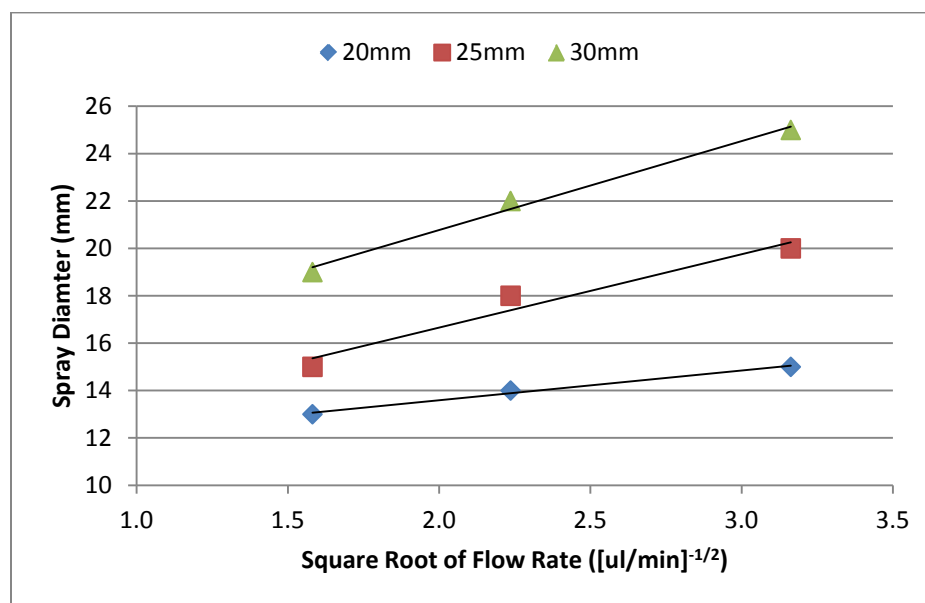


**Figure 3.11:** Graph showing the effect of the square root of the flow rate on the observed sprayed diameter. The data are presented at three spraying flow rates 2.5, 5.0, and 10.0 $\mu$ L/min and three spraying heights 20, 25, and 30mm. The spraying solution was 0.01M CHCA in MeOH.

Figure 3.11 supports the hypothesis that the sprayed diameter is directly related to the initial droplet diameter by flow rate, but there is also an affect of the spraying distance. A linear

trend appears within a given spraying distance for the spraying diameter as a function of the square root of the flow rate. The slopes of the fitted lines presented in Figure 3.11 are not equal. Thus we can say that the sprayed diameter is proportional to the flow rate and the spraying distance. The data presented are consistent with what can be expected from simple physical models of a charged particle in an electric field and consistent with observations made in the literature<sup>31, 36</sup>. As the spraying distance is increased the deposited area also increases. The charged particles created during the cone break-up spend a longer time in the electric field and therefore can be translated farther along the orthogonal spraying axis by a combination of interaction with the electric field and Coulombic repulsion between the droplets. The droplets generated at the tip of the Taylor cone are not uniform in size, they have been found to vary by a factor of two for pure methanol solution; however, this range will be larger for solutions with higher electrical conductivity<sup>37</sup>. Further, all droplets will undergo Coulombic fission as the solvent in the droplet evaporates and the charge density on the surface of the droplet increases sufficiently<sup>28</sup>. If no other spraying conditions are changed, the same flow rate should generate the same droplet size population and an increase in spraying height allows those droplets to spread further, increasing the observed sprayed diameter.

Knowledge of the dependence of the spray diameter on spraying distance and spraying flow rate is important to controlling the electrospray deposition process. Previous work in our group<sup>16, 21</sup> has demonstrated that the center of the sprayed area produces the highest precision and signal intensity when the samples are used for MALDI-TOFMS experiments. The center of a large spray (diameter of 10-25mm) is difficult to find reproducibly in the camera view of commercial MALDI instruments. Thus if the sprayed diameter could be controlled and reduced further, it may be possible to consistently obtain highly precise MALDI results.

Since flow rate and spraying distance influence the spray diameter, it is important to understand the effects of the two parameters on the microscopic morphology of the deposited particles. To accomplish this, atomic force microscopy (AFM) was used to image samples sprayed at two different spraying heights and two different spraying flow rates. The heights and flow rates chosen were 20 and 30mm, and 2.5 and 5.0uL/min respectively. These values were chosen because they represent typical conditions for spraying that have been used in our lab<sup>17, 21, 29</sup>. The samples imaged with AFM were the result of spraying a sample of 0.02M 2,5-DHB in MeOH for the flow rate studies and 0.02M CHCA in MeOH for the spray height study. While the solute-solvent combination is likely important to the morphology observed on the surface<sup>21</sup>, these experiments were conducted to determine the relative differences in the spraying parameters noted above. While it is likely the absolute morphology will be different for the two solutes chosen, one can expect that the trends will be consistent. In order to better image the particle size and distribution for the flow rate studies the material was sprayed for ~15 seconds. The height study samples were sprayed for ~2.0 minutes.

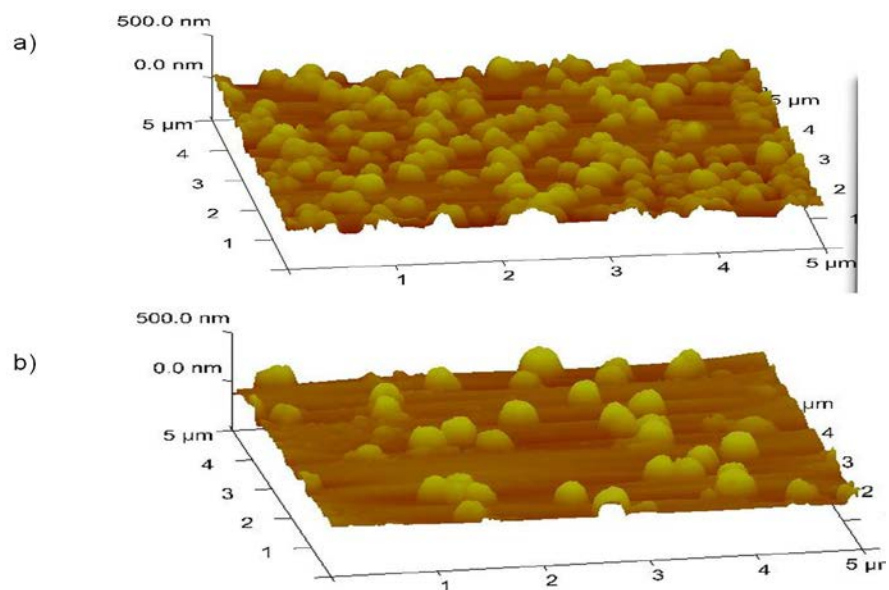


Figure 3.12: AFM images of 0.02M 2,5-DHB in methanol sprayed from 20mm at flow rates of a) 2.0uL/min and b) 5.0uL/min.

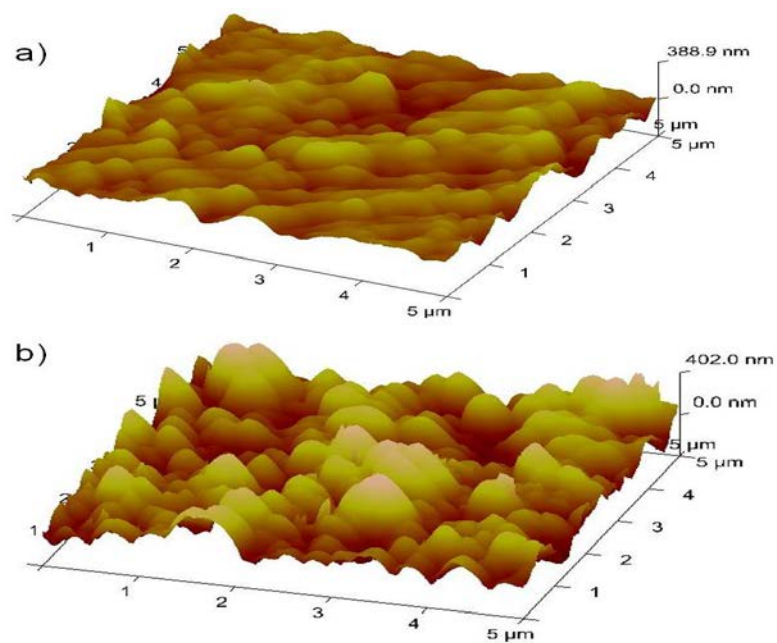
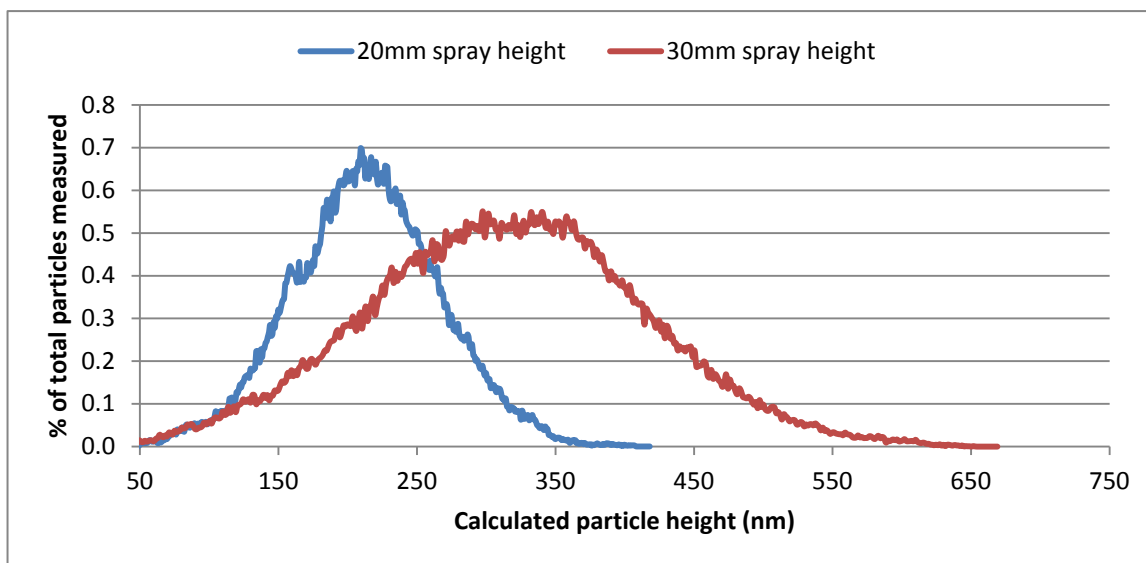


Figure 3.13: AFM images of 0.02M CHCA in Methanol using a flow rate of 2.0uL/min and sprayed from a) 20 mm and b) 30mm.

Figure 3.16 shows the images obtained when samples of the same composition are sprayed from the same spraying distance at two flow rates. The total number of particles is increased when the flow rate is decreased. This is accompanied by visually smaller particle size in the deposited material. The higher flow rate produces fewer but larger particles on the surface. This evidence also supports the sprayed diameter data presented above. Smaller initial droplets would have a higher initial charge density on the surface of the droplet and be expected to fission sooner, producing more droplets, and the smaller droplets would also have a lower momentum in the axial direction, allowing them to be translated further from the center of the spray. Further, the spraying height also affects the particle size observed in the AFM. In Figure 3.13 the particles deposited from the higher spraying distance visually look larger than those sprayed from the shorter distance. The hypothesis for why this phenomenon occurs involves the solubility of the matrix in the solvent used as well as the chemical characteristics of the solvent, mainly the vapor pressure of the solvent in the spraying atmosphere<sup>38</sup>. If the droplets decrease in volume to a point that the solute reaches a critical solubility necessary for nucleation the solute will begin to crystallize. Extensive crystallization of the solute in the droplet leads to formation of a “crust” or shell on the droplet<sup>38,39</sup> that dampens the shear force on the droplet upon impact with the grounded metal surface. If the drying rate of a droplet affects its behavior upon deposition two things should be observable aside from larger diameter droplets on the surface. First, for any given flow rate and solvent-solute combination there should exist a spraying distances where one can observe “wetter” and “drier” particles on the surface<sup>39</sup>. Similarly, the flow rate should be able to be modulated for a fixed height and produce the same effect. This case will be covered in Chapter 4 and therefore we shall focus on the second observable herein. The second observable should be an overall increase in the height of the particle when measured normal to the surface. This would imply that the particle was not



only drier but also less compressible when it impacted the surface. Figure 3.14 is a graphic exported from the AFM software that measures the depth of the features in the image.



**Figure 3.14:** Graph showing the height distribution of particles deposited from electro spraying samples of 0.02M DHB in MeOH from 20mm and 30mm

When the sample solution is sprayed from a height of 30mm versus 20mm a clear shift in the depth, and therefore, the height of the particles is observed. At a 20mm spraying distance there is a mostly Gaussian distribution of heights centered around ~210nm, while for the 30mm spraying distance the center of the distribution is shifted to a larger value around 375nm. Again this suggests that the particles are less affected by the impact at the surface and are therefore “firmer” than the particles sprayed from a shorter spraying distance. It is also of note that the distribution of particle heights is larger at a spraying distance of 30mm. This result is intriguing, but at present the cause is unknown.

To determine if the sample particle morphology is affected by the specific combination of solute and solvent, 2,5-DHB was prepared at a concentration of 0.02M in four solvent

combinations. The solvent combinations chosen were methanol, acetonitrile, methanol:acetonitrile (1:1), and methanol:chloroform (1:1).

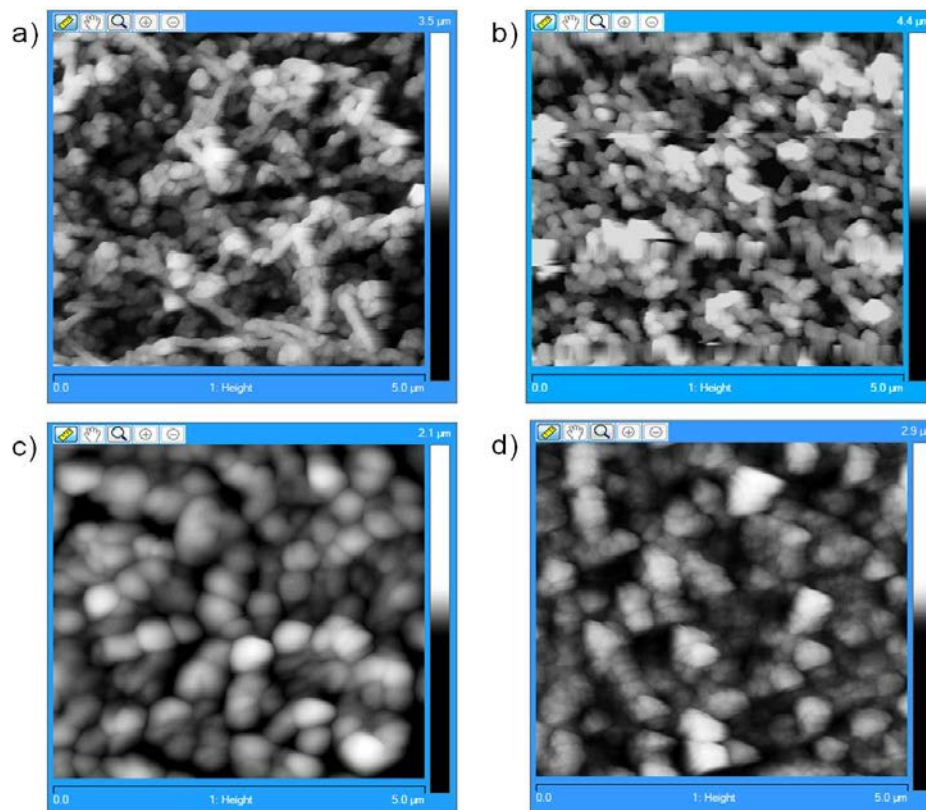


**Figure 3.15: Atomic Force Microscopy (AFM) images of electrosprayed samples. The samples of 0.02M 2,5-DHB dissolved in a) MeOH, b) MeCN, c) MeOH:CHCl<sub>3</sub> (1:1), and d) MeOH:MeCN (1:1) were sprayed at a flow rate of 2.0uL/min from a distance of 20mm.**

The four solvent combinations produced different morphologies as visualized by AFM when they were sprayed using the same flow rates and spraying distance, 2.0uL/min and 20mm. In Figure 3.15 the MeOH:CHCl<sub>3</sub> (19c) and MeOH:MeCN (19d) samples appear to have the least similar morphologies. The MeOH:CHCl<sub>3</sub> sample appears to have deposited large intact solid particles on the sample surface. The sample sprayed from MeOH (19a) shows what appears to be a network of interconnected solid droplets, while the sample sprayed from MeCN (19b) shows a similar network, but the particles appear to be discrete clusters of droplets and are less

interconnected. This may suggest that the spray made using MeOH deposited “wetter” droplets on the surface. The images from the AFM are not of high enough resolution to gauge the true morphology of the individual particles in Figure 3.15 (a) and (b). The lack of resolution for these samples likely arises from measuring amorphous particles of organic materials. Amorphous organic solids are less rigid when compared to metal or silicon surfaces (the typical surfaces used for AFM imaging) and therefore are more compressible, which decreases the image resolution. Also, relatively large variations in height across the area measured ( $10 \times 10 \mu\text{m}$ ) in tapping mode on the AFM does not allow for the best resolution capable on the instrument. Even with the limited resolution, the images show qualitative differences in the morphology of the sprayed material when flow rate and spraying distance and solvent-solute identity are adjusted. The impacts of these differences with regard to the MALDI performance of the samples will be further discussed in Chapters 4 and 6.

Finally, to gain insight into the previous data obtained in our lab regarding the MALDI precision observed as a function of position on the deposited spot<sup>16</sup>, images of the center and the outer edges of the deposited spots were taken using AFM. The same samples that were used to obtain the images presented in Figure 3.15 were used for this purpose. Figure 3.16 shows a progression of particle images collected from the center of a spray to the outer most edge of the spray.

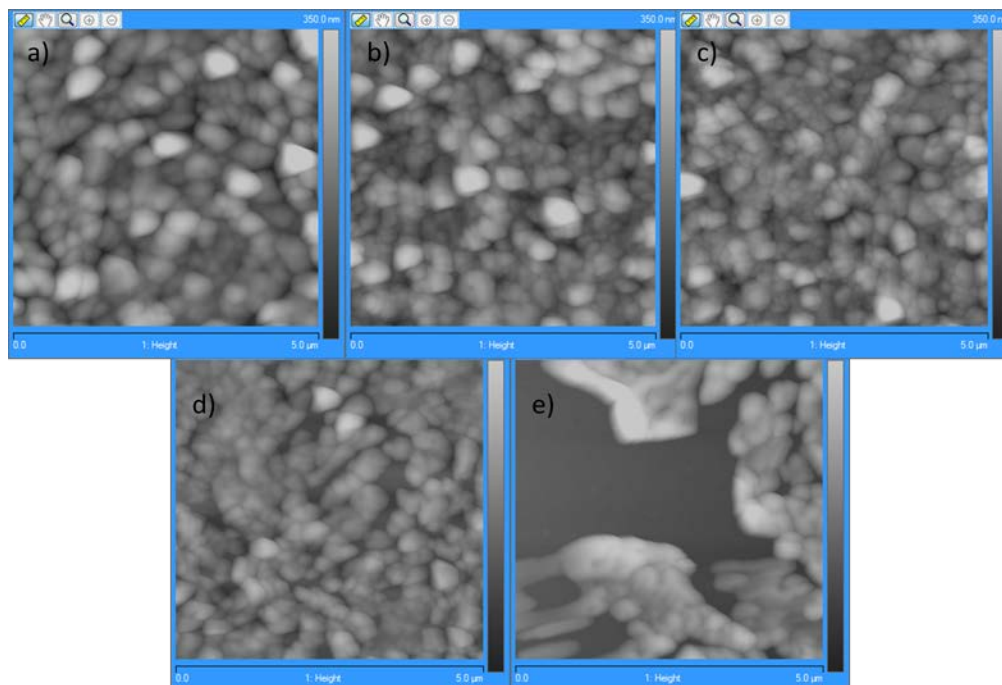


**Figure 3.16:** AFM images of a 0.02M DHB sprayed from a MeOH:Chloroform solution. Images a-f were taken at different locations on the spot. Image a) represents the center of the spot and the images progress outward to f, which is the outer most edge of the spot.

In Figure 3.16 d and e the occurrence of incomplete matrix coverage at the outer most edge of the sprayed sample can be observed. The effect of probe surface coverage on MALDI signal has been investigated in our group<sup>21</sup>. Those findings suggest that precision and signal are increased if the metal probe surface is completely covered by the matrix and analyte material. Incomplete coverage of the surface is the likely cause of the poor precision observed at the edges of the spots that was previously report by our group<sup>16</sup>.

## Conclusions

The data presented in this chapter help to better define the characteristics of the spraying process that determine the sprayed diameter for ESD sample preparation. The nature of the spraying solution, including the solvent composition and initial solute concentration, are important factors to consider when designing a spraying solution for MALDI experiments. The

effects of these factors on the analyte signal observed in the MALDI experiment will be considered further in Chapters 4 and 6. The spraying height and flow rate can be modulated to define a spraying diameter that is either large or small. The addition of a current transducer was shown to aid in the ability to produce more consistent cone jet sprays that lead to higher precision in the MALDI experiment. It is also important to note that this work was done using the traditional set-up for electrospray deposition, a technique that will be given no further consideration in this thesis. Shortly after these data were collected a newer method of electrospray deposition was realized that eliminates the need for modulating the spraying diameter. The lessons learned from the current transducer were carried over for the newer technique, but much of the morphology work was re-examined under the new spraying conditions. Future directions for this work on what will now be termed “uncontrolled” electrospray deposition will be examined in the future works chapter of this thesis.

## References

1. Zhang, J.; Kinsel, G. R., Quantification of Protein-Polymer Interactions by Matrix-Assisted Laser Desorption/Ionization Mass Spectrometry. *Langmuir* 2002, 18 (11), 4444-4448.
2. Bansal, S. S.; Halket, J. M.; Fusova, J.; Bomford, A.; Simpson, R. J.; Vasavda, N.; Thein, S. L.; Hider, R. C., Quantification of hepcidin using matrix-assisted laser desorption/ionization time-of-flight mass spectrometry. *Rapid Communications in Mass Spectrometry* 2009, 23 (11), 1531-1542.
3. Bizzarri, M.; Cavaliere, C.; Foglia, P.; Guarino, C.; Samperi, R.; Lagana, A., A label-free method based on MALDI-TOF mass spectrometry for the absolute quantitation of troponin T in mouse cardiac tissue. *Analytical and Bioanalytical Chemistry* 2008, 391 (5), 1969-1976.
4. Nishikaze, T.; Amano, J., Reverse thin layer method for enhanced ion yield of oligosaccharides in matrix-assisted laser desorption/ionization. *Rapid Communications in Mass Spectrometry* 2009, 23 (23), 3787-3794.
5. Szyszka, R.; Hanton, S. D.; Henning, D.; Owens, K. G., Development of a Combined Standard Additions/Internal Standards Method to Quantify Residual PEG in Ethoxylated Surfactants by MALDI TOFMS. *Journal of the American Society for Mass Spectrometry* 2011, 22 (4), 633-640.
6. Hanton, S. D., Owens, K. G., MALDI MS Applications for Industrial Polymers. In *MALDI Mass Spectrometry for Synthetic Polymer Analysis*, Li, L., Ed. John Wiley & Sons, Inc.: New York, 2010.

7. Nicola, A. J.; Gusev, A. I.; Proctor, A.; Jackson, E. K.; Hercules, D. M., Application of the fast-evaporation sample preparation method for improving quantification of angiotensin-ii by matrix-assisted laser-desorption ionization. *Rapid Communications in Mass Spectrometry* 1995, 9 (12), 1164-1171.
8. Garaguso, I.; Borlak, J., Matrix layer sample preparation: An improved MALDI-MS peptide analysis method for proteomic studies. *Proteomics* 2008, 8 (13), 2583-2595.
9. Zheng, J.; Li, N.; Ridyard, M.; Dai, H.; Robbins, S. M.; Li, L., Simple and robust two-layer matrix/sample preparation method for MALDI MS/MS analysis of peptides. *Journal of Proteomics Research* 2005, 4 (5), 1709-1716.
10. Zhang, N.; Doucette, A.; Li, L., Two-layer sample preparation method for MALDI mass spectrometric analysis of protein and peptide samples containing sodium dodecyl sulfate. *Analytical Chemistry* 2001, 73 (13), 2968-2975.
11. Keller, B. O.; Li, L., Three-layer matrix/sample preparation method for MALDI MS analysis of low nanomolar protein samples. *Journal of the American Society for Mass Spectrometry* 2006, 17 (6), 780-785.
12. Chen, Y. F.; Allegood, J.; Liu, Y.; Wang, E.; Cachon-Gonzalez, B.; Cox, T. M.; Merrill, A. H.; Sullards, M. C., Imaging MALDI mass spectrometry using an oscillating capillary nebulizer matrix coating system and its application to analysis of lipids in brain from a mouse model of Tay-Sachs/Sandhoff disease. *Analytical Chemistry* 2008, 80 (8), 2780-2788.
13. Yao, J.; Scott, J. R.; Young, M. K.; Wilkins, C. L., Importance of matrix:analyte ratio for buffer tolerance using 2,5-dihydroxybenzoic acid as a matrix in matrix-assisted laser desorption/ionization-fourier transform mass spectrometry and matrix-assisted laser desorption/ionization-time of flight. *Journal of the American Society for Mass Spectrometry* 1998, 9 (8), 805-813.
14. Dally, J. E.; Gorniak, J.; Bowie, R.; Bentzley, C. M., Quantitation of underivatized free amino acids in mammalian cell culture media using matrix assisted laser desorption ionization time-of-flight mass spectrometry. *Analytical Chemistry* 2003, 75 (19), 5046-5053.
15. Holcomb, A.; Owens, K. G., Optimization of a modified aerospray deposition device for the preparation of samples for quantitative analysis by MALDI-TOFMS. *Anal. Chim. Acta* 2010, 658, 49-55.
16. Hensel, R. R.; King, R. C.; Owens, K. G., Electrospray sample preparation for improved quantitation in matrix-assisted laser desorption/ionization time-of-flight mass spectrometry. *Rapid Communications in Mass Spectrometry*. 1997, 11, 1785-1793.
17. Chavez-Eng, C. M. Quantitative aspects of matrix-assisted laser desorption/ionization using electrospray deposition. PhD, Drexel University, Philadelphia, 2002.
18. Hanton, S. D.; Hyder, I. Z.; Stets, J. R.; Owens, K. G.; Blair, W. R.; Guttman, C. M.; Giuseppetti, A. A., Investigations of electrospray sample deposition for polymer MALDI mass spectrometry. *Journal of the American Society for Mass Spectrometry* 2004, 15, 168-179.
19. Mahan, A., Owens K. G., MALDI Sample Preparation - The Use of Bioma MS Imaging to Study Electrospray Sample Deposition. *Proceedings of the Annual Meeting of the American Society of Mass Spectrometry Meeting* 2008.
20. Marginean, I.; Parvin, L.; Heffernan, L.; Vertes, A., Flexing the Electrified Meniscus: The Birth of a Jet in Electrosprays. *Analytical Chemistry* 2004, 76 (14), 4202-4207.
21. Szyszka, R. Exploration of the fundamentals and quantitative applications of matrix assisted laser desorption ionization time-of-flight mass spectrometry (MALDI-TOFMS) in polymer analysis. PhD, Drexel University, Philadelphia, 2012.

22. Juraschek, R.; Rollgen, F. W., Pulsation phenomena during electrospray ionization. *International Journal of Mass Spectrometry* 1998, *177* (1), 1-15.
23. Cloupeau, M.; Prunet-Foch, B., Electrohydrodynamic spraying functioning modes: a critical review. *Journal of Aerosol Science* 1994, *25* (6), 1021-1036.
24. Marginean, I.; Nemes, P.; Vertes, A., Order-Chaos-Order Transitions in Electrospays: The Electrified Dripping Faucet. *Physical Review Letters* 2006, *97* (6), 064502-4.
25. Erb, W. J.; Owens, K. G., Development of a dual-spray electrospray deposition system for matrix-assisted laser desorption/ionization time-of-flight mass spectrometry. *Rapid Commun. Mass Spectrom.* 2008, *22*, 1168-1174.
26. Vertes, A.; Irinyi, G.; Gijbels, R., Hydrodynamic model of matrix-assisted laser desorption mass spectrometry. *Analytical Chemistry* 1993, *65*, 2389-93.
27. Rosell, J. Size characterization in electrospays of submicron droplets. Yale University, 1994.
28. Nemes, P.; Marginean, I.; Vertes, A., Spraying Mode Effect on Droplet Formation and Ion Chemistry in Electrospays. *Analytical Chemistry* 2007, *79*, 3105-3116.
29. Erb, W. J. Exploration of the fundamentals of matrix assisted laser desorption/ionization time-of-flight mass spectrometry. PhD thesis, Drexel University, Philadelphia, 2007.
30. Delamora, J. F.; Loscertales, I. G., The current emitted by highly conducting Taylor cones. *Journal of Fluid Mechanics* 1994, *260*, 155-184.
31. Rietveld, I. B.; Kobayashi, K.; Yamada, H.; Matsushige, K., Electro spray Deposition, Model, and Experiment: Toward General Control of Film Morphology. *The Journal of Physical Chemistry B* 2006, *110* (46), 23351-23364.
32. Ganan-Calvo, A. M., Cone-jet analytical extension of Taylor's electrostatic solution and the asymptotic universal scaling laws in electro spraying. *Physical Review Letters* 1997, *79*, 217-220.
33. Rietveld, I. B.; Kobayashi, K.; Yamada, H.; Matsushige, K., Model supported morphology control of electrospray deposited poly(vinylidene fluoride) film. *Macromolecular Symposium* 2007, *249/250*, 322-329.
34. De, W. K.; Van, V. S.; Buschop, H.; Dubruel, P.; Vekemans, B.; Schacht, E.; Vincze, L.; Adriaens, A., Surface characterization of a cross-linked cytochrome c film on cysteamine-modified gold electrodes. *Surface and Interface Analysis* 2009, *41*, 389-393.
35. Matsushima, Y.; Yamazaki, T.; Maeda, K.; Noma, T.; Suzuki, T., Morphology of SnO<sub>2</sub> layers prepared by the electro spraying pyrolysis method. *Journal of the Ceramic Society of Japan* 2006, *114* (1336), 1121-1125.
36. Tang, K. The electrospray: fundamentals and feasibility of its application to targeted drug delivery by inhalation. PhD, Yale University, New Haven, 1994.
37. Kebarle, P.; Tang, L., From ions in solution to ions in the gas phase - the mechanism of electrospray mass spectrometry. *Analytical Chemistry* 1993, *65*, 972A-986A.
38. Baumgärtner, F.; Schauer, C., On the formation mechanism of hollow-sphere aerosols. *Journal of Aerosol Science* 1989, *20* (8), 879-882.
39. Leong, K. H., Morphology of aerosol-particles generated from the evaporation of solution drops. *Journal of Aerosol Science* 1981, *12* (5), 417-435.

## **Chapter 4. Development and Characterization of a Controlled Electropray Deposition Sample Preparation Method**

### **Introduction**

Electropray deposition sample preparation has been shown to produce high precision in MALDI-TOFMS<sup>1-4</sup>. However, there is a need to further understand the spraying process and the key variables that are important in the technique so that the full potential of ESD can be achieved. In order to accomplish this goal, one must first determine what variables in the process can lead to inconsistent sprays. It is clear that the spraying parameters that have already been discussed (Chapter 3) influence the spraying area deposited on the sample probe. The central area of the circular spray produces mass spectra with the largest signal and highest reproducibility<sup>1</sup>. Variations in the sprayed area can lead to imprecision when inter-sample results are compared, as it may be difficult to sample the same area of two independent sprays in the mass spectrometer.

As was discussed in Chapter 3 the other main factor affecting the sprayed area that may not be easily controlled by the user is the spraying mode. The spraying mode can be affected by a number of factors including spraying flow rate, spraying distance, spraying voltage, and the concentration and physio-chemical properties of the material being sprayed<sup>5-7</sup>. Using a current transducer and an oscilloscope one can track the spraying mode and normalize the voltage between sprays in order to increase spray-to-spray repeatability<sup>7</sup>.

As described previously in Chapter 2, ESD is typically performed with a bare SS target plate held at ground potential. For matrices or samples that produce transparent particles on the surface of the probe, it is often difficult to define where the sample resides on the SS



surface. This particular issue was noticed in our group when a low concentration sample of CsI in methanol was electrosprayed onto a SS metal probe. The resulting sprayed material was mostly transparent and hard to locate visually when placed into the MALDI instrument. To help increase the contrast of the sprayed CsI on the target a piece of black electrical tape was applied to the SS plate. The resulting spray produced a unique effect not before observed in our group. The sample did not spray onto the tape, but rather was deposited at the edges of the electrical tape where the metal was not covered. After being repeated numerous times it became clear that the material from the electrospray was being deposited on the bare metal only and not being deposited on the surface of the electrical tape.

Initially it was not known why this phenomenon was occurring, but we sought to take advantage of the effect for this experiment. The entire metal surface of the probe was covered in electrical tape and then a small (approximately 2mm diameter) hole was cut in the tape. The metal surface was then cleaned with a solution of methanol and water (90:10) to remove any adhesive residue. ESD was then performed using CsI in a methanol: water solution (90:10). The resulting spray appeared to be confined to the area of the metal target that was exposed and not on the other covered areas. The metal probe covered with the tape was loaded into the instrument to demonstrate that the material was not sprayed on the tape, but rather deposited solely onto the exposed metal surface. Spectra from the area not covered by the tape produced measurable ion intensities for CsI, while the area that was taped yielded no ion signal. Once it was confirmed that the area of the probe that was taped did not yield any ions, the common practice was to remove the tape prior to analyzing the samples in the instrument, as the clearance between the plate surface and the IS2 plate in the source of the instrument is small and any contact between the tape and the high voltage plate might lead to instrument failure.

The source of the black electrical tape that produced these original controlled sprays could unfortunately not be determined. Therefore a survey of commercially available electrical tape was made to find a comparable replacement. A list of the tapes tested is found in **Error! Reference source not found.** along with some of their stated physical characteristics. Additional experiments with these tapes demonstrated that not all black electrical tape would produce a similar effect as the first lot tested with the CSI experiments. Many of the tapes could be sprayed onto when a single layer of the tape was applied to the metal probe. However, it was observed that with the addition of several layers of tape, the controlled spray effect could be reproduced. Figure 4.1 below shows what a probe with an insufficient tape looked like as compared to one with a sufficient amount of tape to produce the desired effect.

**Table 4.1: List of commercial electrical tapes used to test in the controlled electrospray deposition apparatus and their stated properties.**

Commercial Name	Manufacturer	Thickness	Reported Dielectric Breakdown	Experimental observables
Frost King	Global Industries	0.18mm	9000V	Required 3-4 layers of tape to direct the spray
Scotch super 33+	3M	7mil	8000V	Required 3-4 layers of tape to direct the spray
Scotch super 88	3M	8.5mil	10000V	Required 2-3 layers of tape to direct the spray
2228 moisture sealing electrical tape	3M	65mil	12000V	Worked with a single layer of tape, but was difficult to cut through.

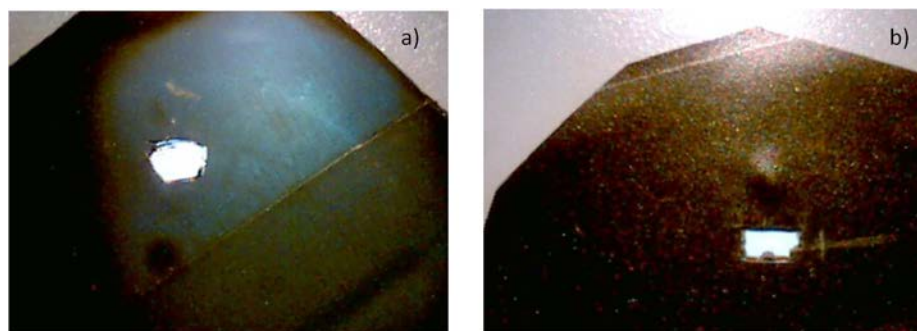


**Figure 4.1: Images of two individual controlled ESD experiments using CHCA as a matrix showing a) a probe that was not sufficiently insulated with a single layer of electrical tape and b) a probe with multiple layers of tape with sufficient insulation to direct the sprayed material onto the exposed metal surface and not the taped area.**

The example shown in Figure 4.1 suggests that the property that enables controlled electro spray to work is the electrical permittivity of the material. Electrical permittivity is a measure of a material's resistance to forming an electric field. Low permittivity materials will not transmit an electric field through the material. Therefore it was hypothesized that any material with a sufficiently low electric permittivity could work in the controlled electro spray apparatus. Another factor that could affect the ability of a material to be used for controlled electro spray would be the ability of the material to form a surface charge in an electric field. Plastics, such as PTFE, are known to surface charge when placed in an electric field. The surface charging of the material would create localized electric fields near the surface of the tape that might direct the charged particles toward the grounded exposed metal surface. This phenomenon would be similar to a technique described by Salim and co-workers<sup>8</sup>, whereby they applied a gold layered PDMS mask above the metal surface of the electro spraying counter electrode. The mask was charged by applying a voltage across the surface. Their work contained simulations that demonstrated a localized electric field at the surface of the mask that directed

charged particles of polymer into holes in the mask allowing access to the grounded metal surface.

Since the process of determining the necessary amount of tape for each lot or brand of tape to enable the controlled electro spraying process would be time consuming, we sought to find other materials that would perform similarly to the electrical tape with a single layer application. Other materials that proved successful in directing the charged particles onto the exposed metal surface only were Whatman PTFE membrane filters (polypropylene backed, 0.5 $\mu$ m pore size catalog No. 7585-004), Nylon 66 membranes (Alltech Associates Inc. catalog No. 2050), and clear Scotch-brand packaging tape (3M-371, 3.1mil thick, polypropylene backing, synthetic rubber adhesive). Commercially available Scotch tape is inexpensive and easy to apply to the metal surface. Its transparency also makes it easier to excise the appropriate area on the probe corresponding to the defined target spot on the surface. Further studies to refine the technique and further characterize the controlled ESD process was conducted with the clear Scotch brand tape unless otherwise noted.

This chapter will detail experiments aimed at determining the effects of ESD variables on the resultant particle morphology and MALDI performance using the controlled ESD device. First the development of an optimized sample spraying routine will be discussed. The lessons learned from these experiments will be used to investigate the gross morphology of the deposited sample area as well as the morphology of the individual particles. Key factors investigated will be solute concentration and solvent identity, spraying flow rate, spraying distance and spraying time. The size of the deposited particles will be visually examined to determine if satellite droplets formed at the cone jet break-up are preferentially deposited at

the edges of the sprays. The effect on the MALDI ion signal for each variable will also be investigated.

## Experimental

### *Sample Preparation for the Angiotensin I/PEG 3400 and CHCA Systems*

A 0.02M solution of CHCA and 1.0 mg/mL solution of AngI or PEG 3400 were prepared in methanol (AngI) or THF (PEG 3400). The matrix and analytes were mixed at a M/A of 1300:1 for deposition.

### *Electrospray Deposition Conditions*

200uL of the MALDI sample solution were charged into the sample loop and needle. An insulating layer of tape was applied to the surface of a Bruker Daltonics Multiprobe™ sample plate, with a 6mm<sup>2</sup> area removed. Samples were sprayed from a height of 20mm at a flow rate of 2.0uL/min for 2 minutes for the AngI/CHCA system and at a height of 23mm and a flow rate of 4.0uL/min for 1 minute for the PEG 3400/CHCA system. The electric field was determined by the applied voltage (~5400V) and distance to the grounded sample substrate and held constant for each sample system. The measured current of the stable sprays were ~60nA for the AngI system and ~15nA for the PEG 3400 system. The insulating layer of tape was removed prior to MALDI TOFMS analysis using a Bruker Daltonics Autoflex III™ instrument equipped with a 355nm SmartBeam II™ Nd:YAG laser. Operating voltages and laser power for the instrument were held constant. The voltages were 20.0kV for IS1, 16.7kV for IS2, 21kV for the reflector, 7.8kV for the lens and 1.65kV on the micro-channel plate detector.

Individual peak areas were calculated using the centroid integration routine in the Bruker Daltonics FlexAnalysis™ software. Six accumulations of 500 shots taken at 100Hz were used to calculate the standard deviation of each spray (i.e, the intra-sample precision). Average

areas of the six accumulations for each spray from 4 independent sprays were used to calculate the inter-sample precision. Note that these precision values are for *absolute* signal intensity.

## Results and Discussion

### *Optimization of Spraying Conditions*

In order to explore the utility of the new controlled ESD method for sample preparation, experiments were conducted using conventional MALDI matrices with both peptide and polymer analytes. The controlled sample preparation should allow for higher precision of analyte signals via production of a spatially confined and homogeneous sampling surface. A solution of Ang I and CHCA was used to test this hypothesis. The sprayed samples were localized to the portion of the target that was not covered by the electrical tape, as was observed in the Csl experiments described in the introduction. These samples were then analyzed by MALDI-TOFMS. These samples showed good intra-sample precision ( $<6.0\%CV$ ) but poor inter-sample precision ( $\sim 17\%CV$ ).

In order to better visualize the sprays, the samples were sprayed again using the same solutions but for a longer period of time. The samples were sprayed for four minutes from 20mm at a flow rate of 2.0  $\mu\text{L}/\text{min}$ . As the spray time was increased a previously unnoticed effect was observed. The sprayed material was primarily deposited onto the uncovered surface of the target; however, it was also deposited on the sides of the metal target and onto the edges of the exposed metal surface of the current transducer located underneath. Any metal surface that was held at ground potential was attracting the charged material; therefore not all of the material being sprayed was being interrogated in the MALDI experiment. In order to eliminate this problem the outer edge of the probe was wrapped with several layers of electrical tape and the current transducer was covered with tape anywhere it was exposed outside of the footprint

of the MALDI target. Samples were again sprayed under identical spraying conditions and analyzed using MADLI-TOFMS. The precision of the samples dramatically improved, but still were not under 10% CV, which was the standard from our previous work<sup>2</sup>.

To better understand the reproducibility of the sprayed samples, studies were conducted by loading the spraying needle with the Ang I/CHCA solution for spraying at multiple time intervals. The time intervals chosen were 1, 2, and 4 minutes. A single spray was conducted for the defined spraying time, then a new sample plate was placed into the apparatus and the process was repeated without reloading the sample solution into the needle. Figure 4.2 shows the results of the 1 minute spray time experiment.

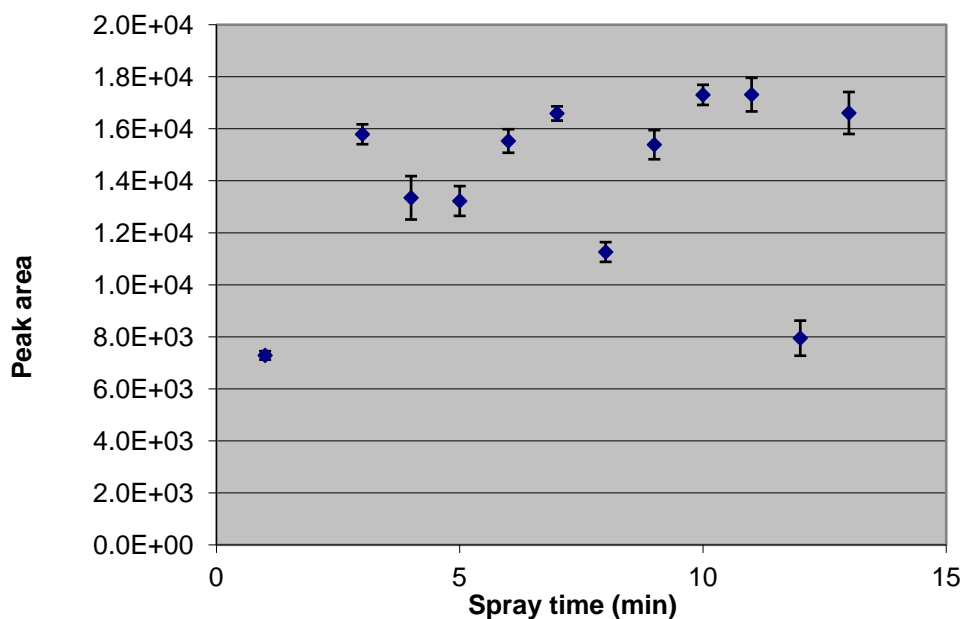


**Figure 4.2:** Plot of average peak area of Angiotensin I as a function of repeat spraying. Angiotensin I in 0.02M CHCA at M/A of ~1300:1 was sprayed for 1 minute intervals. The data points represent the average of 5 independent 500 shot accumulations for each time point. The sample needle was not reloaded between sprays for this study.

Of note in Figure 4.2 is that there appears to be an inconsistency in the average peak area for the analyte. The data demonstrate 1 minute sprays created without re-loading the sampling needle will produce samples that exhibit high intra-sample precision, but the peak area is highly variable between sprays. Also of note in this data is the first time point at one minute. It is the lowest point in the plot. Results obtained from two minute sprays are presented in Figure 4.3 and show a similar trend to the one minute spray data at spray times less than 10 minutes.

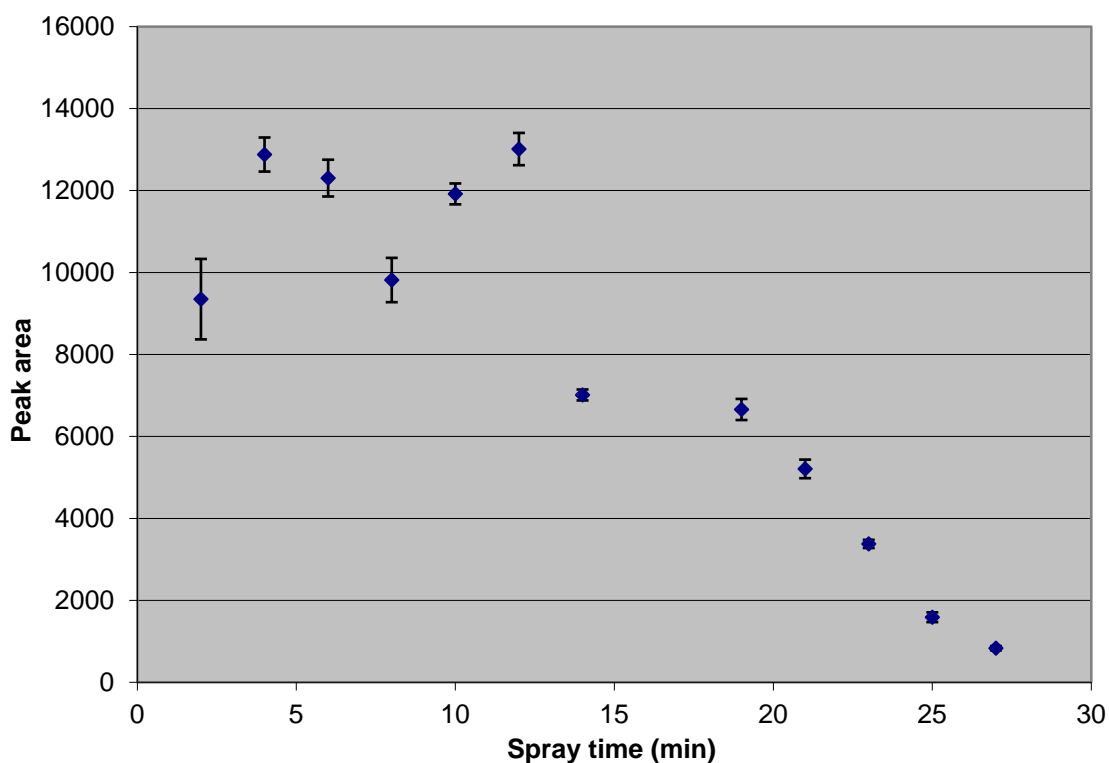


**Figure 4.3: Plot of average peak area of Angiotensin I as a function of repeat spraying. Angiotensin I in 0.02M CHCA at M/A of ~1300:1 was sprayed for 2 minute intervals. The data points represent the average of 5 independent 500 shot accumulations for each time point. The sample needle was not reloaded between sprays for this study.**

The two minute sprays were carried out for the same number of cycles, resulting in a longer overall spray time. Note that as more of the sample was consumed in this experiment, at



later time points the analyte peak area begins to decrease in a linear fashion. This is likely due to the mixing of the backing solvent from the syringe pump with the sample and consequent dilution of the sample mixture. Again it is interesting to note that the first time point in the graph has a low signal and larger variability as compared to the other time points. These data show that there will be a limit to the length of time that one can spray a single sample before it becomes diluted and signal is lost. There also appears to be a point between 4 minutes and 12 minutes where the samples generate similar instrument response. Figure 4.4 demonstrates that 4 minute sprays must be sprayed from separate loadings of the sample solution into the apparatus. From the first spray of four minutes there is a linear decrease in the signal observed from the MALDI-TOF analysis.

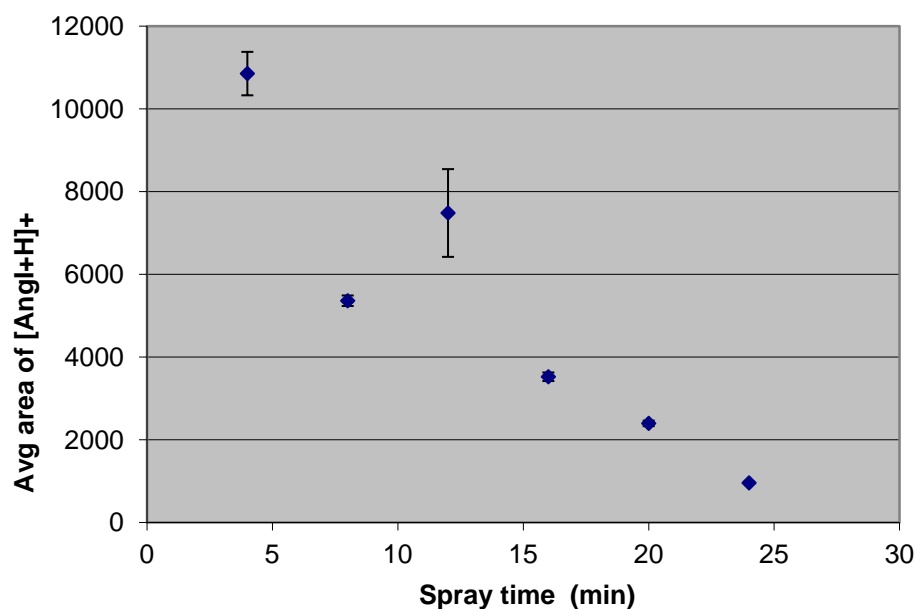


**Figure 4.4:** Plot of average peak area of Angiotensin I as a function of repeat spraying. Angiotensin I in 0.02M CHCA at M/A of ~1300:1 was sprayed for 4 minute intervals. The data points represent the average of 5 independent 500 shot accumulations for each time point. The sample needle was not reloaded between sprays for this study.

Conclusions drawn from these data shaped the sample preparation protocol going forward. The observations of the first spray from the 1 and 2 minute spray time studies consistently being lower in signal response lead to a modified sample loading process. Prior to each loading of the sample two 100uL volumes of backing solvent were passed through the loading valve tubing and sampling needle. Following this, two 100uL volumes of the sample solution are passed through the loading valve tubing and sampling needle. The second sample load was the solution that was used for spraying. Before the metal target was put in place ~10 $\mu$ L of the sample solution was passed through the needle. The syringe pump was then set to the desired flow rate and the voltage set to a voltage just below cone jet onset; when the droplet appeared to have a diameter equal to that of the spraying needle, the voltage was applied. The voltage was then increased to form a stable cone jet as verified by the current measurements on the oscilloscope. Upon adopting the new sample loading procedure highly precise and size controlled ESD MALDI-TOF samples were prepared. The results for both a common peptide (Ang I) and a synthetic polymer sample (PEG 3400) are found in Table 4.2.

**Table 4.2: Analysis of 4 independent sprays of Angiotensin I and PEG 3400. Each spray is an average of 5 mass spectra of 500 accumulations**

Angiotensin I and CHCA Intra-Sample Precision		PEG 3400 and CHCA Intra-Sample Precision	
Spray #	%CV	Spray #	%CV
Spray 1	3.1	Spray 1	1.5
Spray 2	3.5	Spray 2	3.6
Spray 3	2.0	Spray 3	2.6
Spray 4	2.9	Spray 4	5.4
Inter-Sample Precision		Inter-Sample Precision	
4.1		7.1	

Table 4.2 demonstrates that this new sample preparation technique can be used to produce highly reproducible MALDI samples. Note that the intra- and inter-sample precision (expressed as %CV) of the samples presented are not corrected using an internal standard; the %CV values were calculated using the raw peak areas of each analyte alone. The proper control of the spraying apparatus by complete insulation of metal surfaces around the sampling probe and proper sample spraying technique leads to the production of homogeneous samples that are easily identified in the mass spectrometer.

### ***Characterization of the Controlled Electrospraying Technique***

In Chapter 3 efforts were made to understand the contributions of flow rate, spraying distance and electric field on the diameter of the resulting sprayed sample spots. These studies focused on the morphology of the sprayed particles and total area of the spray. They did not define the MALDI performance of the variables studied. With the controlled spraying technique the sprayed area can be removed as a variable. Still there is a desire to understand the morphology of the sprayed material and its consequences on the MALDI signal generated from

the resulting sprays. The following section will be divided into the MALDI performance of samples sprayed at varying spray heights and at varying spraying times. Attention will be paid to the total signal generated as well as to determining the apparent thickness of the samples sprayed. AFM and SEM images of representative sprays will be presented as a qualitative explanation for the observed MALDI signals.

The controlled spray samples were first characterized using AFM and SEM imaging. These techniques were used to show that the controlled spraying samples were morphologically similar to those produced using the uncontrolled ESD methods in our lab. The AFM image of a 2 minute spray of 0.02M CHCA in MeOH is shown in Figure 4.5. The image is visually similar to the AFM images of the uncontrolled ESD samples presented in Chapter 3. Figure 4.6 is a collection of SEM images acquired from samples sprayed in both a controlled and uncontrolled ESD experiment.

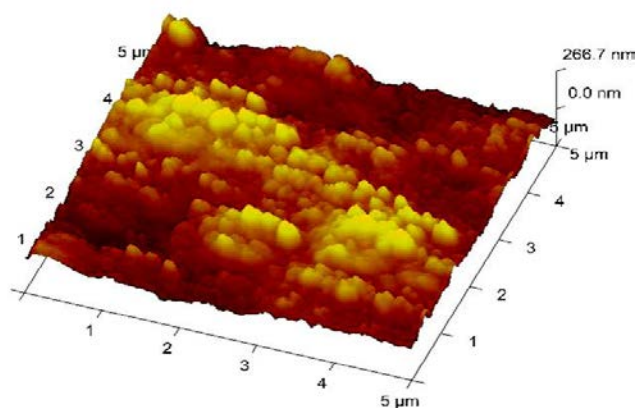


**Figure 4.5:** AFM image of a solution of 0.02M CHCA in MeOH sprayed from a height of 20mm and 2.0ul/min for 2 minutes using the controlled electro spray deposition technique.

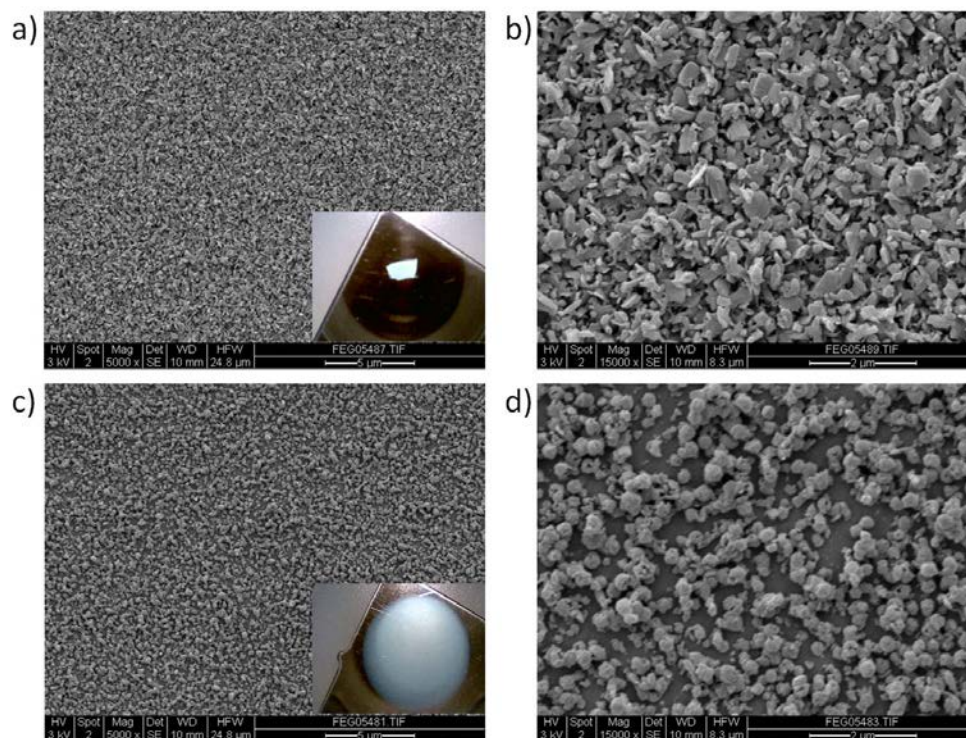


**Figure 4.6: SEM images of controlled and uncontrolled electro spray deposition of 0.02M CHCA in MeOH sprayed from a height of 20mm at 2.0uL/min for 2 minutes. a) Controlled ESD at 5k magnification, b) Controlled ESD at 15k magnification, c) Uncontrolled ESD at 5k magnification, d) Uncontrolled ESD at 15k magnification. The inset micrographs in a) and c) are to demonstrate the gross differences in the size and shape of the resulting sprayed material using each ESD method.**

The SEM images in Figure 4.6 show some gross differences between the two spraying methods. For the uncontrolled ESD method it is evident that there is incomplete coverage of the sprayed surface, as the bare metal of the sample plate surface can be clearly seen in the 15Kx magnification image. The density of the material deposited in the controlled spray is higher than that of the traditional method. Also of note is the appearance of crystallites in the image of the controlled electro sprayed sample. This is possibly due to slower drying of the particles in the controlled sample. The evaporation of the solvent may be decreased for these samples as the density of the droplets near the surface is likely higher. The increased density will affect the local partial pressure of the solvent near the surface and may promote slower drying and thus the formation of crystallites. The formation of crystalline structures from drying droplets has been

shown in the literature<sup>9</sup> and will be further discussed in Chapter 6. As will be discussed later in this chapter, one must consider the spraying time, concentration of matrix and spraying distance when using the controlled ESD method in order to maintain homogeneous deposition of amorphous particles on the surface. The insets in Figure 4.6 show the dramatic decrease in the macroscopic sample size using the controlled ESD method. The controlled ESD sample spot is ~95% smaller than the spot created using the traditional ESD method under the same spraying conditions.

Previous work in our group has examined the sample surface of the uncontrolled ESD technique using microscopy. The findings revealed that if a sufficiently thick layer(s) of sample is sprayed onto a metal surface that the material forms a fairly flat surface with a thickness on the order of 1 -2  $\mu\text{m}^1$ . Confocal laser microscopy was used to determine if the controlled ESD samples also exhibit the same flat sample surface when sprayed onto a metal surface. The images of a controlled ESD sample are found in Figure 4.7.

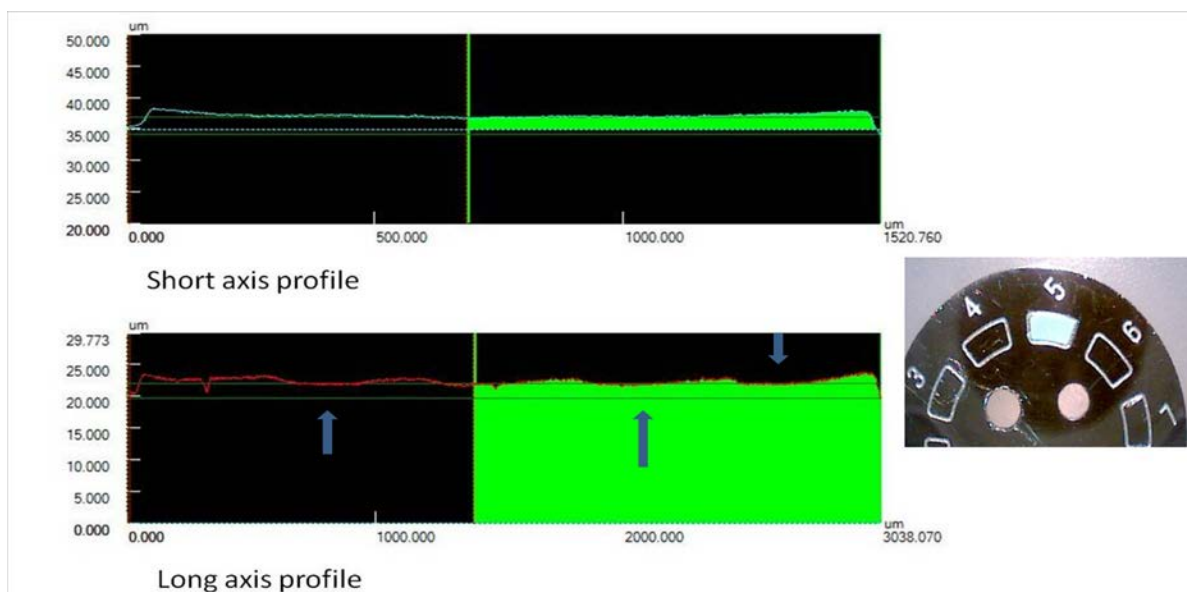


**Figure 4.7:** Laser confocal micrographs of a controlled electro sprayed sample contained to an area of 1.5mm x 3mm. The Solution sprayed was 0.02M CHCA in MeOH at a flow rate of 2.0uL/min for 2.0 minutes from a height of 20mm. The sample also contained Angiotensin I in a M/A ratio of ~1300:1. The blue arrows in the long axis profile image show surface defects that are from laser sampling of the spot in a MALDI-TOF instrument.

The inset photograph in Figure 4.7 shows the controlled ESD sample confined to the 1.5 x 3mm sample location labeled number 5. The cross-section of the sample spot was collected from both axial directions using confocal laser microscopy. Note that there is a slight concaveness to the surface of the sprayed sample. The thickness of the sample remains fairly constant at approximately 2.5  $\mu\text{m}$  across the entire sample surface. An expansion of the data collected at the edge of the deposited sample is shown in Figure 4.8. The analysis of the edge of the sample shows that there is a steep increase in sample thickness over a span of 20 $\mu\text{m}$  from the surface of the metal plate to the plateau of the sample. A decrease in the sample coverage can also be seen near the edge of the sample. This is not unexpected and will be further demonstrated and discussed later in this chapter.

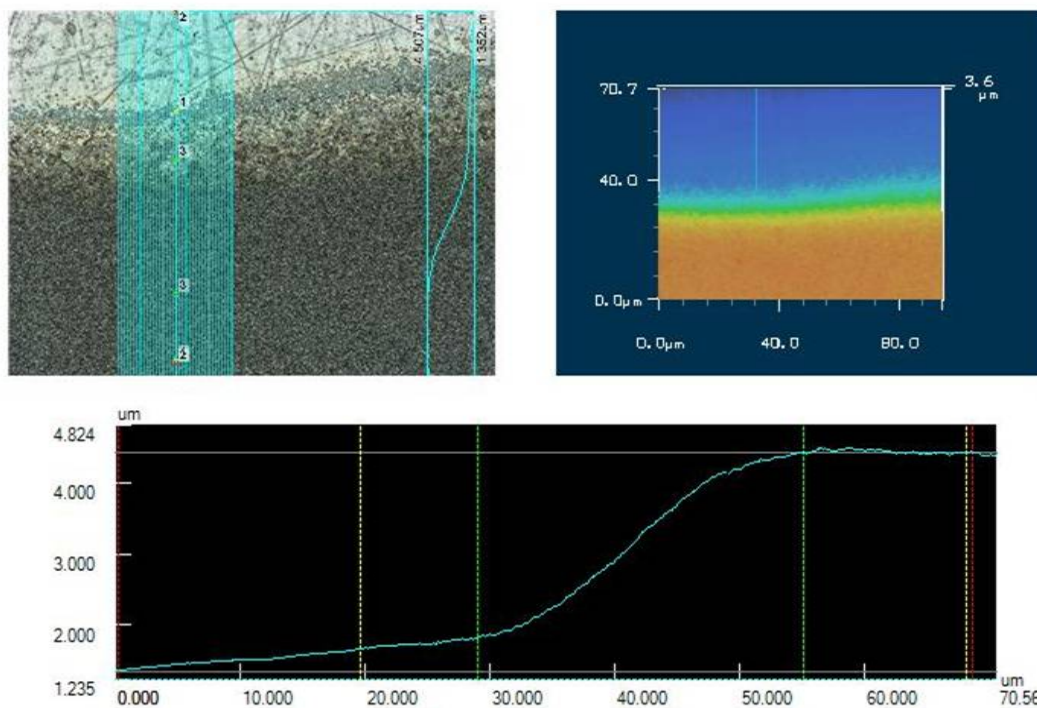


**Figure 4.8:** Laser confocal micrographs analyzing the edge of a controlled spot sample. The images show a steep rise of the sample edge to a height of  $\sim 3\mu\text{m}$  from the metal surface over a distance of  $\sim 20\mu\text{m}$ .

The micrographs presented in Figures 27 and 28 demonstrate that the controlled ESD technique produces samples that are similar morphologically to those produced using the traditional ESD technique for sample preparation. Further investigations using the controlled ESD technique will focus on the MALDI-TOFMS behavior of the samples. As in Chapter 3, spraying height, flow rate, spraying time and matrix concentration will be investigated using the new spraying technique. SEM images are provided for key samples to aid in rationalizing the mass spectrometric behavior observed in each of the experiments.

### ***Matrix Identity and Concentration Effects on Controlled ESD***

Chapter 3 introduced the concept that matrix and solvent identity may be a factor in ESD sample preparation. AFM images of 2,5-DHB deposited from various solvents visually



demonstrated that particle morphology may be influenced by the nature of the solvent used for spraying. This effect is not unprecedented and has been noted by other research groups<sup>10-13</sup>. The physio-chemical properties of the solutions being sprayed are also influenced by the concentration of the matrix in the mixture. These properties are not easily measured on small volumes, therefore only the identity and concentration of the matrix in a solution of methanol will be considered herein. The reason for this is that there are a finite number of preferred MALDI matrices as described in the literature<sup>14, 15</sup>. Two of the most commonly used MALDI matrix compounds are CHCA and 2,5-DHB, therefore these two matrices were examined under the normal operating conditions for the controlled ESD technique at a concentration of 0.02M in MeOH. The two solutions containing these matrices were sprayed for 30 seconds and two minutes. The 30 second spray was chosen as a way to investigate individual particles on the surface of the target, as it was expected that a spray of this duration would not result in complete surface coverage. The two minute sprays were made to image the surface of a sample that would be examined by MALDI-TOFMS, to determine if the layering of material on the metal surface produced morphological differences. SEM images of these samples are shown in Figure 4.9.

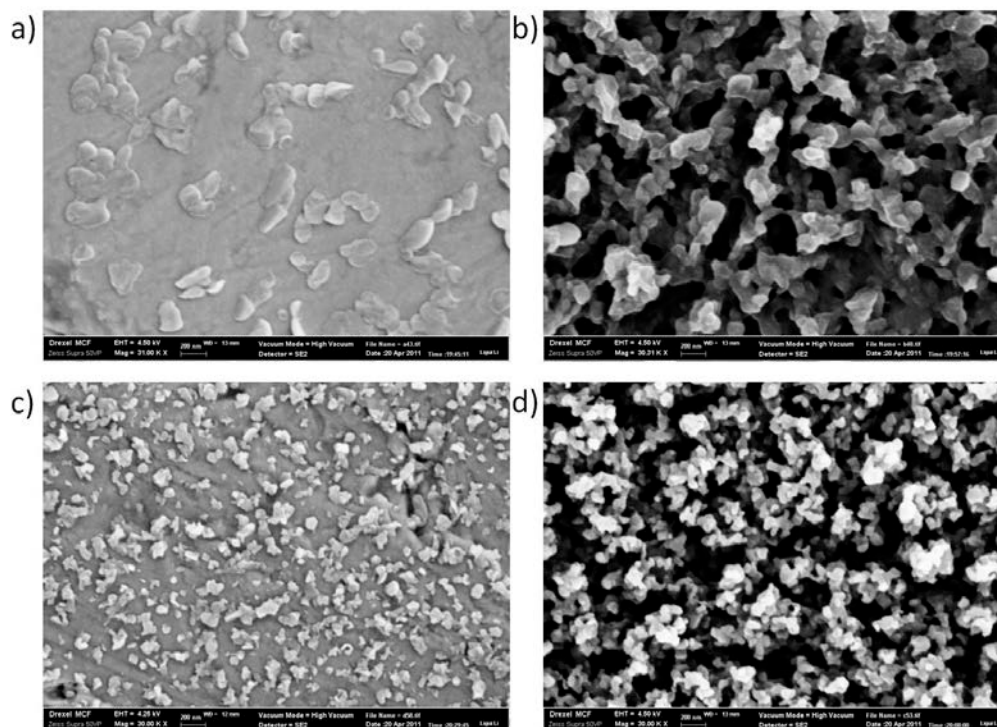


**Figure 4.9:** SEM images of 0.02M sprays of 2,5-DHB and CHCA in MeOH. Samples were sprayed from a height of 20mm and a flow rate of 2.0 $\mu$ L/min. a) 2,5-DHB sprayed for 30 seconds, b) 2,5-DHB sprayed for 2.0 minutes, c) CHCA sprayed for 30 seconds, d) CHCA sprayed for 2.0 minutes. Images are magnified 30k X.

The samples sprayed using 2,5-DHB (Figures 29a and b) appear to be deposited wetter than those prepared using the same concentration of CHCA in MeOH. In the images of the 30 second sprays, the material deposited from the CHCA spray (Figure 29c) appears to have impacted the surface dry and represents a typical amorphous particle that is formed when using the ESD sample preparation technique. This observation should not be unexpected as the solubility of 2,5-DHB is  $\sim 4x$  greater in MeOH than that of CHCA. Solubility data are presented and discussed further in Table 6.1 in Chapter 6. The 2,5-DHB spray at 30 seconds (Figure 29a) seems to deposit still wet droplets of matrix and MeOH that then dry on the surface of the metal target. This morphological trend is carried throughout the spraying process as can be seen in the SEM images of the two minute sprays for each matrix. The two minute spray of the 2,5-

DHB solution (Figure 29b) is spongy in nature, while the CHCA spray (Figure 29d) forms piles of more solid amorphous particles in the surface. Of note for both matrix solutions is that the surface generated with longer spray time does not form a continuous homogeneous layer, but rather a high surface area network of randomly dispersed solid particles in a lattice like structure. CHCA was chosen for future controlled ESD experiments because it visually produced a drier particle on the surface.

The images in Figure 4.9 reinforce the idea that solubility of the matrix in the spraying solution is an important variable to consider when using ESD for sample preparation. To further investigate this phenomenon CHCA was again sprayed in MeOH, this time using varying concentrations of CHCA. The concentrations chosen represent 5, 10, 25, and 50% of the solubility limit of CHCA in MeOH. The images of these sprays can be found in Figure 4.10 below.

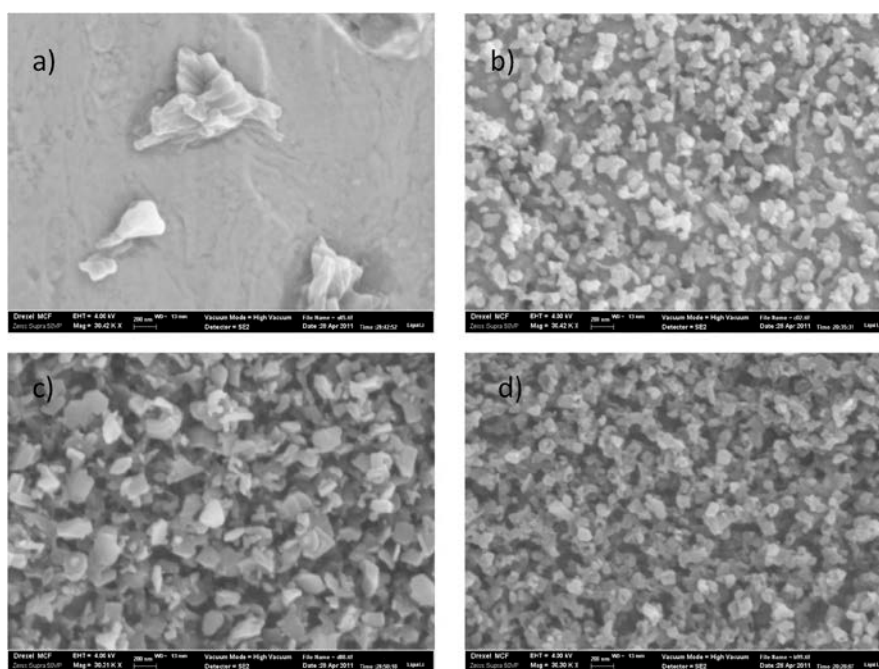


**Figure 4.10:** SEM images of CHCA sprayed for 30 seconds at a height of 20mm with a concentration in MeOH of a) 0.01M (5% saturation), b) 0.02M (10% saturation), c) 0.05M (25% saturation) and d) 0.1M (50% saturation). Images are magnified 30K X.

These thirty second sprays of the same matrix at different concentrations demonstrated two effects. The first is that at some concentration below the solubility limit of the matrix in a given solvent, the sprayed droplets are not dry prior to their impact with the surface. This is clearly shown in the SEM image of the 0.01M CHCA solution in MeOH in Figure 4.10a. The droplets that reach the surface are not dry upon impact and therefore form crystalline structures as they dry on the surface. Sprays of this type would not be ideal for MALDI-TOFMS analysis as the crystallization event could influence the distribution of analyte and matrix in each crystal and not provide a homogeneous sample for analysis. Secondly, as the concentration of the matrix is increased in the spraying solution, the amount of solid material deposited on the surface is increased for a given spray time. The density of dried particles covering the surface does increase for higher concentration of matrix in the solvent, as can be seen in the SEM images. This is important in that the “thickness” of a sprayed sample will increase with higher concentrations of matrix.

The increase in the particle density at higher matrix concentration can in part be explained by the increase in the amount of matrix molecules in the individual liquid droplets emitted from the tip of the Taylor cone. As the droplets travel through the air in the ESD chamber, the solvent contained in the droplet begins to evaporate. During the evaporation of the solvent there is no loss of charge in the droplet<sup>16</sup>. At a critical point, where the surface tension of the droplet can no longer overcome the columbic repulsions caused by the surface charging of the droplet, the droplet undergoes fission. Typically the material is released in a jet of small charged droplets<sup>17</sup>. Most common matrix compounds are polar in nature; CHCA is a strongly acidic compound. Charge build-up on the surface of the droplets is driven by the dissociation of the matrix molecules in the droplet<sup>18</sup>. Therefore, droplets formed with higher concentrations of matrix will build charge on the surface of the droplet at a greater rate

kinetically than droplets with a lower concentration of matrix. Higher initial concentrations of matrix may allow droplet fission to occur more frequently, thus producing more solid particles of smaller size on the metal surface of the probe during ESD sample preparation. This process is also aided by an increase in droplet surface area relative to internal volume. Smaller droplets will have a larger surface area and the charge build up on the surface will be more efficient. It should also be noted that the conductivity, viscosity and surface tension are different between the sprayed solutions in Figure 4.10. These properties will have an effect on the initial droplet volume and therefore affect the final droplet size<sup>10, 12, 19</sup>. These properties were not considered in this experiment because the dominating effect on the initial droplet size is the flow rate of the solution as can be seen in the following equation<sup>12</sup>:

$$d = a_d \left( \frac{\rho \epsilon_0 Q^4}{I^2} \right)^{\frac{1}{6}} \quad (1)$$

Where  $d$  is the droplet diameter,  $a_d$  is a proportionality constant,  $\rho$  is the viscosity of the solution,  $\epsilon_0$  is the permittivity of vacuum,  $Q$  is the flow rate, and  $I$  is the current measured emitted from the needle. Using this equation to predict initial droplet diameter and thereby droplet volume, the flow rate of the sample is found to have the largest effect on droplet size. Since the flow rate was held constant for these experiments, the differences in the initial droplet volumes would be due to the change in current generated at the counter electrode, which is an indirect measurement of the conductivity of the spraying solution<sup>16, 20</sup>. In Chapter 3 the effect of the concentration on the measured current for 0.01M and 0.1M CHCA solution was shown. The 0.1M CHCA solution generated a current roughly 6x that of the current generated by the 0.01M CHCA solution. This value suggests that at a maximum, if no other solution properties changed, the droplets generated from a 0.01M CHCA solution would start out approximately 36x larger

than droplets formed from a 0.1M CHCA solution. This seems to fit with the observation that the 0.01M solution produced wet droplets on the surface as compared to the smaller drier particles deposited by the 0.1M solution. It also helps to explain the increased number of particles on the surface for the more concentrated matrix solutions, as smaller initial droplets would lead to the appearance of more particles on the surface. However, the current alone cannot explain all of the SEM images. The particles deposited on the surface in Figure 4.10 for the 0.02M and 0.05M solutions do not scale as expected when compared to the 0.1M solution particles. The confounding variable is likely the solubility of the matrix in the MeOH solvent. Once the solubility limit is reached the droplet should form a "crust" or shell that would prevent it from further fissions prior to impact on the surface<sup>9,21</sup>. In order to further explore this concept, solutions of 0.02M CHCA in MeOH were sprayed at a flow rate of 2.0uL/min for 30 seconds at varying heights. The solution variables are kept the same, but the distance to the metal surface is increased, thus any differences in particle size should be attributable to the droplets spending different amounts of time travelling to the surface (and therefore different times drying). SEM images of samples prepared for this experiment are found in Figure 4.11.

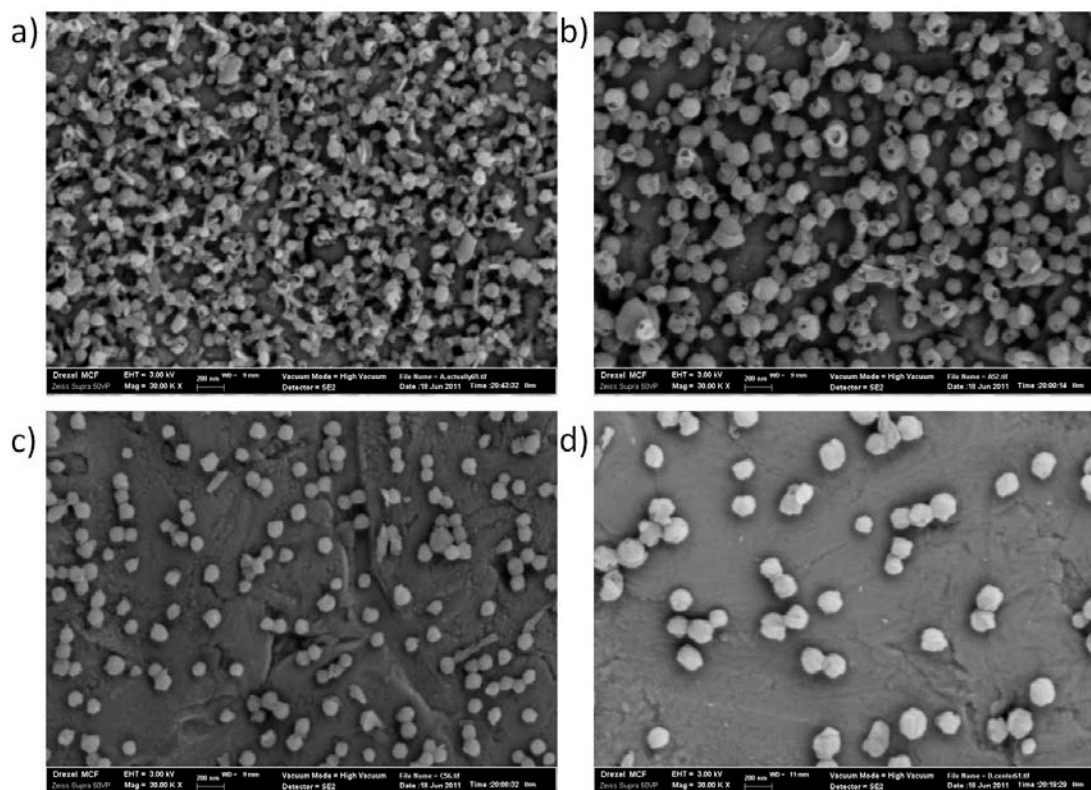


**Figure 4.11:** SEM images of 0.02M CHCA sprayed at a flow rate of 2.0 $\mu$ L/min for 30 seconds from heights of a) 15mm, b) 20mm, c) 25mm and d) 35mm. Images are magnified 30k X.

An interesting feature seen in Figure 4.11 is that for the sprays generated from heights of 15 and 20mm (Figure 4.11a and b) the particles appear to produce hollow spheres with holes as compared to the sprays generated from 25 and 35 mm (Figures 11c and d), which appear to produce solid spheres that lack the holes seen at smaller spray distances. Another observation is that the particles generated from the 25 and 35mm sprays are more homogeneous in size as compared to those produced at the shorter spraying distances. A possible explanation for these observations can be found in the velocities of the charged particles as they approach the surface. Rietveld et al. presented an equation for the velocity of a charged particle in the electro spray process as follows<sup>12</sup>:

$$v = \frac{Eq}{3\pi\mu d} \quad (2)$$

Where  $v$  is the velocity of the charged particle,  $E$  is the electric field,  $q$  is the charge of the droplet,  $\mu$  is the dynamic viscosity of the medium (air), and  $d$  is the diameter of the charged droplet. Again in Chapter 3 it was shown that under the same spraying conditions the electric field decreases as the height of the spray is increased. This would imply that the droplets sprayed from higher above the metal surface should have a lower velocity and therefore a longer drying time before reaching the surface. This could lead to the visually more homogeneous particle size distribution that is observed from the larger spraying distances. However, it does not explain the presence of the “holes” in the particles that are deposited when using 15 and 20 mm spraying distances.

Air dried droplets are known to form hollow shell particles<sup>21</sup>. The solubility and identity of the solute and the solvent in the droplet are critical to the thickness and rigidity of these hollow spheres<sup>9</sup>. It has also been demonstrated that if a solute has the tendency to form crystals, single crystal structures can be generated from the drying droplets<sup>22</sup>. Holes formed in the shells are also not uncommon. Figure 4.12 is an illustration of the types of particles that have been observed from air drying of droplets<sup>9</sup>.



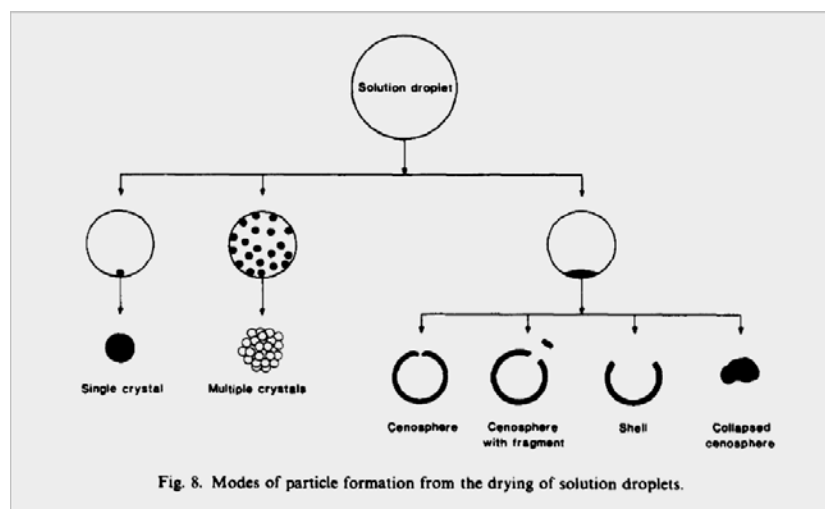


Figure 4.12: Illustration of the modes of particle formation of drying droplets. Reproduced from Leong<sup>9</sup>.

The illustrations on the left side of Figure 4.12 represent possible drying modes for materials that have defined crystal forming habits such as salts. Depending on the solubility and drying conditions a single crystal can be formed or a hollow shell of multiple crystals can be formed. The single crystal arises from low solute concentration and slow evaporation. The multiple crystal particle (2<sup>nd</sup> from the left) can be formed from high solute concentrations and rapid solvent evaporation. Multiple crystals are the result of multiple nucleation sites at the edge of the crystal where the concentration of solute is highest. On the right side of the image are the drying modes for organic molecules that do not exhibit crystal habits. The surfaces of these particles will exhibit crystals, but the shape of the crystal does not contribute significantly to the shape of the droplet. The surface shell is a result of a large number of crystallization sites but the shape of the deposited particle is still spherical and not dominated by the solutes crystal habit. These types of particles are similar to what we have observed in the SEM images from Figure 4.12. Depending on the drying rate, temperature, pressure, humidity, identity of the gas in the drying environment, solute concentration and solute solubility, any of the types of

particles illustrated in Figure 4.12 can be observed as a result of droplet drying<sup>9, 22, 23</sup>. More complete spheres are generated for solutions of lower solute concentration or solutes with high solubility in the droplet solvent. Intact hollow spheres are formed if the outer shell is permeable to the solvent vapor<sup>22</sup>. It is also important to note that gases have been observed trapped in the hollow spheres<sup>21</sup>. Although the presence of holes in the particles has been observed previously, it is not clear how they arise. They may form at or near the surface where contact with the metal drives the nucleation of the solute<sup>24</sup>. If this happens a concentration gradient toward the nucleation site can form in the droplet. This would lead to the buildup of the solute material at the bottom of the droplet allowing the solvent to evaporate faster at the top, possibly causing the hole at the top of the solid particle. The holes may also form from the fission of the charged droplets. Researchers have described this process as a jet of charged solvent being released from the parent droplet<sup>10, 11, 17</sup>. During this process the droplet is elongated as the charge tries to delocalize itself along the surface of the droplet. From the elongated droplet comes the emission of the charged solvent. This phenomenon has been demonstrated in Chapter 3 Figure 3.6 using high speed cameras<sup>10</sup>. The jet of material has a velocity and momentum away from the parent droplet and therefore by the conservation of energy the parent droplet should, for a period of time, be deformed inward on itself until the liquid can re-shape into a sphere. If this process was to occur at the critical solubility for the matrix in MeOH, it could explain the observation of the hollow particles observed on the surface for the sprays at shorter distance. Though the exact mechanism is not clear from this work, it seems that slower more gradual drying of the particles sprayed from 25 and 35mm leads to more homogeneous particle sizes on the surface.

Satellite droplets arise from the breakup of the liquid at the tip of the Taylor cone<sup>19, 25</sup>.

Previous work suggest that the satellite droplets will be approximately 2% of the parent droplet

volume and carry with them  $\sim 15\%$  of the total charge of the original droplet<sup>12</sup>. This implies that the charge density of the smaller droplets is quite large. The decreased mass and relatively high charge density would mean that due to Coulombic repulsion the satellite droplets should deviate farther from the central orthogonal axis of the spray. In order to see if this is experimentally observable, Figure 4.13 shows SEM images of samples prepared at the 35mm spraying distance that were collected at the relative center of the sprayed area and at the outer edge of the sprayed area.

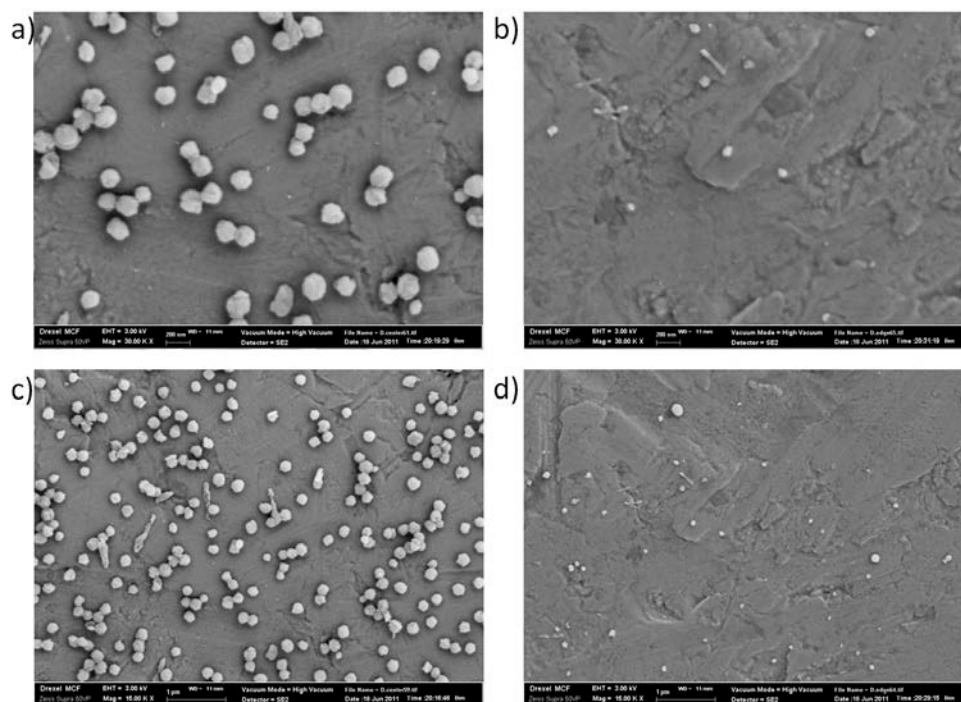


**Figure 4.13: SEM images of 0.02M CHCA sprayed at a flow rate of 2.0uL/min for 30 seconds and a height of 35mm. a) center of sprayed area at 30k X magnification, b) edge of sprayed area at 30k X magnification, c) center of sprayed area at 15k X magnification, d) edge of sprayed area at 15k X magnification.**

The outer edge of the sprayed material (Figure 4.13b and d) does contain droplets that are visually smaller than those observed near the center of the spray (Figure 4.13a and c). The density of these particles are also less than the density observed near the center of the spray.

This is expected and has been discussed in detail in other work<sup>10</sup>. While this visual observation is important for the precision of the spraying process, it still needs to be determined if the morphological differences of these samples impact the quality of the MALDI-TOFMS data. In order to determine this, samples of Ang I in CHCA matrix were sprayed from varying spray heights and analyzed by MALDI-TOFMS. Measurements of the average peak area are plotted as a function of spraying height as shown in Figure 4.14.

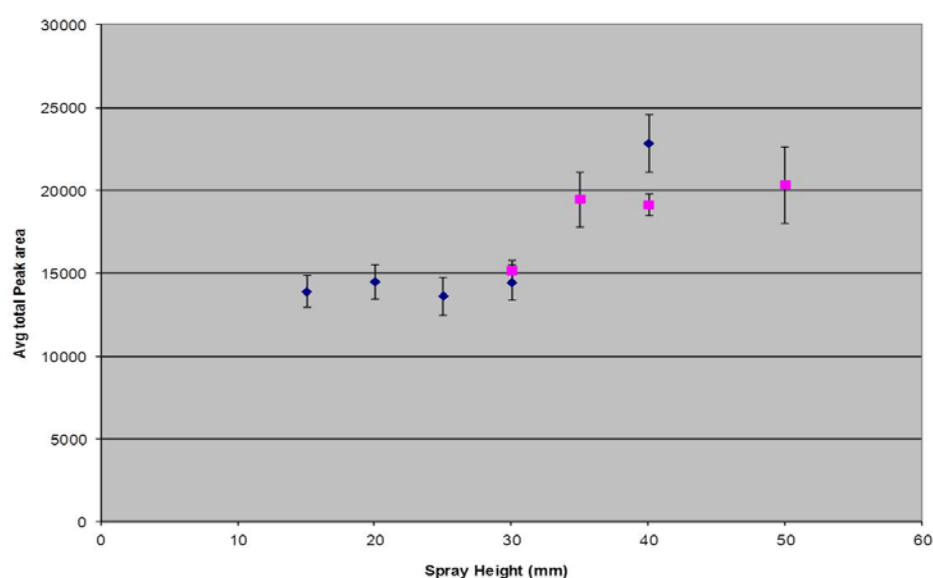


**Figure 4.14:** Graph of average peak area as a function of spray height for samples analyzed over two days. Each data point was sprayed from a solution of 0.02M CHCA at 2.0uL/min for 2 minutes. The blue diamonds are samples run on the first day. Pink squares were analyzed on a different day and include two repeated heights at 30 and 40mm. Each data point is the average of three independent sprays from each height.

The data obtained from the spraying height study indicate that there is an increase in signal as the spraying distance is increased for a solution of the same composition. In Figure 4.14, there are two distinct plateaus in the data. The first plateau exists in the height range of 15-30mm and the second in the height range of 35-50mm. Of interest is the total increase in signal between these plateaus; the second plateau represents an approximate 30% increase in

signal. Thus spraying from a greater distance yields a sample that is more sensitive in the MALDI experiment. One explanation for this increase in signal at a constant laser power in the instrument was given by Westman et al.; their group has shown that thicker samples will yield more ions<sup>26</sup>. To determine if the samples sprayed at varying heights were of different thickness we have employed a method for determining relative sample thickness in MALDI that has been previously reported by our group<sup>1</sup>. To do this, sprays from heights between 15 and 40mm were analyzed. The thickness of a sample should be indicated by the cumulative number of laser shots required to generate a plateau in ion signal. To accomplish this, a sample is analyzed by firing the laser at a fixed location of the sample. The molecular ion signal is summed over each accumulation and carried out until a plateau has been reached. In this way the relative thickness of the sample can be defined for each spray. The final summed areas for the Ang I molecular ion are given for each spraying height in Figure 4.15.

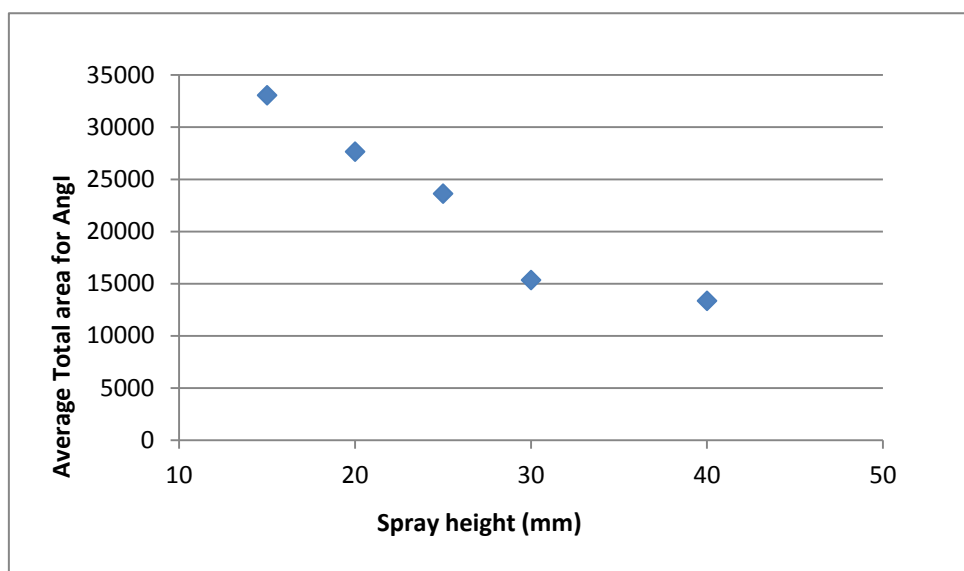


**Figure 4.15:** Total summed areas of the Angiotensin I molecular ion for sprays made from 0.02M CHCA and Angiotensin I (M/A ~1300:1) at 2.0uL/min for 2 minutes from varying spraying heights.

From the data acquired it appears that the samples sprayed at greater distances are not thicker than those sprayed from shorter distances. Therefore there must be another reason for the increased signal and sensitivity when spraying at greater distances. The particle morphology may play a role in the amount of material desorbed on each laser shot. The sprays made from larger spraying distances appear to be solid particles on the surface as compared to the cracked hollow particles that are observed for sprays made from shorter distances (Figure 4.11). A closer look at the initial 500 laser shots for each of the samples shows an increase in the total area per shot for the 40mm spraying distance followed by the onset of an early plateau as compared to the samples sprayed at shorter distances.

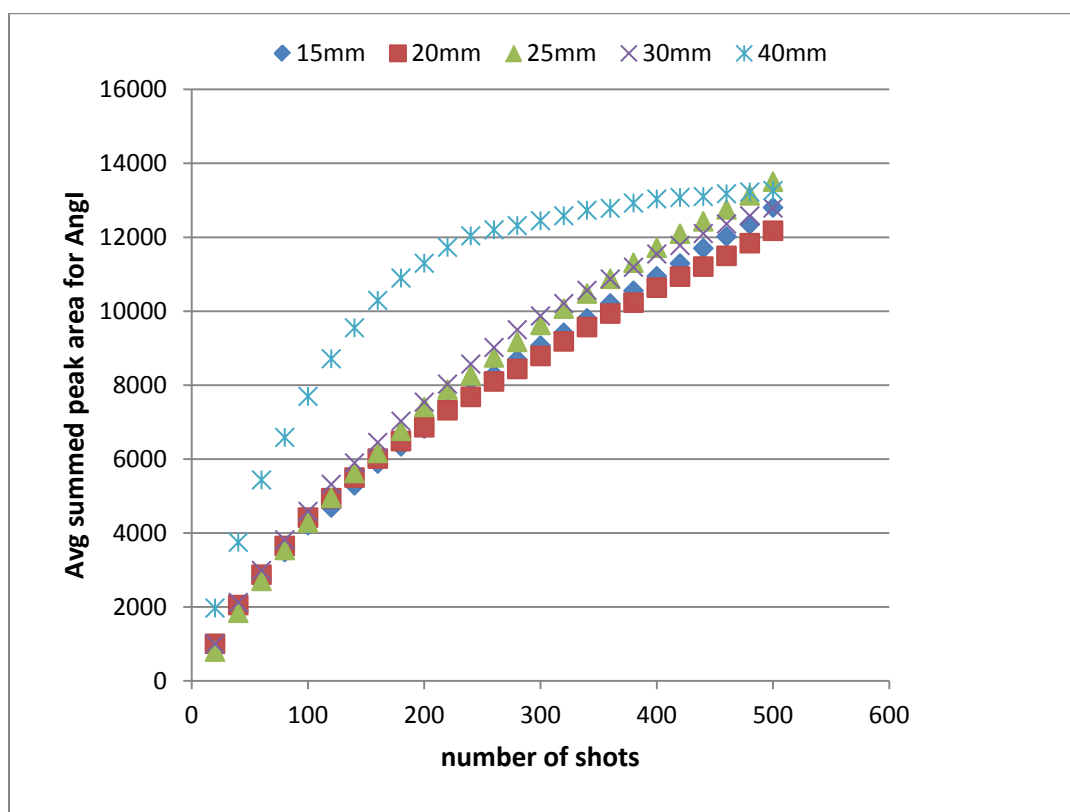


Figure 4.16: Average summed areas of the first 500 laser shots of sprayed solutions of 0.02M CHCA and Angiotensin I (M/A ~1300:1) sprayed at 2.0 $\mu$ L/min for 2 minutes from varying heights.

Figure 4.16 shows that persistence of the ion signal for the lower spray heights is greater as compared to the 40mm spray. However, it also shows that the initial ion intensity per shot is greater than that for the shorter spraying distances. This graph confirms that the sample sprayed from 40mm gives greater sensitivity than those sprayed from shorter distances for the first 100 shots or so of the sample, thus corroborating the observations in Figure 4.14 and Figure 4.15. The increase in the average area of the larger spraying distance is caused by either larger amounts of material being desorbed per laser shot or higher ionization efficiencies for the 40mm spray.

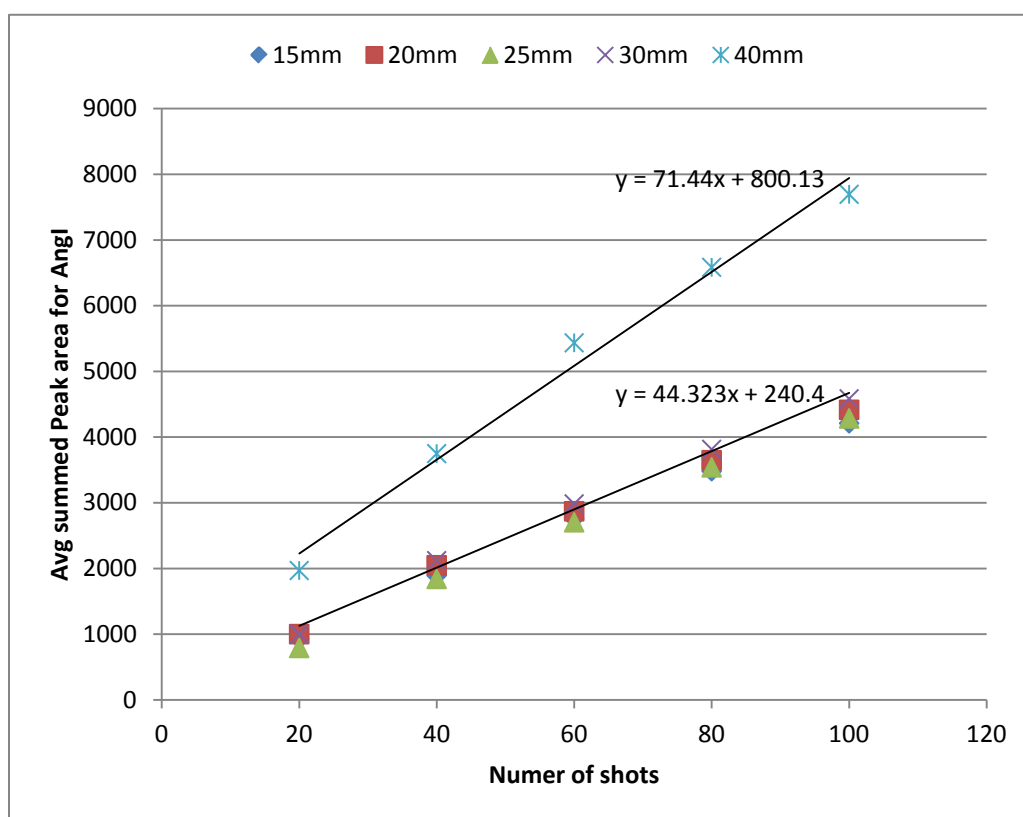
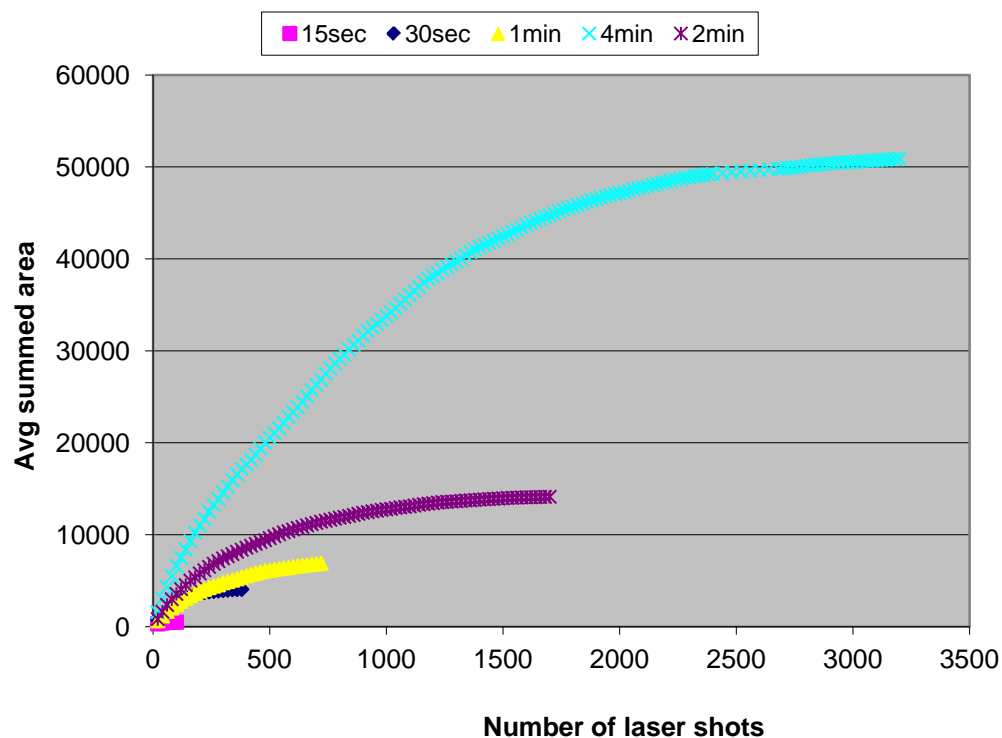


Figure 4.17: Averaged peak areas per shot for the first 100 shots of solutions of 0.02M CHCA and Angiotensin I (M/A ~1300:1) sprayed at 2.0uL/min for 2 minutes from varying spray heights. The fitted lines were generated by excel as the best fit linear regression for the data points. The equations are presented here for comparisons only, and are not meant to be a quantitative model for desorption or ionization. Note that this graph is an expansion of the graph presented in Figure 16.

To further investigate the observed signal differences, the average peak area collected from the first 100 shots for each sample were plotted and the initial slopes for the area plots were calculated. The slopes in Figure 4.17 are included for comparison purposes; the slope for the 40mm spray is approximately 60% greater than that for the shorter spraying distances. This represents a rather large quantitative difference in the MALDI sensitivity for the 40mm sample, but does not support the hypothesis that the larger spraying distance produces samples of greater thickness. Therefore, there must be other factors affecting the signal in the MALDI experiment. To further re-enforce this point, samples were sprayed for varying lengths of time from a fixed distance. Longer spraying time will increase the amount of sample sprayed onto the surface of the probe and thereby increase the thickness of the sample. It is expected that the total summed signal for increasing spray time will increase, and that this increase should be linear with time. The samples for this study were prepared using the same sample solution as the height studies, but were sprayed from a constant distance of 20mm. The initial slopes of the ion intensities for at least the first 100 shots should be similar to that for the 20mm spraying distance as seen in Figure 4.17.





**Figure 4.18:** Average summed peak areas for Angiotensin I molecular ion as a function of number of laser shots in a fixed location on the sample. The samples were sprayed from a solution of 0.02M CHCA and Angiotensin I (M/A ~1300:1) at 2.0 $\mu$ L/min at a height of 20mm.

Figure 4.18 shows that the total signal generated from the samples does increase as a function of spraying time. As noted above, this result was expected as similar results using synthetic polymer samples has been reported by our group<sup>1</sup>. What is of more interest is that when the data are plotted in the same manner as the height data from Figure 4.17, an unexpected trend is found.

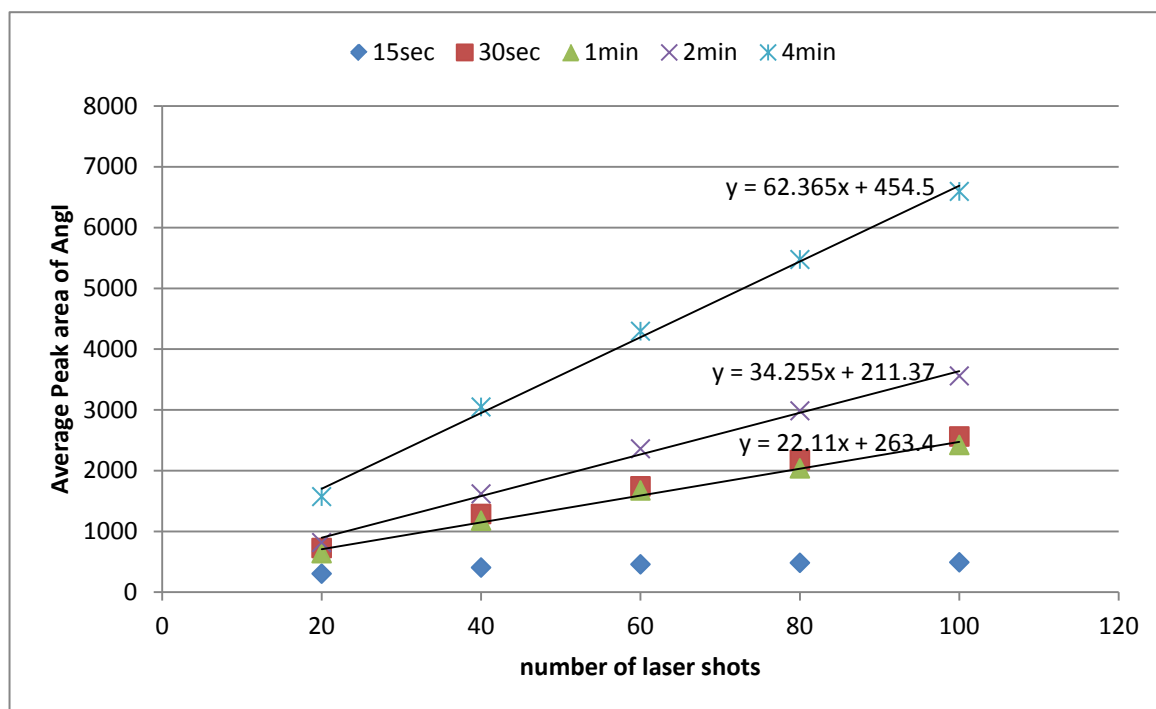
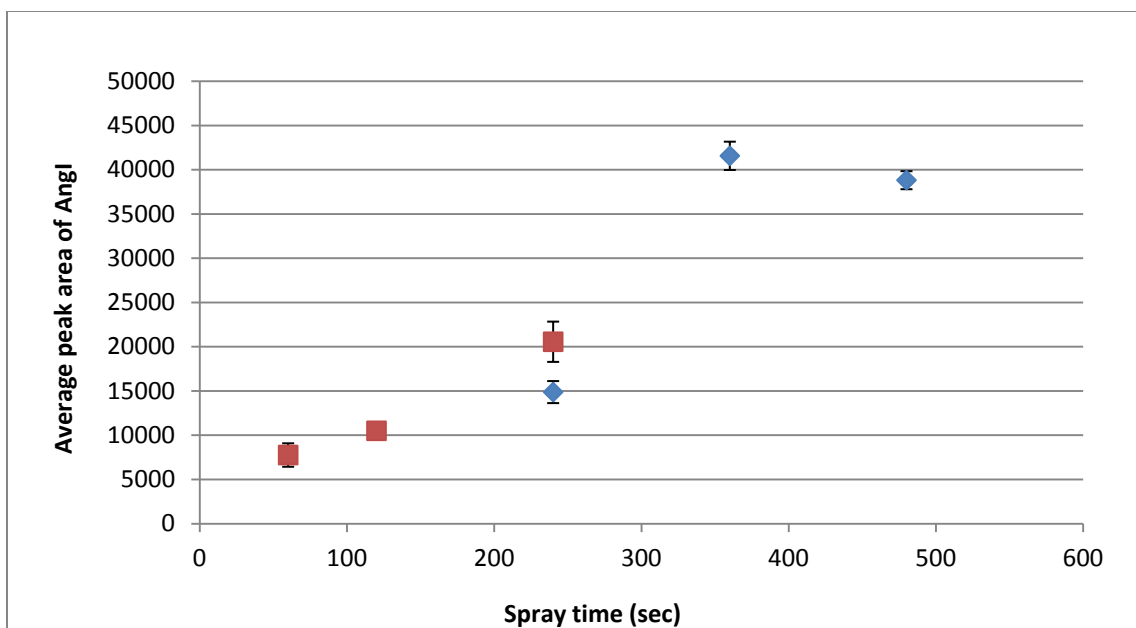


Figure 4.19: Graph of the average peak area for Angiotensin I molecular ion as a function of the number of shots for the first 100 shots on a clean sample. The samples sprayed were 0.02M CHCA and Angiotensin I (M/A ~1300:1) sprayed at 2.0uL/min from a height of 20mm.

The data for the first 100 laser shots for each of the samples are expanded in Figure 4.19. The slopes of the linear fits for the data points are again presented for comparison. It should be noted that the slope calculated for the two minute spray is similar to that which was obtained for two minute sprays between the spraying heights of 15 and 30mm, as presented in Figure 4.17. Also of note is that the slopes for sprays made between 30 seconds and two minutes are very similar, while four minute spray deviates significantly. The increase in slope with increasing spray time suggests that there is an increase in MALDI signal per laser shot for these samples. Therefore, the change in the total summed areas for the differing spray times are not linear as expected; there is an added benefit to spraying for longer periods that is not captured solely by the analysis of the thickness of the MALDI sample.

This phenomenon has to the authors knowledge not been noted or discussed in the literature previously for MALDI samples prepared by electrospray deposition. However, researchers have generated data using other preparation techniques and observed similar results<sup>26</sup>. In that study the traditional dried drop sample preparation was used and the ion signal as a function of laser penetration depth and energy deposition was explored. While their findings are not directly related to this work, the discussion presented could help to explain the results observed herein. They discuss the importance of the desorption volume on the plume density. Larger amounts of material desorbed from the sample surface will generate higher plume densities<sup>26, 27</sup>. A higher plume density provides more collisions between the excited state matrix molecules and the analytes, which facilitates the protonation process, creating the molecular ions of the analyte<sup>28-30</sup>. Westman et al. further discuss the effect of crystal size on the desorption process, describing that smaller crystals will be preferentially desorbed first and that different size crystals will create plume volumes with different energy densities<sup>26</sup>. Though our samples do not contain crystals for desorption, it has been shown that depending on the spraying variables the degree of particle heterogeneity can be influenced (Figure 4.9, Figure 4.10, Figure 4.11). The apparent uniform solid particles seen in the SEM images in Figure 4.11 could account for the greater sensitivity at higher spraying distances. The increased homogeneity of the particles leads to larger amounts of material being desorbed creating a higher plume density that generates stronger ion signals in the MALDI experiment. This process would also help to explain why the initial signal per shot is higher for the 40mm sprayed sample, but it appears to be depleted faster than the samples sprayed from shorter distances. This concept, however, does not explain the observations from the spraying time studies, as the particle size and distribution should remain the same during the spray.

The amorphous nature of the ESD prepared samples also may be the cause of the increased signal and sensitivity observed with longer spraying times. Previous attempts in our group to measure the thickness of the ESD samples proved to be difficult with traditional interferometry based methods<sup>1</sup>. This difficulty was eventually attributed to the high degree of scattering of the incidence light that decreased the amount of light returning to the detector. We have also shown that sprays of at least two minutes produce lattice-like structures of amorphous particles (Figure 4.9). The scattering of the incident light by these structures should increase as the layers of particles increase during the electrospray process. This increase in scattering could account for an increase in light/matrix interactions and thereby increase the volume of material being ablated per shot. As before, this increase in ablated material will increase the plume density and the secondary ion-molecule interactions leading to large analyte ion signals. An increase in desorption and ionization coupled with the increased thickness of the sample would explain the deviation from linearity seen in the spraying time studies. To determine if the effect observed would continue for longer sprays, a second study was performed over longer spraying times of up to 8 minutes.



**Figure 4.20:** Average peak areas for Angiotensin I molecular ion as a function of spraying time. Samples were prepared on two days from separate solutions of 0.02M CHCA and Angiotensin I (M/A ~1300:1) at a flow rate of 2.0 $\mu$ L/min and a height of 20mm. The data points represent the averages of three independently prepared samples for each spraying height.

The data in Figure 4.20, though limited, suggest that a plateau in the average analyte signal is observed when spraying for longer periods of time. This fits well with the idea that the scattering and interaction of the incident light in the MALDI experiment is increased as sample thickness is increased. At some finite thickness the energy absorbed for a sample should reach a maximum. At this point the effective amount of sprayed material that can be removed by the amount of energy deposited by the laser over the area of incidence (fluence) is maximized. This relationship has been described in previous work,<sup>31</sup> and a general equation has been given for the number of layers of a light absorbing material desorbed at a fluence above that which is needed to produce ions. For our experiments the layers are represented by the particles deposited on the surface as a result of the ESD process. After a sufficient number of particles have been deposited onto the surface, the metal probe is covered in a layer that obscures the surface toward other deposited particles. When this occurs new particles being deposited begin

to pile up on the surface. This leads to the buildup of particles on the surface resulting in the thickness of the sample on the plate as shown in Figure 4.8. It has been shown that multiple laser shots are required to desorb ESD samples to the point that the metal probe can be seen. Each laser shot will remove a finite amount of the surface<sup>27</sup>. Here we liken the removal of these particles to the layers of ejected material in equation 3.

$$l_{ejected} = \frac{1}{\alpha} \ln \left( \frac{F_{laser}}{F_{Thre}} \right) \quad (3)$$

In the above equation  $l_{ejected}$  is the number of layers of material ejected,  $\alpha$  is the effective absorption coefficient, and  $F_{laser}$  and  $F_{Thre}$  represent the fluence used and the threshold fluence required for the desorption of material (typically the fluence needed to generate ions in MALDI), respectively<sup>31</sup>. The laser power was held constant for all measurements conducted for the spraying time samples. If the effective absorption of the samples is changing as is argued above, this would explain the higher signals seen in the MALDI experiment. However, this is an oversimplification of the data in order to draw experimental conclusions. It is likely that while this may be one of the factors affecting the data, there may still be other yet unknown factors that need to be investigated in additional studies.

## Conclusions

The new controlled ESD sample preparation technique described in this chapter is shown to produce samples contained to a defined area that generate high intra- and inter-sample reproducibility. The MALDI signal dependence was shown to depend on the spraying distance and spraying time. While the exact mechanisms underlying the increased signal sensitivity in the MALDI experiment due to spraying height and spraying time have not been conclusively shown, their effects are still quantifiable and offer advantages over other sample

preparation techniques. Sensitivity in any analytical method is important to detect low concentration analytes. Using the information presented in this chapter one can increase the sensitivity of the MALDI experiment and possibly lower the detection limit for analytes of interest. Secondly, the ability to spray for longer times will deposit more sample onto the sampling probe. This alone will increase the likelihood of detecting low concentration analytes as compared to the traditional dried drop method. The dried drop method typically deposits 0.5-5 $\mu$ L of analyte and matrix solution onto a probe, where the same solution can be sprayed for many minutes in ESD sample preparations. There will be more analyte on the surface in a defined location using controlled ESD and therefore a larger analyte signal can be obtained using MALDI-TOFMS. This coupled with the observed sensitivity increase for analytes sprayed for longer time periods could allow very dilute solutions of analyte to be analyzed by the technique. Further studies should be conducted to quantify the extent of the signal enhancement for dilute analytes.

## References

1. Szyszka, R. Exploration of the fundamentals and quantitative applications of matrix assisted laser desorption ionization time-of-flight mass spectrometry (MALDI-TOFMS) in polymer analysis. PhD, Drexel University, Philadelphia, 2012.
2. Chavez-Eng, C. M. Quantitative aspects of matrix-assisted laser desorption/ionization using electrospray deposition. PhD, Drexel University, Philadelphia, 2002.
3. Erb, W. J. Exploration of the fundamentals of matrix assisted laser desorption/ionization time-of-flight mass spectrometry. PhD thesis, Drexel University, Philadelphia, 2007.
4. Hanton, S. D.; Hyder, I. Z.; Stets, J. R.; Owens, K. G.; Blair, W. R.; Guttman, C. M.; Giuseppetti, A. A., Investigations of electrospray sample deposition for polymer MALDI mass spectrometry. *Journal of the American Society for Mass Spectrometry* 2004, *15*, 168-179.
5. Cloupeau, M.; Prunet-Foch, B., Electrohydrodynamic spraying functioning modes: a critical review. *Journal of Aerosol Science* 1994, *25* (6), 1021-1036.
6. Rietveld, I. B.; Kobayashi, K.; Yamada, H.; Matsushige, K., Electrospray Deposition, Model, and Experiment: Toward General Control of Film Morphology. *The Journal of Physical Chemistry B* 2006, *110* (46), 23351-23364.
7. Juraschek, R.; Röllgen, F. W., Pulsation phenomena during electrospray ionization. *International Journal of Mass Spectrometry* 1998, *177* (1), 1-15.
8. Salim, A.; Son, C.; Ziaie, B., Selective nanofiber deposition via electrodynamic focusing. *Nanotechnology* 2008, *19* (37), 375303.
9. Leong, K. H., Morphology of aerosol-particles generated from the evaporation of solution drops. *Journal of Aerosol Science* 1981, *12* (5), 417-435.
10. Tang, K. The electrospray: fundamentals and feasibility of its application to targeted drug delivery by inhalation. PhD, Yale University, New Haven, 1994.
11. Hao, X.; Lu, X.; Li, Z.; Zhao, Y.; Shang, T.; Yang, Q.; Wang, C.; Li, L., Effects of the electrospray ionization parameters on the formation and morphology of colloidal microspheres of polyacrylonitrile. *Journal of Applied Polymer Science* 2006, *102*, 2889-2893.
12. Ivo B. Rietveld, K. K., Hirofumi Yamada, Kazumi Matsushige,, Model Supported Morphology Control of Electrospray Deposited Poly(vinylidene fluoride) Film. *Macromolecular Symposia* 2007, *249-250* (1), 322-329.
13. Morozov, V. N.; Morozova, T. Y., Electrospray Deposition as a Method for Mass Fabrication of Mono- and Multicomponent Microarrays of Biological and Biologically Active Substances. *Analytical Chemistry* 1999, *71*, 3110-3117.
14. Allwood, D. A.; Dyer, P. E., Quantitative fluorescence measurements performed on typical matrix molecules in matrix-assisted laser desorption/ionisation. *Chemical Physics* 2000, *261* (3), 457-467.
15. Bashir, S.; Mutter, R.; Giannakopoulos, A. E.; Wills, M.; Derrick, P. J., Parameterising matrix-assisted laser desorption/ionisation (MALDI): strategy for matrix-analyte selection and effect of radical co-additives on analyte peak intensities. *Analytica Chimica Acta* 2004, *519* (2), 181-187.
16. Ganan-Calvo, A. M., Cone-jet analytical extension of Taylor's electrostatic solution and the asymptotic universal scaling laws in electro spraying. *Physical Review Letters* 1997, *79*, 217-220.
17. Kebarle, P.; Verkerk, U. H., Electrospray: from ions in solution to ions in the gas phase, what we know now. *Mass Spectrometry Reviews* 2009, *28* (6), 898-917.



18. Jorabchi, K.; Smith, L. M., Single Droplet Separations and Surface Partition Coefficient Measurements Using Laser Ablation Mass Spectrometry. *Analytical Chemistry* 2009, *81* (23), 9682-9688.
19. Rosell, J. Size characterization in electrosprays of submicron droplets. Yale University, 1994.
20. Rietveld, I. B.; Kobayashi, K.; Yamada, H.; Matsushige, K., Model supported morphology control of electrospray deposited poly(vinylidene fluoride) film. *Macromolecular Symposia* 2007, *249/250*, 322-329.
21. Baumgartner, F.; Schauer, C., On the formation mechanism of hollow-sphere aerosols. *Journal of Aerosol Science* 1989, *20* (8), 879-882.
22. Leong, K. H., Morphological control of particles generated from the evaporation of solution droplets: Experiment. *Journal of Aerosol Science* 1987, *18* (5), 525-552.
23. Leong, K. H., Morphological control of particles generated from the evaporation of solution droplets - theoretical considerations. *Journal of Aerosol Science* 1987, *18* (5), 511-524.
24. Jiang, Y.; Yu, Y.; Sun, W.; Chen, C.; Meng, G.; Gao, J., Electrostatic Spray Assembly of Nanostructured La<sub>0.7</sub>Ca<sub>0.3</sub>CrO<sub>3- $\delta$</sub>  Films. *Journal of The Electrochemical Society* 2007, *154* (8), E107-E111.
25. Nemes, P.; Marginean, I.; Vertes, A., Spraying Mode Effect on Droplet Formation and Ion Chemistry in Electrosprays. *Analytical Chemistry* 2007, *79*, 3105-3116.
26. Westman, A.; Demirev, P.; Huth-Fehre, T.; Bielawski, J.; Sundqvist, B. U. R., Sample exposure effects in matrix-assisted laser desorption/ionization mass spectrometry of large biomolecules. *International Journal of Mass Spectrometry and Ion Processes* 1994, *130* (12), 107-115.
27. Dreisewerd, K., The desorption process in MALDI. *Chemical Reviews* 2003, *103* (2), 395-425.
28. Knochenmuss, R., Ion formation mechanisms in UV-MALDI. *Analyst* 2006, *131* (9), 966-986.
29. Knochenmuss, R.; Stortelder, A.; Breuker, K.; Zenobi, R., Secondary ion-molecule reactions in matrix-assisted laser desorption. *Journal of Mass Spectrometry* 2000, *35* (11), 1237-1245.
30. Zenobi, R.; Knochenmuss, R., Ion formation in MALDI mass spectrometry. *Mass Spectrometry Reviews* 1999, *17*, 337-366.
31. Georgiou, S.; Koubenakis, A., Laser-induced material ejection from model molecular solids and liquids: Mechanisms, implications, and applications. *Chemical Reviews* 2003, *103* (2), 349-393.

## Chapter 5. Exploring the Effects of Laser Wavelength on Matrix and Analyte Signal in MALDI-TOFMS

### Motivation

Commercial UV-MALDI instruments are typically equipped with one of two wavelengths for desorption of the matrix and analytes. The two wavelengths, 337nm and 355nm, are generated by nitrogen lasers (337nm) or frequency tripled Nd:YAG lasers (355nm). Since commercial instruments are typically sold with a single laser source, most of the MALDI is generated at one of these two wavelengths. A recent trend in MALDI instruments has seen them built almost exclusively with YAG lasers operating at 355nm. YAG lasers offer higher repetition rates as compared to nitrogen lasers and are therefore better suited to the emerging field of MALDI imaging MS<sup>1-3</sup>. Another reason for this switchover is a perception of higher stability of YAG lasers and lower operating costs. There are a limited number of nitrogen laser producers and the cost of replacing the short life-time sealed nitrogen laser cartridge is high.

There is little reference in the literature discussing the differences between the two wavelengths. However, a paper written by Zhang and Kinsel describing a quantitative method to determine protein surface absorption by MALDI employed a home-built instrument equipped with both 337nm and 355nm wavelength lasers<sup>4</sup>. Their work generated a unique comparison between the two wavelengths. They demonstrated that under identical sample preparation conditions and similar instrument conditions the 355nm laser produced greater sensitivity for the matrix and analyte combinations tested. Figure 5.2 is reproduced from their work. For nearly all the conditions tested the slopes for the standard addition calibration curves of porcine Insulin are greater at 355nm. This suggests 355nm is more sensitive than the 337nm wavelength

in the MALDI experiment, a point that was made by the authors but not further explored. A thorough literature search of citing articles revealed that this phenomenon has not been further investigated. It should be of importance for future MALDI work to determine if this phenomenon can be recreated with more matrices and other analytes using the two wavelengths.

Once the sample has been introduced into the instrument, the process of obtaining a mass spectrum from the sample via MALDI can be broken into two steps. The first is the desorption of the matrix and analyte from the solid surface, while the second is the ionization of the matrix and analyte compounds prior to their acceleration out of the source. The experimentally observable differences observed in the MALDI spectra by Zhang and Kinsel<sup>4</sup> could arise from differences in either the desorption characteristics of the matrix compounds or the ionization efficiency of the analytes and matrix compounds at the differing wavelengths. Though we will treat these as separate steps here, the two processes are often difficult to separate in practice. The following will be a brief discussion of the desorption and ionization processes in MALDI as discussed in the literature.

Table 5.1: Experimentally determined slopes for the calibration curves of porcine Insulin using MALDI with incidence wavelengths of 337nm and 355nm. Table reproduced from Zhang and Kinzel<sup>4</sup>

	337-nm MALDI			355-nm MALDI		
	ng/cm <sup>2b</sup>	slope × 10 <sup>5</sup>	R <sup>2</sup>	ng/cm <sup>2a</sup>	slope × 10 <sup>5</sup>	R <sup>2</sup>
<b>Matrix: ACHCA</b>						
PEEK	139 ± 7	1.18	0.998	120 ± 20	15.5	0.982
LDPE	49 ± 21	1.54	0.985	33 ± 9	7.23	0.998
<b>Matrix: SA</b>						
PEEK	129 ± 4	2.43	0.998	152 ± 36	4.34	0.948
LDPE	49 ± 23	1.82	0.979	34 ± 23	1.72	0.987
<b>Matrix: DHB</b>						
PEEK	130 ± 20	2.23	0.947	110 ± 10	6.48	0.995
LDPE	44 ± 11	1.66	0.991	31 ± 18	2.10	0.993
<b>Matrix: FA</b>						
PEEK	140 ± 10	1.51	0.963	130 ± 20	3.27	0.990
LDPE	46 ± 23	1.53	0.991	48 ± 26	1.28	0.982

<sup>a</sup> The quantity of tightly bound porcine insulin that is not removed by an SDS wash. <sup>b</sup> The values shown represent the x-intercepts of the MALDI standard additions plots and the errors in these values as calculated according to ref 35.

## Introduction

### *Desorption*

The MALDI technique was first introduced in the mid-1980s as a technique for analyzing intact large molecules in excess of 10kDa using an irradiation wavelength of 266nm<sup>5,6</sup>. In the mid to late 1980s research groups studying laser desorption ionization (LDI) were generally using frequency quadrupled Nd:YAG lasers (266nm) or excimer lasers (308nm) to analyze lower molecular weight compounds by mass spectrometry. By extension these same groups began to adopt the MALDI technique and continued to use the same laser wavelengths. Later nitrogen lasers, producing a beam of 337nm light, were used for MALDI experiments. Today commercial instruments are equipped with either nitrogen lasers (337nm) or a frequency tripled Nd:YAG laser (355nm). The type of laser and specific wavelength should be of critical importance to the MALDI experiment. Once a sample has been prepared the next step to forming ions is to desorb the material from the surface of the MALDI probe. This is accomplished by using organic matrix

materials that absorb highly at the wavelength used for desorption<sup>7</sup>. The energy from the laser pulse is absorbed by the matrix molecules and in turn provides the energy required for rapid desorption from the sample surface. During desorption and the resulting plume expansion analyte ions are created from interactions with the ionized matrix molecules. This concept will be discussed further in this chapter. For now we will focus on the desorption process and the role that laser wavelength plays in its mechanism.

Wavelengths between 248 and 355nm are typically employed for MALDI experiments. A summary of the critical aspects of the desorption process was written by Dreisewerd in 2003<sup>7</sup>. In this paper he notes that a thorough review and therefore understanding of the effects of wavelength in this useable range has not been undertaken. A more recent review of the literature uncovers a continued lack of research done in this area. Table 5.2 provides a concise list of the important laser parameters for the MALDI experiment from his work.

**Table 5.2: Table of relevant MALDI laser parameters reproduced from Dreisewerd<sup>7</sup>.**

parameter	range	typical values for common matrixes and a laser spot diameter of ~100 $\mu\text{m}$
laser wavelength, $\lambda$	193–430 nm	(266), 337, 355 nm
laser penetration depth into the sample, $\delta$ ( $= \alpha^{-1}$ ; $\alpha$ : absorption coefficient)	~ 50–300 nm	50–200 nm
photon energy at laser wavelength, $E_\nu$	2.9 eV (430 nm) – 6.5 eV (193 nm)	4.71 eV (266 nm), 3.72 eV (337 nm), 3.53 eV (355 nm)
laser pulse duration, $\tau$	0.5 – ~20 ns, (560 fs <sup>d</sup> )	0.5–10 ns
diameter of laser spot on sample surface	1 $\mu\text{m}$ – ~1 mm	50–200 $\mu\text{m}$
energy per single laser pulse as applied to the sample, $E$	10 nJ – 10 $\mu\text{J}$ <sup>b</sup>	1–10 $\mu\text{J}$
mean power of a single laser pulse, averaged over the pulse duration ( $1/e^2$ -definition) <sup>c</sup> , $P_{\text{avg}}$	1–5 $\times 10^3$ W <sup>b</sup>	10 <sup>2</sup> W – 5 $\times 10^3$ W
fluence (energy per laser pulse and unit area), $H$ <sup>d</sup>	30 – ~10,000 $\text{Jm}^{-2}$ <sup>b</sup>	30–600 $\text{Jm}^{-2}$
irradiance (fluence divided by the laser pulse duration), $I$	3 $\times 10^3$ – 1 $\times 10^9$ $\text{Wcm}^{-2}$ <sup>b</sup>	1 $\times 10^6$ – 5 $\times 10^7$ $\text{Wcm}^{-2}$

<sup>a</sup> Ref 53. <sup>b</sup> Values strongly depend on the focal laser spot size. <sup>c</sup> For near Gaussian pulse shape the peak power is about two times the average power. <sup>d</sup> Often denoted as  $F$  or  $\Phi$ , instead.

Of the parameters listed in Table 5.2 the most widely discussed in the literature have been fluence<sup>8-11</sup> and the photon energy<sup>12-14</sup>. The photon energy is a characteristic of the type of laser being used while the fluence is a function of the laser intensity and laser spot size on the

surface of the sample. The energy per photon of a laser is defined by the wavelength of the laser being used and is important in that the ionization of the matrix molecules in the MALDI experiment is believed to proceed by photoexcitation from the absorption of one or more photons<sup>15</sup>. For desorption, the absorption of the laser energy facilitates the breaking of bonds between molecules in the solid state. The energy supplied must both produce primary ions of the matrix molecules and be sufficient to overcome the lattice energy of the solid sample. These two processes combine to result in the production of ionized analyte molecules in the expanding plume.

### ***Ionization***

Ionization in the MALDI experiment is typically broken into a two step process. The details of primary ionization are still debated in the literature. The two dominant models for primary ionization are the lucky survivor model<sup>16,17</sup> and the energy pooling model<sup>15</sup>. Karas et al. proposed the lucky survivor mechanism as an encompassing theory to explain the experimental observables in MALDI. Simply, their theory states that the ions observed in the MALDI experiment are largely derived from preformed analyte ions that are present in the solid sample. When the matrix and analyte are desorbed, they form clusters of matrix and analyte ions. The clusters are then desolvated in the gas phase in the desorbing MALDI plume. During this stage free electrons and ionized matrix and analyte molecules are continually colliding, effectively transferring charge and ultimately leading to the ions observed in the experiment. Figure 5.1 illustrates the principles of this theory. The authors believe that this theory explains the prevalence of primarily singly charged analyte molecules in the MALDI experiment, as multiply charged ions would not be thermodynamically favored in this model. This theory largely hinges on observations of matrix and analyte solutions in various pH ranges<sup>18</sup>. Dyes sensitive to pH were mixed with MALDI solutions and upon drying of the solutions they largely retained the

same color in the crystalline form as in the solution phase. It was then postulated that the ionic states of the matrix and analytes are conserved in the solid formed by evaporation of the solvent. These ionized analytes are then simply ablated and enter into the plume. A large excess of electrons and neutral species in the expanding plume interact with the preformed ions, effectively neutralizing them. The resultant mass spectrum is a survey of those ions that “survived” and made it to the detector.

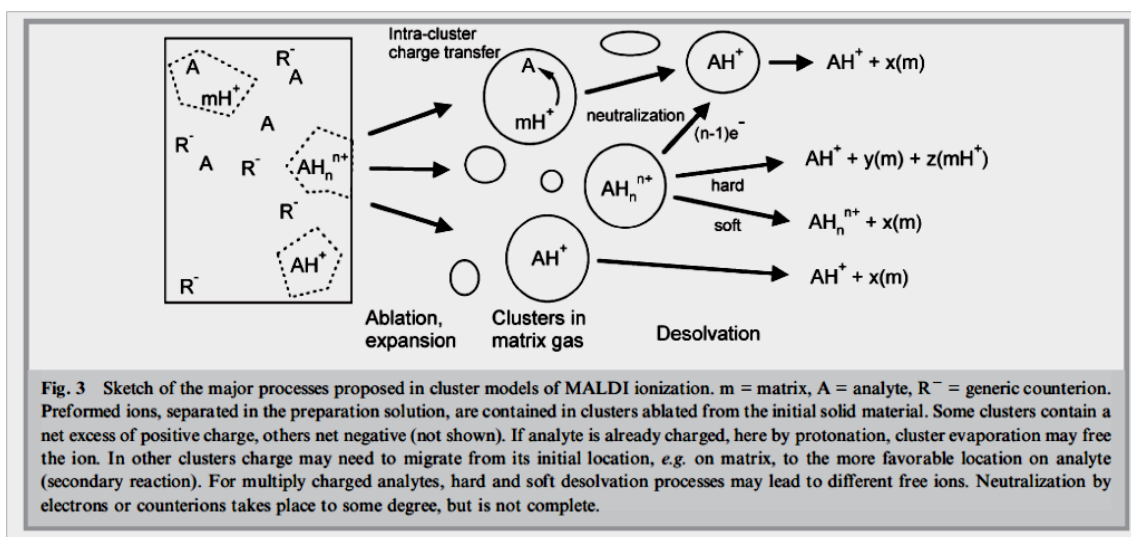


**Figure 5.1:** A sketch of the proposed processes occurring in the lucky survivor ionization theory adapted from Knochenmuss' 2006 review article<sup>15</sup>.

The second theory on primary ionization has been advanced by Knochenmuss and is termed the energy pooling model<sup>15</sup>. This model has been used to account for the low probability of a single matrix molecule absorbing two or more photons directly to become ionized due to the low intensities of laser light used in the MALDI experiment. Instead it is postulated that the excited states of neighboring matrix molecules can overlap and combine in pooling events. In a typical event two molecules in an excited  $S_1$  state come into proximity and the energy from one is transferred to the second resulting in one molecule in a higher excited state,  $S_n$  and the other

in ground state,  $S_0$ . Multiple interactions of this nature eventually lead to the ionization of a matrix molecule. It is also important to note that molecules are not required to be immediate neighbors for this phenomenon to occur. Aromatic compounds in the solid state can facilitate this pooling action by exciton migration<sup>15</sup> or “hopping”. A diagram of this process is presented in Figure 5.2.

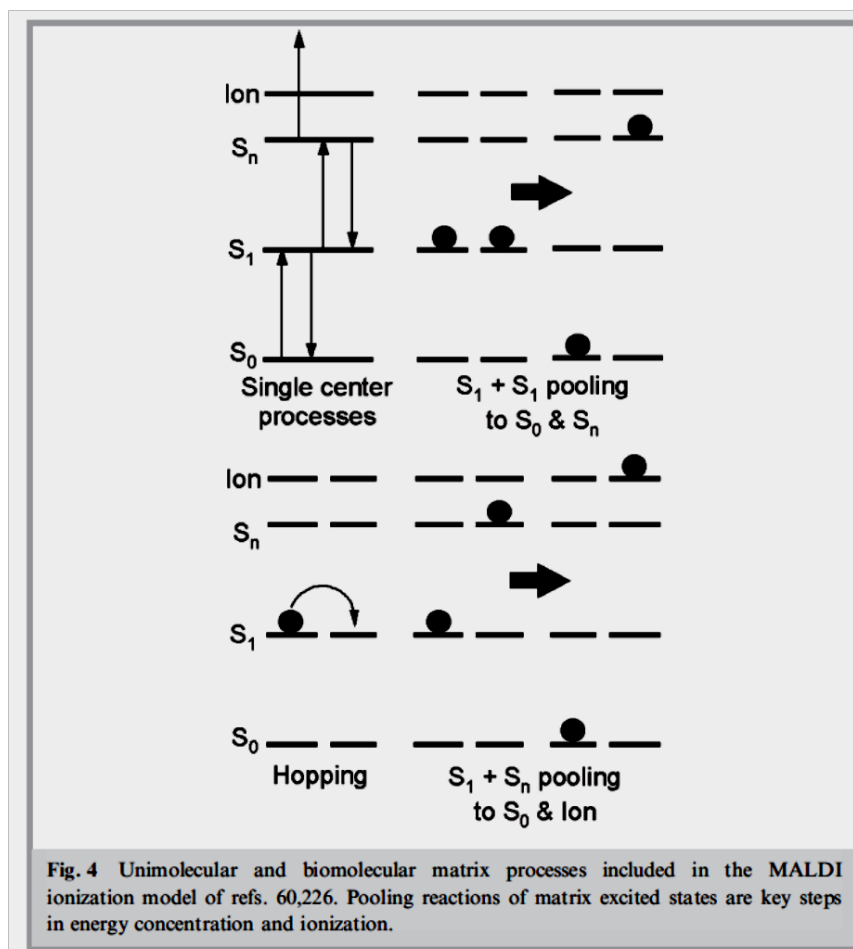


Figure 5.2: An illustration of the pooling mechanism for MALDI ionization. This figure is reproduced from Knochenmuss<sup>15</sup>.

Though the process of primary ionization is still debated there seems to be consensus on the mechanisms for secondary reactions that occur in the expanding plume<sup>19-23</sup>. These



reactions are largely dominated by proton transfer reactions between acidic and basic molecules in the gas phase. Radical reactions and electron transfer reactions are also known to take place in the plume<sup>15, 24, 25</sup>. These secondary reactions lead to the production of the ions detected in the MALDI experiment. For analytes such as peptides or proteins, the relative acidity of an analyte as compared to the matrix being used is important to the experimental outcome. Also, of great importance are the concentrations of the reactants in the plume, the density of the plume and the time in which the reactants have to interact. These processes will be considered further in the discussion of the experiments in this chapter.

### ***Chapter Organization***

This chapter will detail the experiments conducted in order to confirm the observations of Kinsel and Zhang<sup>4</sup> as well as results of additional experiments conducted to gain insight into the desorption and ionization mechanisms operating in the MALDI experiment. An examination of the absorption spectra of common UV-MALDI matrix compounds will be made in both the solution phase and solid state. These experiments are followed by a two wavelength study of the matrix-to-analyte (M/A) plots for a system of Ang I in CHCA. The background spectra of common matrix compounds at 337 and 355nm will also be discussed.

## **Experimental**

### ***Matrix Studies***

Matrix compounds were prepared at a concentration of 0.10M in MeOH, except for dithranol, which was prepared at a concentration of 0.10M in THF. The solutions were analyzed by the dried drop technique. One microliter of each solution was placed on the MALDI probe and allowed to air dry. Positive and negative polarity mass spectra were taken for each matrix using a Bruker Reflex III MALDI-TOFMS instrument. All voltages and instrument parameters were

held constant for both wavelengths. IS1 was 20kV, IS2 was 15.3kV, lens was 7.1kV, reflector was 23kV, and the detector was set to 1.55kV. The resultant spectra were calibrated using Bruker FlexAnalysis software using the monoisotopic masses of the matrix ions that were identified in the spectra.

In order to perform the two wavelength studies, a second laser was added to the Bruker Reflex III instrument in use in our lab. A diagram of the modified light box is shown in Chapter 2. The standard nitrogen laser was aligned into the instrument prior to the alignment of the Nd:YAG laser. The beam shape on the probe surface and the ion signal were first optimized for the nitrogen laser. The YAG beam was then adjusted independently to optimize the ion signal in the instrument. The set up of the light box allowed for switching between the two wavelengths while a sample was in the instrument. Typically it took one minute to change between the lasers and acquire data at the alternate wavelength. The ability to easily and quickly switch between the two wavelengths for the same sample helped to minimize variability in the results for each wavelength that may arise from different sample preparations.

The intensity of each beam was measured prior to entering the instrument by diverting the beam into a power meter equipped with a pyroelectric energy probe. For experiments involving measuring the amount of material desorbed by the two different lasers, an additional set of mirrors and lenses matching those found in the Reflex III were used to direct and focus the laser beams onto a QCM crystal. Note that the reflectance/transmission of all mirrors and lenses used in the instrument were measured using a Perkin-Elmer Lambda-950 UV-visible absorption spectrometer to ensure no significant differences in the reflection/transmission properties that would lead to energy deposition discrepancies.

### ***Solution-Phase UV-Visible Spectroscopy***

Stock solutions of each matrix compound were prepared at a concentration of 0.10M in MeOH or THF (dithranol only). Serial dilutions of the stock solutions were made to reach ~0.1-1mM solutions for analysis. Spectra were collected between 220 and 850nm in double-beam mode using the dissolution solvent as reference. The molar absorptivity for each compound was calculated at the wavelength of interest using a single concentration point.

### ***Solid-State UV-Visible Spectroscopy***

Matrix compounds were mixed with lanthanum oxide (>99%), purchased from Fischer Scientific Company, to produce ~5% by weight mixtures of the matrix compound in the solid mixture. The mixture was homogenized using stainless steel vials and a steel ball bearing. The ball bearing was placed into the vial with the matrix powder and was vortexed for 1 minute on a Vortex-Genie II. The homogenized mixture was then spread onto an anodized solid state sample holder equipped with a UV transparent window for analysis. Spectra were collected between 220 and 850nm in double-beam mode on the PE Lambda-950 instrument equipped with a Labsphere, Inc. (North Sutton, NH) 60mm diameter diffuse reflection sphere using a Spectralon (Labsphere) disc as a reference.

### ***Matrix-to-Analyte Plots***

A stock solution of 1.0 mg/mL of Ang I was prepared using 18 M $\Omega$  D.I. water as the solvent. An appropriate volume of the peptide stock was added to each sample to obtain the desired molar M/A ratio. The matrix concentration was held constant at 0.02M in MeOH in the final spraying solutions. The samples were sprayed using the controlled ESD technique from a height of 20mm and a flow rate of 2 $\mu$ L/min for two minutes with an applied voltage of 5.7KV. Mass spectra were acquired using the Reflex III MALDI TOFMS. All instrument conditions were held constant between the two wavelengths. The same sample solutions were used for each

analysis. Five 50 shot accumulations were collected for each sample and averaged prior to plotting.

### ***QCM Experiments***

The sensing electrode of the crystal was coated with pure CHCA using the controlled electro spray deposition technique. CHCA (0.02 M in methanol) was sprayed from a distance of 30mm at 2.0uL/min for ~5 minutes at a voltage of 6.5kV producing an amorphous coating of matrix directly on the crystal. The crystal was then mounted into the MALDI instrument near the focal length of the focused laser beam.

Each laser was fired at a repetition rate of 10 Hz onto “clean” spots on the coated QCM surface continuously until no more mass was removed from the crystal. Micrographs of the burn profiles were captured at 200X magnification using an Intel Plug & Play microscope to calculate the area of the beam. The laser energy and spot area were adjusted to be similar for both wavelengths. In this manner the fluence at each wavelength was similar and allowed for a better comparison at each wavelength.

## **Results and Discussion**

### ***Matrix Absorption Spectra***

The solution phase and solid state UV-visible absorption spectra of various common matrix compounds were collected to determine the differences in absorption at the wavelengths of 337 and 355nm. The solution phase spectra showed consistent absorption differences between all matrix compounds for the two wavelengths, with the exception of vanillic acid, which actually had the greatest absorbance at 266nm. Vanillic acid was a commonly used matrix for early MALDI work using the frequency quadrupled Nd:YAG laser at a wavelength of 266nm<sup>5, 11, 26</sup>. Table 5.3 shows the solution phase absorbance, calculated molar absorptivity,

and absorbance ratio between 337 and 355nm for the matrix compounds studied. The absorption coefficients measured are similar to those reported in the literature<sup>27, 28</sup>.

**Table 5.3: List of common MALDI matrix compounds analyzed by solution phase UV-Vis spectroscopy. The absorbance at 266, 337, and 355nm are reported. The absorption coefficients for both 337 and 355nm have been calculated and their ratios compared. It is important to note that these measurements were made in MeOH and their absorbance are likely influenced by the dissolution solvent.**

Common Name	Conc. (mM)	Absorbance			ε-value		Ratio
		266 nm	337 nm	355 nm	337nm	355nm	
DHB	0.11	0.015	0.381	0.152	3,510	1,395	2.5
CHCA	0.10	0.167	2.234	1.430	22,138	14,170	1.6
Dithranol	0.10	0.721	0.643	0.883	6,508	8,941	0.7
Sinapinic Acid	0.10	0.354	1.017	0.291	3,530	2,906	3.5
Ferulic Acid	0.10	0.662	0.895	0.167	8,876	1,651	5.4
THAP	0.10	0.641	0.230	0.079	2,358	811	2.9
HABA	0.02	0.034	0.205	0.219	20,135	21,550	0.9
IAA	0.10	0.903	1.337	0.389	13,647	3,975	3.4
Vanillic Acid	0.98	3.391	0.019	0.009	19	9	2.1
ATT	0.10	1.680	0.203	0.077	1,964	745	2.6
ANP	0.10	0.153	1.227	1.083	12,427	10,969	1.1
4-NA	0.10	0.140	0.813	1.265	8,242	12,829	0.6
1,5-DAN	0.10	0.168	1.009	0.208	10,392	2,138	4.9

The ratio of the absorbance at 337 versus 355nm as presented in Table 5.3 shows that there are in some cases significant differences in the absorption for many commonly used matrices. In particular, the absorption at 337nm for DHB, CHCA, ferulic acid and sinapinic acid are large as compared to 355nm. While the dissolution solvent will impact the absolute absorption of the compounds, we have been careful to analyze them in a MALDI relevant solvent, MeOH. These absorbance differences have been noted in the literature and are often used to explain the apparent fluence dependence of ion onset in MALDI<sup>7, 15, 25, 29</sup>. However, these experiments have generally compared irradiation of samples at 337nm and 355nm with other wavelengths in the visible region<sup>30, 31</sup>, the Infrared region<sup>28, 32-35</sup>, and even the UV region<sup>33</sup>, but they have not been compared directly. The outcome of the experiments, regardless of the incidence wavelength used, have suggested that the absorbance of the matrix at the wavelength

used directly impacts the experimental MALDI spectra, where those matrices that absorb more strongly yield greater analyte ion signals<sup>15, 25, 29, 33</sup>. However, this does not support the findings of Kinsel and Zhang<sup>4</sup> as discussed previously.

The absorbance of an organic compound can be influenced by its local environment. Therefore, it may not be appropriate to use solution phase absorbance as a deterministic parameter for MALDI experiments. In UV-MALDI the analytes and matrix are normally interrogated as a solid mixture in the instrument. Therefore the solid state absorbance of the matrix compounds should be a better predictor for the effectiveness of a matrix in MALDI. Table 5.4 shows results from the diffuse reflectance solid state UV-Vis absorption measurements made on the same MALDI matrix compounds as listed in Table 5.3.

**Table 5.4: List of common MALDI matrix compounds measured by diffuse reflectance UV-Vis spectroscopy at 266, 337, and 355nm. The relative absorbance values are presented as well as the ratio of the absorbance values for each compound at 337 and 355nm.**

Common Name	Absorbance			Ratio
	266 nm	337 nm	355 nm	337/355
DHB	0.2637	0.5735	0.5069	1.1
CHCA	0.1598	0.4814	0.4615	1.0
Dithranol	0.2403	0.2308	0.2909	0.8
Sinapinic Acid	0.12	0.3503	0.3205	1.1
Ferulic Acid	0.04741	0.1814	0.1526	1.2
THAP	0.2933	0.4186	0.3276	1.3
HABA	0.05638	0.1545	0.1974	0.8
IAA	0.2706	0.448	0.3986	1.1
Vanillic Acid	0.2729	0.07505	0.03537	2.1
ATT	0.3421	0.07108	0.08124	0.9
ANP	0.0452	0.1714	0.2119	0.8
4-NA	0.0875	0.3891	0.4629	0.8
1,5-DAN	0.1319	0.3626	0.2879	1.3

The solid state UV spectra of the matrix compounds show differences in the absorbance between 337 and 355nm wavelengths that are smaller than those differences observed in the solution phase spectra. Table 5.4 demonstrates that most of the matrix compounds absorb

efficiently at both 337 and 355nm. The ratio between 337 and 355nm is close to one for all the matrix compounds; this is a result of peak broadening and slight red shifts in the solid state diffuse reflectance spectra. The same phenomenon has been reported by others for various matrix compounds for a more limited number of matrix molecules or focused on the absorbance differences between positional isomers of DHB<sup>11,36</sup>. A selection of the solution and solid state spectra for the matrix compounds analyzed in this work is found in Figure 5.3. These spectra clearly demonstrate the peak broadening and red shifting in the solid state spectra. They also illustrate that the spectral shifting is not equal for all compounds. The solid state spectrum for ATT does not appear to be red shifted far, but it does exhibit peak broadening. The solid state spectra of three popular MALDI matrices, CHCA, 2,5-DHB and SA also shown in Figure 5.3 are distinctly broadened in the solid state as well as red shifted. This helps to explain why all three matrix compounds can be used at both wavelengths with good success.

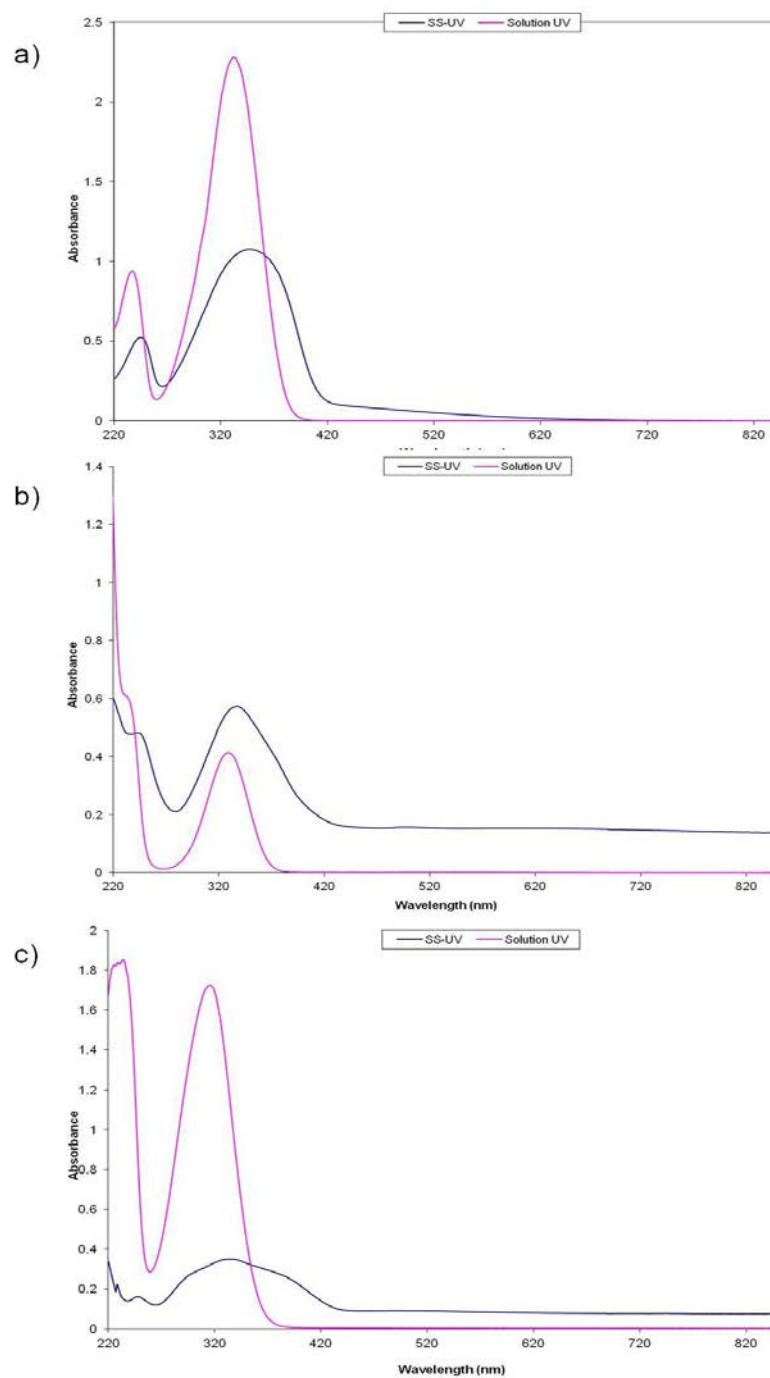


Figure 5.3: Solid state diffuse reflectance and solution phase UV-Vis spectra of four MALDI matrix compounds, a) CHCA, b) 2,5-DHB, and c) SA. The spectra were plotted without normalization; no quantitative data can be discerned from the solid state spectra.



The data from Table 5.3 and Table 5.4 have been consolidated into Table 5.5 for easier comparison between the solution phase and solid state absorbance at 337 and 355nm. When analyzed side by side, the absorption differences between solution and solid state UV-visible spectra are easily discernible. For example, the large discrepancies between 2,5-DHB, sinapinic acid and ferulic acid that are observed in the solution phase are not found to be present in the solid state. This data suggests that the sensitivity observed by Zhang and Kinsel<sup>4</sup> may not be easily explained by the effective absorbance of the matrix at each wavelength.

**Table 5.5: A Comparison between the solution phase and solid state UV-Vis absorbance at 337 and 355nm for common UV-MALDI matrix compounds. The data herein is a summary of Tables 5.4 and 5.5.**

Common Name	Ratio	
	Solution-UV 337/355	SS-UV 337/355
DHB	2.5	1.1
CHCA	1.6	1.0
Dithranol	0.7	0.8
Sinapinic Acid	3.5	1.1
Ferulic Acid	5.4	1.2
THAP	2.9	1.3
HABA	0.9	0.8
IAA	3.4	1.1
Vanillic Acid	2.1	2.1
ATT	2.6	0.9
ANP	1.1	0.8
4-NA	0.6	0.8
1,5-DAN	4.9	1.3

### ***QCM Desorption Studies***

A prerequisite for the observation of ion signal in the MALDI experiment is desorption of the matrix and analyte molecules from the surface<sup>7,15</sup>. Once the material has entered the gas

phase it is rapidly accelerated as an expanding plume in the instrument. In this plume the matrix and analyte molecules interact chemically and generate the secondary ions that are observed in the experiment<sup>15, 19, 37</sup>. The density of the plume, as determined by the amount of solid material desorbed, affects the number of ions observed at the detector<sup>7, 38, 39</sup>. Though we have demonstrated that the absorption of the matrix compounds at 337 and 355nm are similar for common MALDI matrix compounds, these data do not provide insight into the amount of material that is desorbed by each laser shot at the two wavelengths. In order to determine if the amount of matrix desorbed at each wavelength is similar we need to quantitatively measure the material removed from the probe surface by each shot at the two wavelengths. A study of this nature was performed in the early 1990s by Quist et al, however, they did not compare multiple wavelengths<sup>40</sup>. Their study only sought to understand the effects of laser incidence angle on the amount of material removed from the surface and only investigated this phenomenon at 355nm. In our work we are largely concerned with differences that can be attributed to the incident wavelength. To accomplish this, we used two lasers with a common set of optics and a quartz-crystal microbalance (QCM). Due to the difficult nature of these measurements in our lab, CHCA was chosen as an exemplary matrix for these tests.

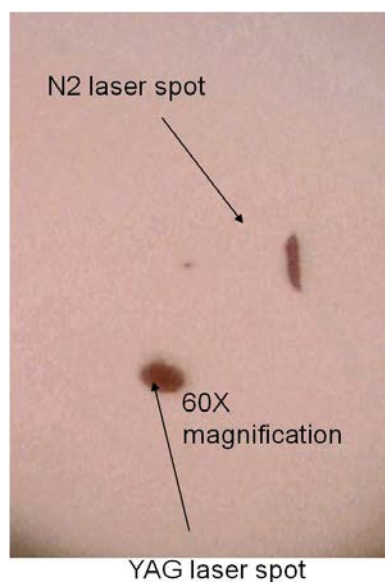


**Figure 5.4: Optical micrograph of the laser spot profile for the 337nm nitrogen laser and the 355nm Nd:YAG laser. The YAG laser produced a spot that was ~6% larger than that of the nitrogen laser spot.**

Figure 5.4 was used to calculate the spot size for both laser beams. As measured using an Edmund Optics 1' x 3' resolution target (Part number 01-21-J31) with markings of 10um per line, the area for the 355nm YAG laser was found to be ~6% larger than that of the 337nm nitrogen laser. Both lasers were held at a constant energy of 6.5uJ/pulse, for which the standard deviation of 1000 shots was measured to be 0.03uJ using the Laser Precision joulemeter. Therefore, the calculated fluence was 344 J/m<sup>2</sup> for the nitrogen laser (337nm) and 323 J/m<sup>2</sup> for the YAG laser (355nm). The fluence for the nitrogen laser was slightly higher than that for the YAG laser as a consequence of the small difference in spot areas. Figure 5.5 and Figure 5.6 show plots of the data collected from the QCM in these experiments. The slope of the mass change curve measured by the QCM was calculated by exporting the QCM data into Excel, This was necessary to determine of the mass removed per laser shot, as the QCM used has a sensitivity limit of 0.4 ng/cm<sup>2</sup>.

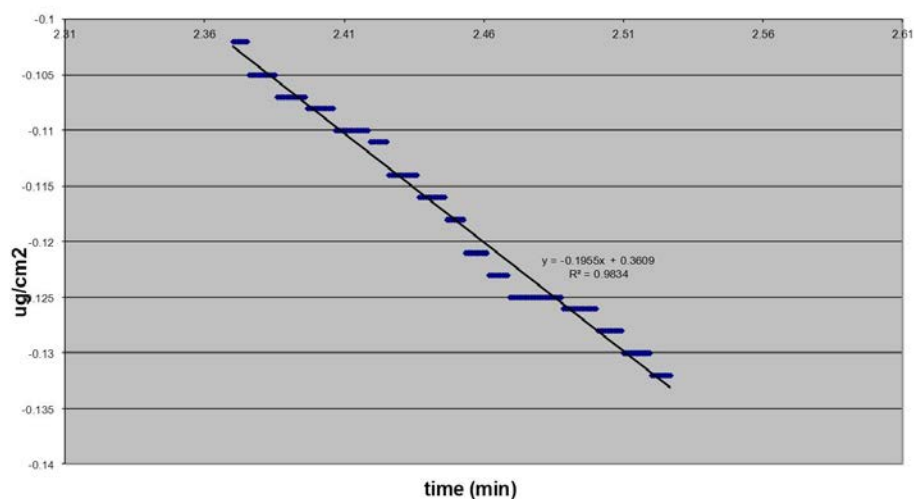


Figure 5.5: QCM data for the change in mass per unit area vs time when irradiated with 337nm laser light. The slope of the fitted line was used for the calculation of material removed per laser shot.

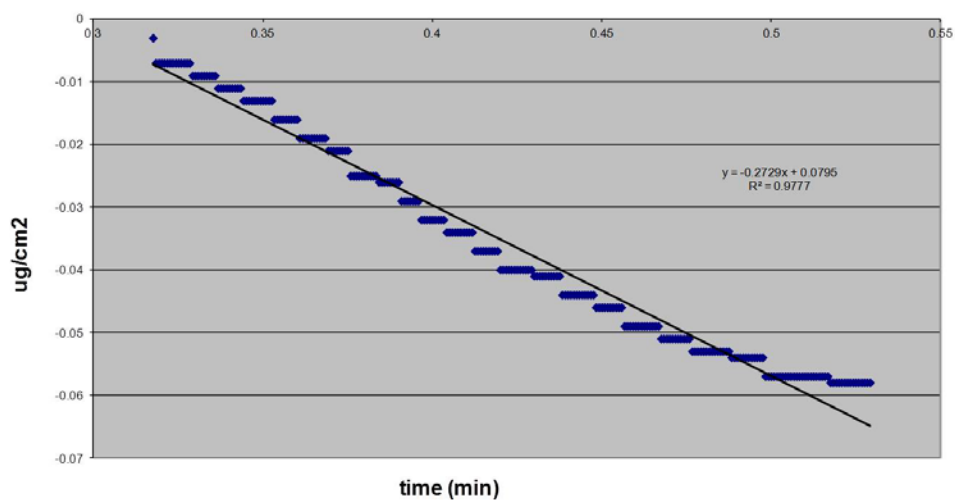


Figure 5.6: QCM data for the change in mass per unit area vs time when irradiated with 355nm laser light. The slope of the fitted line was used for the calculation of material removed per laser shot.

In Figure 5.5 and Figure 5.6 the sensitivity limit of the QCM is clearly observable. There are multiple data points that produce the same reported mass value on each plot. Each laser

shot removes an amount of material that is smaller than the smallest mass change measurable by the QCM. Therefore the slope of the line created by hundreds of shots was needed in order to determine the amount of material removed per shot by each of the laser wavelengths. The area of the conducting surface of the crystal is known and was used to determine the micrograms removed per second as the laser was fired at the sample. Finally, the laser repetition rate was used to derive the mass removed per laser shot. Critical values for the calculation described above are listed in Table 5.6.

**Table 5.6: A list of the critical values calculated for the determination of the mass desorbed as a function of wavelength for CHCA.**

	Laser		units
	Nitrogen	YAG	
Area	1.9E-08	2.0E-08	m <sup>2</sup>
Power	6.5E-06	6.5E-06	J
Fluence	344	323	J/m <sup>2</sup>
Slope	0.196	0.273	ug/cm <sup>2</sup> /min
Corrected mass	0.0669	0.0933	ug/min
mass per shot	0.11	0.16	ng/shot

The calculated mass desorbed per laser shot at 337nm and 355nm is presented in Table 5.6. Although the fluence used for the nitrogen laser is slightly higher than that for the YAG laser, there is an ~45% increase in the amount of mass desorbed at 355nm as compared to 337nm. This is a significant result in that many investigators have suggested that more material is desorbed at higher fluences<sup>8, 29, 38, 41</sup>. It is also significant in that we have already demonstrated that the absorption at 337nm and 355nm wavelengths for CHCA is similar in the solid state UV-

visible absorption spectrum. Further, the solution phase spectra would predict that the amount of light absorbed at 337nm should be 1.6X that at 355nm and thus the nitrogen laser would be predicted to be the optimal laser for this matrix.

The data presented in Table 5.6 supports the claims of Zhang and Kinsel<sup>4</sup>, in that if more matrix and thereby more analyte is desorbed from the surface when using an incident wavelength of 355nm, it may be possible to generate more ions in the expanding plume. However, it is important to note here that the QCM measurements presented were made without analyte and at atmospheric pressure. The experimental data we are trying to understand were collected under vacuum and contained analyte co-crystallized with the matrix. To further investigate this point, samples containing analyte must be analyzed under the same conditions as those detailed for determining the mass desorbed per laser shot. The samples need to be analyzed using a common instrument with lasers optimized to the same or nearly same fluence for both wavelengths.

### ***Matrix-to-Analyte (M/A) Plots for Angiotensin I in CHCA***

Previous members of our group have reported on the importance of the molar ratio between the matrix and analyte used in the MALDI experiment<sup>42</sup>. Other groups have also reported on the effect of molar ratio between matrix and analyte on the analyte signal<sup>43, 44</sup> and fluence dependencies<sup>45</sup>. These other groups largely dealt with the classic dried drop technique for sample preparation and were concerned with the co-crystallization of matrix and analyte molecules. Using a more homogeneous sample preparation technique such as ESD, the effect of M/A molar ratios can be clearly visualized<sup>42, 46</sup>. As described in previous chapters of this thesis, ESD sample preparation creates a homogeneous coating of amorphous particles containing both the matrix and analyte. When samples are prepared in this manner one can clearly identify the

changes in signal intensity as the M/A ratio is modified. M/A plots for a model system, Ang I in CHCA, were prepared and analyzed at 337nm and 355nm to determine if the increase in matrix material desorped at 355nm also increased the sensitivity of the experiment. The quantity of matrix was held constant in these experiments and analyte was titrated into the spraying solutions as has been previously described elsewhere<sup>42</sup>. The resulting M/A plots from these experiments are shown in Figure 5.7.

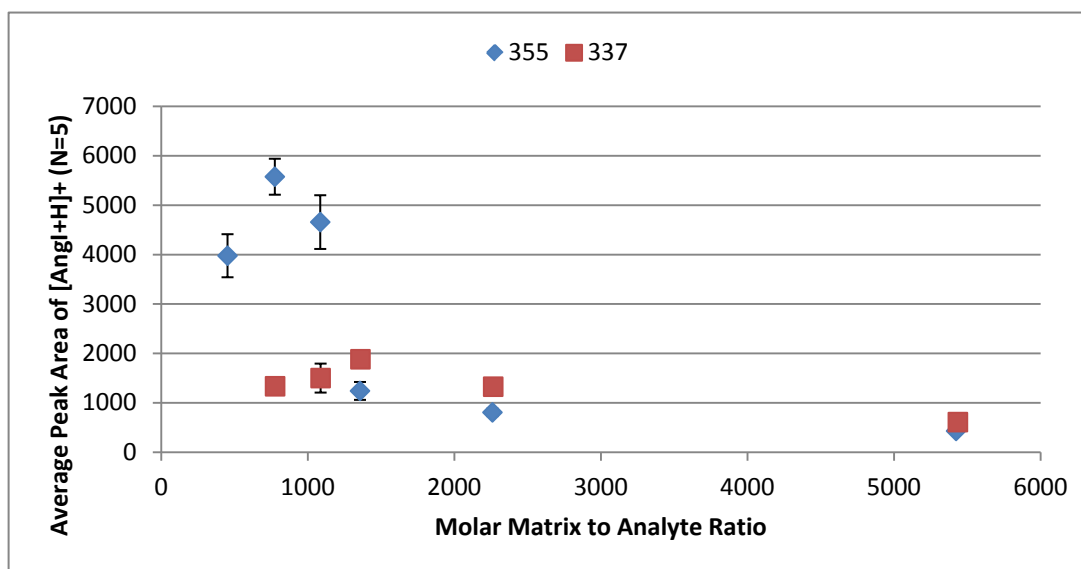


**Figure 5.7:** Matrix to analyte plots of Angiotensin I and CHCA analyzed at 337nm and 355nm wavelengths for desorption. Each data point is an average of the protonated molecular ion of Angiotensin I for 5 individual accumulations of 50 laser shots randomly acquired over the sprayed sample area.

It is important to note that the M/A ratio increases in moving to the right in the plot in Figure 5.7. As compared to a “traditional” analytical calibration curve, smaller quantities of analyte present in the sample would occur on the right in these plots. Note that each of these wavelengths has a linear range for analysis, at 337nm it is above 1300 and for 355nm it is above 700 M/A. It is also noted that the protein analyte signal “saturates” at these values, and then decreases quickly at lower M/A values. Presumably at low values of M/A there is not enough

matrix present in the MALDI sample to effectively both desorb and ionize the analyte<sup>42</sup>. Figure 5.7 clearly demonstrates that there is nearly a 3-fold difference in analyte signal between the two wavelengths for some values of the M/A ratio. The maximum signal for the two wavelengths are significantly different, suggesting that less matrix is needed to produce a maximum signal when using 355nm as the incident wavelength. At M/A ratios less than ~1300:1 there is also a large difference in the total analyte signal. These differences are deemed to be significant because the instrument set-up, including the optical path of the laser beams, the energy of each laser and the laser spot area were held constant for each set of samples. Therefore at similar fluence a significant signal enhancement occurs when a 355nm laser is used.

This finding supports the previously discussed work of Zhang and Kinsel<sup>4</sup>. The goal of their study was to produce calibration curves for insulin using various matrix compounds. For the concentration of CHCA and insulin reported, the minimum M/A ratio they could have obtained was ~450. Previous work in our group suggests that the M/A signal maximum is translated to a larger M/A ratio as the molecular weight of the analyte is increased<sup>42</sup>. This would suggest that they were working at sub-optimal M/A ratios as described by typical M/A plots. The increase in slope that they associated to increased sensitivity is also demonstrated in the plots shown here in Figure 5.7. In the range of M/A values that they were using there is likely a large difference in the slopes of the M/A plot for the different wavelengths, which could account for the perceived sensitivity increase in their study.

### ***Effect of Wavelength on Cationization***

It has already been demonstrated that at 355nm the amount of matrix material desorbed is greater than that desorbed at 337nm. It has also been demonstrated that for a



given matrix and analyte combination that there are values of M/A ratio that produce a larger population of analyte ions using 355nm. The fact that there are M/A ratios where both wavelengths perform similarly suggests that the amount of matrix and analyte desorbed from the surface is not the only factor affecting the analyte signal. If this were true then we should expect to see a uniform increase in ion signal across the entire M/A range in Figure 5.7. Instead there must be other factors affecting the analyte signal. It is likely that ionization in the expanding plume is different between these wavelengths. In order to gain insight into the ionization pathways occurring in the plume we have further examined the raw mass spectra generated from the M/A plots. Generally we concern ourselves with the protonated analyte peak,  $[M + H]^+$ , when examining the effects of analyte and matrix concentrations. However, due to the increased homogeneity of the ESD sample preparation technique, we typically observe alkali (predominantly sodium) cationized analyte molecules. Figure 5.8 is a plot of the ratio between  $[M + H]^+$  analyte signal and sodium cationized analyte signal,  $[M + Na]^+$ .

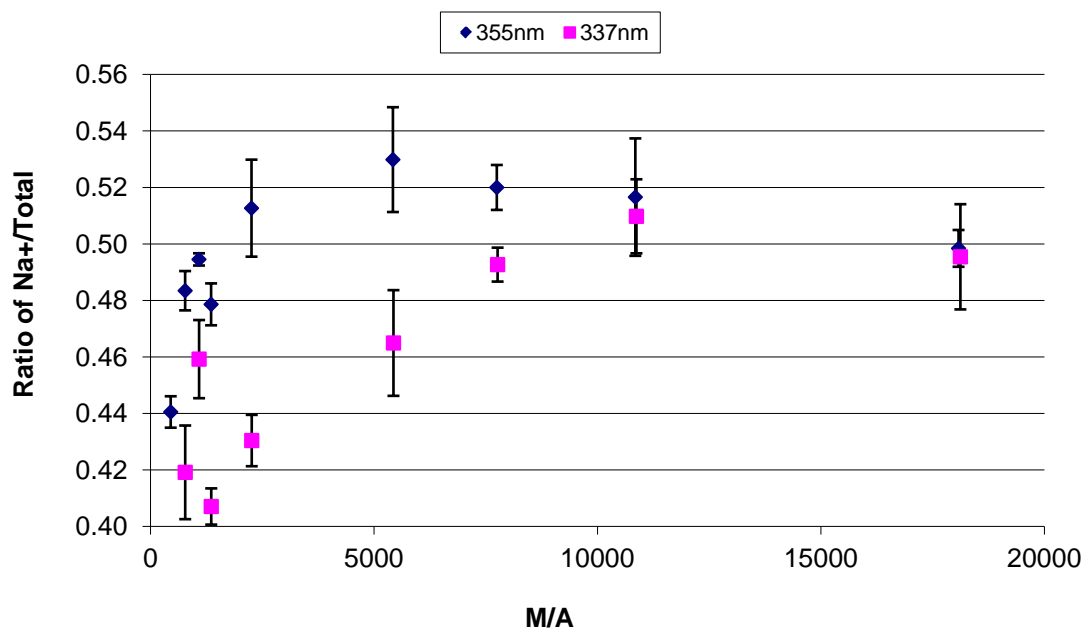


**Figure 5.8:** Plot of the relative sodium cationized analytes signal as a function of matrix to analyte ratio at two commonly used MALDI wavelengths, 337 and 355nm. The sodium ratios are calculated against the total analyte signal for angiotensin I.

Figure 5.8 shows that the ratio of sodium cationized Ang I to the total analyte signal is larger at 355nm as compared to 337nm. A similar trend to that observed in Figure 5.7 can also be seen in this plot that the differences in sodium cationized analyte signal as compared to the protonated signal decreases as the M/A is increased. Of note in this plot is that the consistently higher  $[M + Na]^+$  signal at 355nm combined with the larger  $[M + H]^+$  signal at this wavelength point to better ionization efficiency at 355nm for the analyte. The leveling off of both plots is also interesting. The assumption can be made that on a molar basis that salt present in the sample solutions during spraying come from the matrix and not the analyte solutions. Since the concentration of matrix is held constant in these experiments and the amount of analyte is varied, an increase in M/A would result in a similar increase in the salt- to-analyte (S/A) molar ratio. Though there is likely a large molar excess of salt in the samples at the right end of the plot, the  $[M + Na]^+$  signal does not continue to increase, instead it seems to level off and

possibly even decrease. This is not unlike the S/A plots that have been examined by our group for synthetic polymer analytes<sup>47</sup>. One of the main disadvantages of the ESD technique is the high occurrence of cation adduction. This data suggests that at some S/A ratio the cationized analyte signal could remain constant. This observation could help drive the utility of ESD sample preparation for more quantitative MALDI experiments.

The desorption of more material per laser shot from the surface of a MALDI target leading to larger analyte signal intensities can be explained by our understanding of the secondary reactions that are believed to produce the ions detected in MALDI<sup>15</sup>. In general, more material in the expanding plume created by laser desorption leads to a denser plume. A dense plume will create more analyte ions by way of enhanced matrix-analyte interactions<sup>19</sup>. It is expected that protonation should be energetically favored for a peptide and matrix molecules over cationization<sup>15</sup>. However, our findings suggest that especially for MALDI performed at 355nm, cationization is also a major contributor to analyte ionization. The cationization of Ang I for both wavelengths used in this experiment can be clearly seen in Figure 5.9.

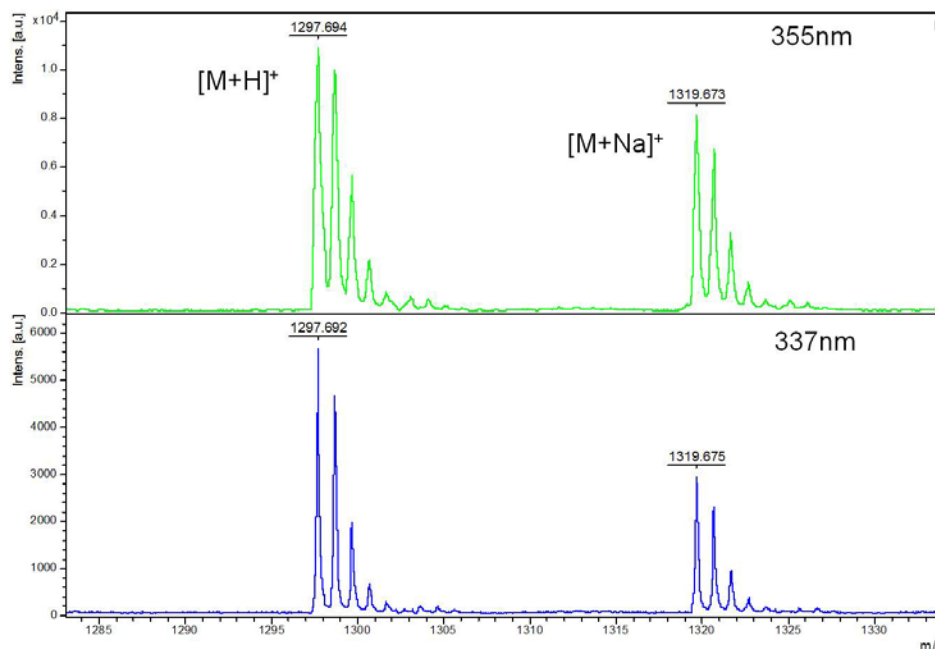


**Figure 5.9: MALDI mass spectra of Angiotensin I using CHCA as a matrix collected on a Bruker Reflex III instrument using two different wavelengths. The M/A ratio for both samples is  $\sim 1300:1$ . The samples were prepared using the controlled ESD technique.**

Figure 5.9 shows the analyte spectra for Angiotensin I collected at the same M/A ratio at the two different wavelengths. The spectrum acquired using the 355nm YAG laser demonstrates the increased  $[M + Na]^+$  as compared to the same sample measured at 337nm. The question remains as to why this is occurring and why it seems to be more favorable at 355nm for certain M/A ratios. One possible explanation for this phenomenon is an increase in cluster formation. It has been shown by various groups that the ionization potential for matrix clusters is lower than that for a single molecule<sup>12, 14, 48-50</sup>. If larger particles of the solid surface are desorbed by the laser and if those clusters effectively lower the ionization potential for the matrix molecules, this could explain the effective increase in ionization efficiency that is observed in the 355nm wavelength experiments. At lower M/A ratios where there is more analyte available for ionization in the plume, this process could lead to higher ion yields. However, the fact that the analyte ion yield appears to be similar at large M/A ratios suggest that at both wavelengths

there is enough ionized matrix available to effectively ionize a large majority of the analyte in the plume, resulting in experimentally similar ionization efficiencies between the wavelengths. A possible extension of this hypothesis is that the increase in cationization occurring at 355nm wavelength is due to an increase in cluster formation of the matrix molecules, which can be stabilized by incorporation of cations in the clusters. If this is the case it should be observable in the background matrix spectra as well.

### ***Matrix Background Spectra***

In order to further understand the effect of the incident wavelength on the matrix molecules, the matrix compounds were analyzed without analyte using both 337 and 355nm wavelengths. The samples were prepared by the dried drop method and analyzed using the same instrument set up as previously described for the M/A plots. Note that the laser spot area and fluence were not controlled for these experiments. The laser power was adjusted to obtain a maximum number of peaks in the background spectrum as these studies were conducted for the purpose of determining the extent of cationization and clustering occurring at each wavelength. The analysis was conducted in both positive and negative polarity. A few commonly used matrix compounds will be discussed in this chapter; the complete set of spectra for all matrices can also be found online at <http://maldimatrixinfo.wikispaces.com>.

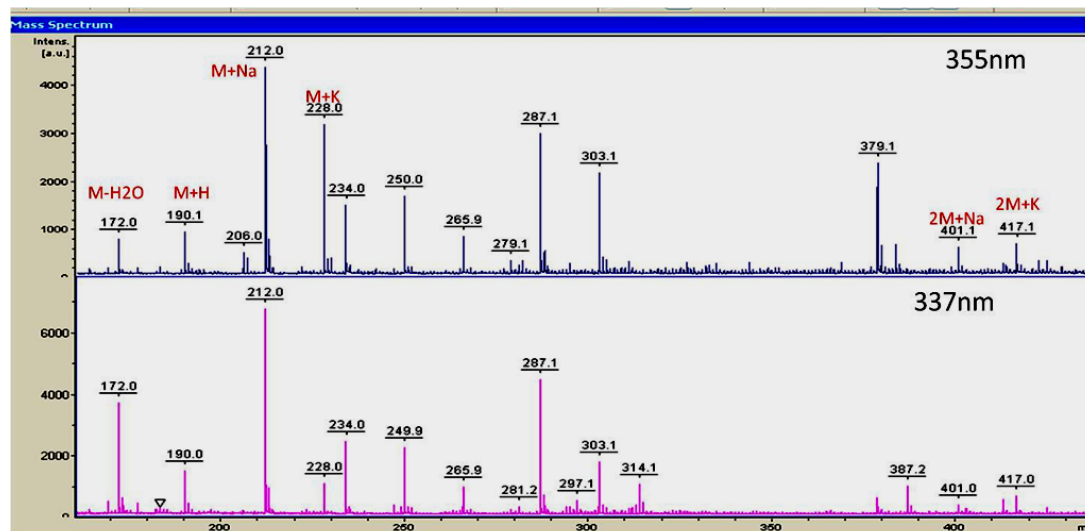


Figure 5.10: Positive polarity mass spectra of CHCA at both 337 and 355nm wavelengths. The table below the spectra illustrate the relative peak area differences for the same matrix compound that the two wavelengths.

Table 5.7: Table showing the ratios of various CHCA background matrix ion peaks compared between 337nm and 355nm wavelength incident light.

CHCA Wavelength	Peak area ratio			
	$[M-H_2O]^+/[M+H]^+$	$[M+Na]^+/[M+H]^+$	$[M+Na]^+/[M+K]^+$	$[2M+Na]^+/[2M+K]^+$
355	0.66	7.74	1.83	0.75
337	2.46	5.25	6.24	0.49

Figure 5.10 shows that the matrix molecule CHCA exhibits a similar trend between the wavelengths that is observed for the analyte molecules in the M/A plots. These trends are presented as peak area ratios in

Table 5.7. The amount of cationization at 355nm is increased when compared to that at 337nm. This increase is also not limited to the sodium cationized molecules; there is also an increase in the amount of potassium cationized species as well. Also of note is that the peak corresponding to the loss of water from the matrix molecule is significantly larger as compared to the protonated matrix peak at 337nm. This could suggest that the desorption process imparts more

energy into the matrix molecules at the shorter wavelength, which leads to an increase in dissociation of the matrix molecules. These differences, coupled with the fact that similar ions are generated for each wavelength but have differing relative intensities, suggest that the slight differences in the energy per photon between the two wavelengths may be accessing different excited states in the molecule. However, these differences in the spectra do not appear to be easily generalized. Sinapinic acid, a molecule similar in structure to CHCA (both are cinnamic acid derivatives), exhibit different trends when their MALDI background spectra are reviewed.

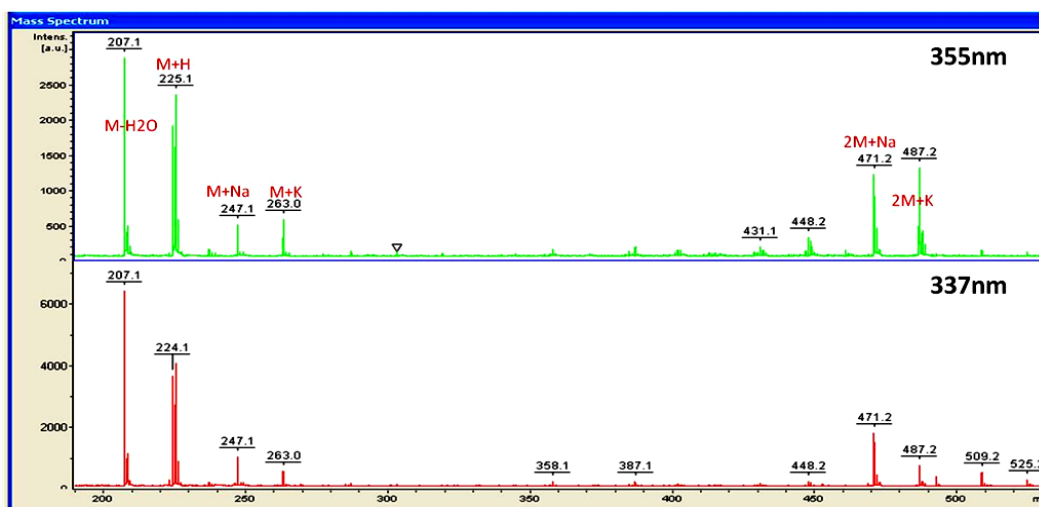


Figure 5.11: Positive polarity mass spectra of CHCA at both 337 and 355nm wavelengths. The table below the spectra illustrate the relative peak area differences for the same matrix compound that the two wavelengths

**Table 5.8: Table showing the ratios of various SA background matrix ion peaks compared between 337nm and 355nm wavelength incident light.**

<b>Sinapinic acid</b>	<b>Peak area ratio</b>			
	<b>Wavelength</b>	<b>[M-H<sub>2</sub>O]<sup>+</sup>/[M+H]<sup>+</sup></b>	<b>[M+Na]<sup>+</sup>/[M+H]<sup>+</sup></b>	<b>[M+Na]<sup>+</sup>/[M+K]<sup>+</sup></b>
<b>355</b>	<b>1.30</b>	<b>0.20</b>	<b>0.80</b>	<b>0.92</b>
<b>337</b>	<b>2.02</b>	<b>0.31</b>	<b>1.88</b>	<b>2.38</b>

Figure 5.11 shows that the wavelength used has little effect on the amount of sodium cationized matrix ions observed in the sinapinic acid mass spectra. The peak area ratios for the cationized matrix ions and other matrix ions are summarized in

Table 5.8. There is an increase in potassium adduction as was observed with CHCA. Although there is also an increase in the intensity of the ion associated with a loss of water, the difference is not as dramatic as was seen in the CHCA background spectra. These spectra are presented as both an illustration of the clear differences that exist in the background spectra at 337 and 355nm and the overall differences in mass spectra for two similar MALDI matrix compounds.

The small set of data presented here corroborates the data obtained from the M/A plots. The increase in ion signal along with an increase in cationization at 355nm is not localized to the analyte molecules. The same increase in cationization is observed in the matrix spectra. This re-enforces that the ionization reactions occurring in the expanding plume are common to both matrix and analyte. At 355nm some mechanism is driving an increase in cationization of the matrix molecules that is in turn being seen in the interactions with the analyte in the expanding plume.



## Conclusions

The data presented here have demonstrated that many common MALDI matrix compounds have comparable absorbance at 337 and 355nm in the solid state. This is significant in that predictions made about the utility of new matrix compounds at these wavelengths based on solution phase UV-visible absorption data alone may not be useful. It has also been shown for the first time that the signal for a model analyte and common matrix, CHCA, is greater at 355nm as compared to 337nm. This supports the findings by Kinsel and Zhang as mentioned previously. There is a clear dependence on MALDI signal for the wavelength used for desorption. Experiments using a QCM to quantitatively determine the amount of matrix material desorbed at each wavelength have shown that ~45% more matrix is desorbed per laser shot at 355nm as compared to 337nm. Increased material in the expanding plume may account for the increase in ion signals observed at 355nm. The data also suggests that the degree of cationization of the analyte is influenced by the choice of wavelength. Increased cationization has also been shown to occur in the matrix spectra as well and these data could provide insight into the mechanisms of analyte ionization. Further studies will need to be conducted to separate the desorption and ionization steps in MALDI to further characterize the differences between the two most commonly used wavelengths for desorption in commercial MALDI instruments.

## References

1. Stumpf, W. E., Drugs in the brain - cellular imaging with receptor microscopic autoradiography. *Progress in Histochemistry and Cytochemistry* 47 (1), 1-26.
2. Oppenheimer, S. R.; Drexler, D. M., Tissue analysis by imaging MS. *Bioanalysis* 4 (1), 95-112.

3. Bakry, R.; Rainer, M.; Huck, C. W.; Bonn, G. K., Protein profiling for cancer biomarker discovery using matrix-assisted laser desorption/ionization time-of-flight mass spectrometry and infrared imaging: A review. *Analytica Chimica Acta* 690 (1), 26-34.
4. Zhang, J.; Kinsel, G. R., Quantification of Protein-Polymer Interactions by Matrix-Assisted Laser Desorption/Ionization Mass Spectrometry. *Langmuir* 2002, 18 (11), 4444-4448.
5. Tanaka, K.; Waki, H.; Ido, Y.; Akita, S.; Yoshida, Y.; Yoshida, T.; Matsuo, T., Protein and polymer analyses up to  $m/z$  100 000 by laser ionization time-of-flight mass spectrometry. *Rapid Communications in Mass Spectrometry* 1988, 2 (8), 151-153.
6. Karas, M.; Hillenkamp, F., Laser desorption ionization of proteins with molecular masses exceeding 10,000 daltons. *Analytical Chemistry*, 1988; Vol. 60, pp 2299-2301.
7. Dreisewerd, K., The desorption process in MALDI. *Chemical Reviews* 2003, 103 (2), 395-425.
8. Westmacott, G.; Ens, W.; Hillenkamp, F.; Dreisewerd, K.; Schurenberg, M., The influence of laser fluence on ion yield in matrix-assisted laser desorption ionization mass spectrometry. *International Journal of Mass Spectrometry* 2002, 221 (1), 67-81.
9. Dreisewerd, K.; Schurenberg, M.; Karas, M.; Hillenkamp, F., Influence of the laser intensity and spot size on the desorption of molecules and ions in matrix-assisted laser desorption/ionization with a uniform beam profile. *International Journal of Mass Spectrometry and Ion Processes* 1995, 141 (2), 127-148.
10. Chou, C.-W.; Nelson, R. W.; Williams, P., Dependence of the ejection velocities of laser-ablated ions on the laser wavelength and fluence. *European Journal of Mass Spectrometry* 2009, 15, 305-314.
11. Hillenkamp, F.; Karas, M.; Holtkamp, D.; Klusener, P., Energy deposition in ultraviolet laser desorption mass spectrometry of biomolecules. *International Journal of Mass Spectrometry and Ion Processes* 1986, 69 (3), 265-276.
12. Kinsel, G. R.; Knochenmuss, R.; Setz, P.; Land, C. M.; Goh, S. K.; Archibong, E. F.; Hardesty, J. H.; Marynick, D. S., Ionization energy reductions in small 2,5-dihydroxybenzoic acid-proline clusters. *Journal of Mass Spectrometry* 2002, 37 (11), 1131-1140.
13. Land, C. M.; Kinsel, G. R., The mechanism of matrix to analyte proton transfer in clusters of 2,5-dihydroxybenzoic acid and the tripeptide VPL. *Journal of the American Society for Mass Spectrometry* 2001, 12 (6), 726-731.
14. Keller, B. O.; Li, L., Discerning matrix-cluster peaks in matrix-assisted laser desorption/ionization time-of-flight mass spectra of dilute peptide mixtures. *Journal of the American Society for Mass Spectrometry* 2000, 11, 88-93.
15. Knochenmuss, R., Ion formation mechanisms in UV-MALDI. *Analyst* 2006, 131 (9), 966-986.
16. Karas, M.; Gluckmann, M.; Schafer, J., Ionization in matrix-assisted laser desorption/ionization: singly charged molecular ions are the lucky survivors. *Journal of Mass Spectrometry* 2000, 35 (1), 1-12.
17. Karas, M.; Kruger, R., Ion Formation in MALDI: The Cluster Ionization Mechanism. *Chemical Reviews* 2003, 103 (2), 427-440.
18. Kruger, R.; Pfenninger, A.; Fournier, I.; Gluckmann, M.; Karas, M., Analyte incorporation and ionization in matrix-assisted laser desorption/ionization visualized by pH indicator molecular probes. *Analytical Chemistry* 2001, 73 (24), 5812-5821.
19. Knochenmuss, R.; Zenobi, R., MALDI ionization: The role of in-plume processes. *Chemical reviews* 2003, 103 (2), 441-452.

20. Zhang, J.; Knochenmuss, R.; Stevenson, E.; Zenobi, R., The gas-phase sodium basicities of common matrix-assisted laser desorption/ionization matrices. *International Journal of Mass Spectrometry* 2002, *213*, 237-250.
21. Jaskolla, T. W.; Karas, M., Compelling evidence for lucky survivor and gas phase protonation: the unified MALDI analyte protonation mechanism. *Journal of the American Society of Mass Spectrometry* 2011, *22*, 976-988.
22. Erb, W. J.; Owens, K. G., Development of a dual-spray electrospray deposition system for matrix-assisted laser desorption/ionization time-of-flight mass spectrometry. *Rapid Communications in Mass Spectrometry* 2008, *22*, 1168-1174.
23. Breuker, K.; Knochenmuss, R.; Zhang, J.; Stortelder, A.; Zenobi, R., Thermodynamic control of final ion distributions in MALDI: in-plume proton transfer reactions. *International Journal of Mass Spectrometry* 2003, *226* (1), 211-222.
24. Zenobi, R.; Knochenmuss, R., Ion formation in MALDI mass spectrometry. *Mass Spectrometry Reviews* 1999, *17*, 337-366.
25. Knochenmuss, R., Photoionization pathways and free electrons in UV-MALDI. *Analytical Chemistry* 2004, *76* (11), 3179-3184.
26. Karas, M.; Bachmann, D.; Hillenkamp, F., Influence of the wavelength in high-irradiance ultraviolet laser desorption mass spectrometry of organic molecules. *Analytical Chemistry* 1985, *57* (14), 2935-2939.
27. Allwood, D. A.; Dreyfus, R. W.; Perera, I. K.; Dyer, P. E., UV optical absorption of matrices used for matrix-assisted laser desorption/ionization. *Rapid Communications in Mass Spectrometry* 1996, *10* (13), 1575-1578.
28. Niu, S.; Zhang, W.; Chait, B., Direct comparison of infrared and ultraviolet wavelength matrix-assisted laser desorption/ ionization mass spectrometry of proteins. *Journal of the American Society for Mass Spectrometry* 1998, *9* (1), 1-7.
29. Knochenmuss, R., A quantitative model of ultraviolet matrix-assisted laser desorption. *Analytical Chemistry* 2003, *75* (10), 2199-2207.
30. Hu, X. K.; Lacey, D.; Li, J.; Yang, C.; Loboda, A. V.; Lipson, R. H., Visible wavelength MALDI using Coumarin laser dyes. *International Journal of Mass Spectrometry* 2008, *278* (1), 69-74.
31. Lee Chuin Chen; Daiki Asakawa; Hirokazu Hori; Kenzo Hiraoka, Matrix-assisted laser desorption/ionization mass spectrometry using a visible laser. *Rapid Communications in Mass Spectrometry* 2007, *21* (24), 4129-4134.
32. Little, M. W.; Laboy, J.; Murray, K. K., Wavelength Dependence of Soft Infrared Laser Desorption and Ionization. *Journal of Physical Chemistry C* 2007, *111* (3), 1412-1416.
33. Karas, M.; Bachmann, D.; Hillenkamp, F., Influence of the Wavelength in High-Irradiance Ultraviolet-Laser Desorption Mass-Spectrometry of Organic-Molecules. *Analytical Chemistry* 1985, *57* (14), 2935-2939.
34. Kampmeier, J.; Dreisewerd, K.; Schürenberg, M.; Strupat, K., Investigations of 2,5-DHB and succinic acid as matrices for IR and UV MALDI. Part: I UV and IR laser ablation in the MALDI process. *International Journal of Mass Spectrometry and Ion Processes* 1997, *169-170*, 31-41.
35. Cramer, R.; Hillenkamp, F.; Haglund, R. F., Infrared Matrix-Assisted Laser Desorption and Ionization by Using a Tunable Mid-Infrared Free-Electron Laser. *Journal of the American Society for Mass Spectrometry* 1996, *7* (12), 1187-1193.
36. Horneffer, V.; Dreisewerd, K.; Lämdeemann, H. C.; Hillenkamp, F.; Lange, M.; Strupat, K., Is the incorporation of analytes into matrix crystals a prerequisite for matrix-assisted laser desorption/ionization mass spectrometry? A study of five positional isomers of dihydroxybenzoic acid. *International Journal of Mass Spectrometry* 1999, *185-187*, 859-870.

37. Knochenmuss, R.; Stortelder, A.; Breuker, K.; Zenobi, R., Secondary ion-molecule reactions in matrix-assisted laser desorption. *Journal of Mass Spectrometry* 2000, 35 (11), 1237-1245.
38. Westman, A.; Demirev, P.; Huth-Fehre, T.; Bielawski, J.; Sundqvist, B. U. R., Sample exposure effects in matrix-assisted laser desorption/ionization mass spectrometry of large biomolecules. *International Journal of Mass Spectrometry and Ion Processes* 1994, 130 (12), 107-115.
39. Knochenmuss, R.; Zhigilei, L. V., Molecular dynamics model of ultraviolet matrix-assisted laser desorption/ionization including ionization processes. *Journal of Physical Chemistry B* 2005, 109 (48), 22947-22957.
40. Quist, A. P.; Huthfehre, T.; Sundqvist, B. U. R., Total yield measurements in matrix-assisted laser-desorption using a quartz-crystal microbalance. *Rapid Communications in Mass Spectrometry* 1994, 8 (2), 149-154.
41. Chen, Y.; Vertes, A., Pumping rate and surface morphology dependence of ionization processes in matrix-assisted laser desorption ionization. *Journal of Physical Chemistry a* 2003, 107 (46), 9754-9761.
42. Chavez-Eng, C. M. Quantitative aspects of matrix-assisted laser desorption/ionization using electrospray deposition. PhD, Drexel University, Philadelphia, 2002.
43. Ehring, H.; Sundqvist, B. U. R., Studies of the MALDI process by luminescence spectroscopy. John Wiley & Sons, Ltd.: 1995; Vol. 30, pp 1303-1310.
44. Gluckmann, M.; Pfenninger, A.; Kruger, R.; Thierolf, M.; Karas, M.; Horneffer, V.; Hillenkamp, F.; Strupat, K., Mechanisms in MALDI analysis: surface interaction or incorporation of analytes? *International Journal of Mass Spectrometry* 2001, 210 (1-3), 121-132.
45. N. Medina; T. Huth-Fehre; A. Westman; B. U. R. Sundqvist, Matrix-assisted laser desorption: Dependence of the threshold fluence on analyte concentration. *Organic Mass Spectrometry* 1994, 29 (4), 207-209.
46. Hensel, R. R.; King, R. C.; Owens, K. G., Electrospray sample preparation for improved quantitation in matrix-assisted laser desorption/ionization time-of-flight mass spectrometry. *Rapid Communications in Mass Spectrometry* 1997, 11, 1785-1793.
47. Erb, W. J. Exploration of the fundamentals of matrix assisted laser desorption/ionization time-of-flight mass spectrometry. PhD thesis, Drexel University, Philadelphia, 2007.
48. Kinsel, G. R.; Lindner, J.; Grotemeyer, J.; Schlag, E. W., Absorption effects in laser desorption of neutral organic molecules. *The Journal of Physical Chemistry* 1991, 95 (20), 7824-7830.
49. Ueno-Noto, K.; Marynick, D. S., A comparative computational study of matrix-peptide interactions in MALDI mass spectrometry: the interaction of four tripeptides with the MALDI matrices 2,5-dihydroxybenzoic acid, alpha-cyano-4-hydroxy-cinnamic acid and 3,5-dihydroxybenzoic acid. *Molecular Physics* 2009, 107 (8-12), 777-788.
50. Nangia, S.; Garrison, B. J., Molecular dynamics simulations of matrix assisted laser desorption ionization: Matrix-analyte interactions. *Nuclear Instruments and Methods in Physics Research Section B: Beam Interactions with Materials and Atoms* 269 (14), 1744-1747.

## Chapter 6. Investigation into the Effect of Solvent Composition on MALDI Signal

### Introduction

In most MALDI experiments the prerequisite for sample analysis is that the matrix and analyte must be homogeneously incorporated into a solid. Typically this is accomplished by allowing solutions of the matrix and analyte to evaporate leaving behind crystalline or amorphous solids. The aim of this chapter is to investigate if the identity of the solvent has an effect on the ions generated in the MALDI experiment.

As discussed in chapter 5, one of the prevailing theories for primary ionization in MALDI involves photoexcitation and energy pooling in the solid matrix material<sup>1</sup>. This process is believed to proceed by the interaction of excited singlet state ( $S_1$ ) matrix molecules<sup>1</sup>. Previous work in our group explored this by demonstrating that fluorescence quenching by halide ions occurs in the expanding MALDI plume<sup>2</sup>. The halide ions interact by way of orbital overlap with the excited state matrix molecules in the plume. When this orbital overlap occurs, the singlet state matrix molecules are converted into the triplet state ( $T_1$ ). Molecules in the  $T_1$  state reside at lower energy than those in the  $S_1$  state, and they are also more likely to undergo vibrational relaxation during collision events reducing them to the lowest vibrational level in the  $T_1$  state. The lower energy  $T_1$  state will require more energy in order to create a primary matrix ion. The probability of direct three-photon absorption leading to ionized matrix molecules has been suggested to be low<sup>1</sup>, therefore the absorption of four or more photons that may be required of the matrix molecules residing in the  $T_1$  state will be even less likely. Therefore, an increase in the population of  $T_1$  matrix molecules in the plume could result in a decrease in the observed MALDI signal, as there will be less ionized matrix molecules in the expanding plume. Still  $T_1$

molecules can undergo energy pooling, however, the mechanism is different from that of the  $S_1$  molecules. Triplet state molecules are believed to interact by Dexter energy transfer, which requires a high degree of orbital overlap to occur. Due to this specificity Dexter energy transfer falls off quickly, as a function of  $e^{-2r/L}$ , where  $r$  is the distance between two molecules and  $L$  is the sum of the Van der Waals radii of the donor and the acceptor<sup>3</sup>. By comparison, molecules in the  $S_1$  state undergo Forster energy transfer, involving dipole-dipole interactions<sup>4</sup>. These energy transfers fall off as a function of  $1/r^6$ , making them more likely in the expanding plume. The steep fall off in the probability of Dexter energy transfer with intermolecular distance suggests that a greater number of matrix molecules residing in the triplet state will reduce the total number of ionized matrix molecules produced in the plume. A decrease in the number of ionized molecules available for analyte ionization would lead to a decrease in the MALDI ion signal. This was the case as the presence of chloride, bromide or iodide anions were shown to decrease the ion signal observed as their concentrations were increased<sup>2</sup>. Stern-Volmer plots of the titration of the halide salts into the matrix and analyte solutions were consistent with the excited state quenching. Some of the plots from these experiments are shown in Figure 6.1. These data provided good evidence for the pooling hypothesis.

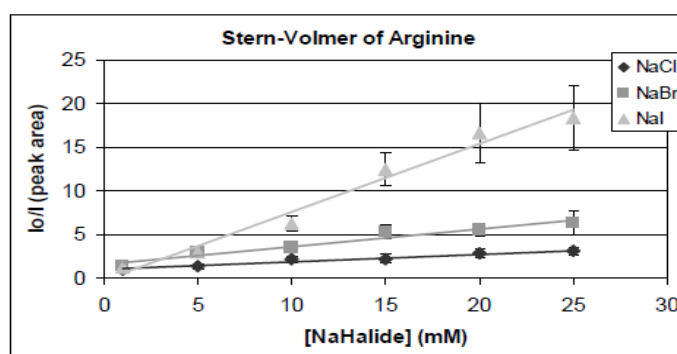


Figure 6.1: Stern-Volmer plots of arginine with NaCl, NaBr, and NaI from 1-25mM concentrations. Error bars are calculated for the 95% confidence intervals. Reproduced from Holcomb<sup>2</sup>.

Salts are particularly important in MALDI sample preparation techniques where crystallization of the matrix and analyte is performed rapidly or where amorphous particles of the mixture are deposited, as is the case with ESD. Samples prepared by the dried drop technique are believed to exclude salts from the crystals that are formed and consequently less cationization of the analyte is observed<sup>5</sup>.

All sample preparation techniques that rely on solvent evaporation to produce solid matrix and analyte crystals or particles will likely also incorporate some amount of the solvent into the particles or crystals. The extent of solvent incorporation for some matrix and analyte combinations has been explored by Kruger et al<sup>6</sup>. They measured solvent incorporation using proton NMR, and showed up to ~3% incorporation by mass in samples prepared by the dried drop method. It is important to note that this value will likely vary depending on the physio-chemical properties of the solvent and the sample preparation technique used. In the same work they provided evidence that the ionic interactions of the MALDI matrix and dye molecules in solution appear to be conserved upon crystallization of the solution. Based on these findings they hypothesized that ion pairs of the dye molecules and the matrix molecules in solution are still present in the solid material. The ion pairs may be bridged or stabilized by the residual solvent molecules in the dried samples. Though this evidence would seem to strongly support the theory of preformed ions as a primary ionization mechanism it could have important consequences for the pooling theory as well.

Residual solvents interacting as bridging partners of ion pairs may affect the local environment of matrix molecules in the solid sample. The solvent molecules can interact with the matrix to shift the excitation wavelength of the matrix and possibly affect the pooling by stabilizing or de-stabilizing the excited state dipole. The local environment in the dried samples

may affect the energy state of the excited matrix molecules similar to the halide anions as shown in Figure 6.1. These factors could singly or in combination lead to a decrease in the number of excited state matrix molecules available for energy pooling. A decrease in the number of ionized matrix molecules available for reactions with the analyte in the expanding plume will decrease the observed signal in the MALDI experiment. The studies presented previously<sup>2, 6</sup> and also those presented herein are not able to resolve the two proposed primary ionization mechanisms in their design. The decrease in ionization observed by the addition of halide ions into solid MALDI samples and similarly the evidence for ion pair retention in crystallized MALDI samples cannot provide specific evidence for primary ionization in light of the predominance of secondary ionization reactions occurring in the expanding plume<sup>1, 7-9</sup>. Even proponents of the cluster ionization mechanism have accepted the effect of secondary plume reactions leading to the observed analyte signals in MALDI<sup>9</sup>.

To explore the effects of residual trapped solvent on MALDI ionization, experiments using solution-phase fluorescence measurements of 2,5-DHB in three solvents were made. The solvents chosen were MeOH, MeCN and chloroform. MeOH is a common solvent used in our group for sample preparation using ESD. Chloroform was chosen to determine if fluorescent quenching would be observed due to the covalently bonded chlorine atoms of the solvent similar to that observed by the halide ions previously studied<sup>2</sup>. Finally, MeCN was chosen due to the fact that dried drop sample preparation is generally carried out in the literature using MeCN:water mixtures containing volatile organic acids such as trifluoroacetic acid. This experiment was carried out using ~6ppm solutions of 2,5-DHB in each of the three solvents. The solutions were excited at 337nm and the emission was measured at 455nm. The results of this experiment are shown in Figure 6.2.



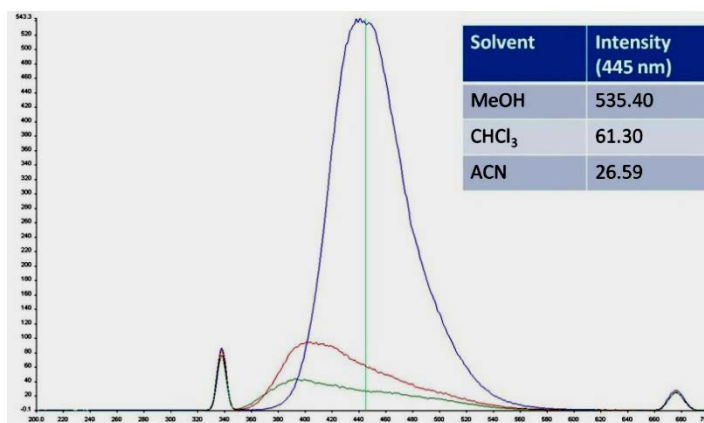


**Figure 6.2:** The fluorescence emission spectra of 2,5-DHB when excited at 337nm. 6ppm solutions of 2,5-DHB were made in pure MeOH, MeCN and Chloroform. The intensity of the emission at 445nm is given in the tabular inset. These spectra were collected as part of the undergraduate research of Francisco Guevara.

Figure 6.2 shows that the fluorescence emission of 2,5-DHB is significantly decreased in the presence of both MeCN and chloroform. In light of the previous studies in our group, it was expected that the MALDI signal for solutions prepared in MeCN and chloroform would lead to a decrease in analyte ion signal. If this proved to be the case then it could add further evidence for the energy pooling ionization mechanism. Experiments will be detailed in which the solvents presented in Figure 6.2 are used to prepare MALDI samples via ESD. The samples will be analyzed to determine if the dissolution solvent has an impact in the number of analyte ions observed in the measured MALDI spectra.

## Experimental

Specific sample preparation details pertaining to the experiments discussed in this chapter will be presented here. Detailed information regarding the instrumentation used for these studies can be found in Chapter 2.

Solutions containing 0.02M 2,5-DHB and Ang I (M/A = 2500:1) were prepared in various solvent systems using reagent grade MeOH, MeCN and chloroform obtained from Sigma-

Aldrich. Where mixtures of these solvents were made they were prepared volumetrically in the percentages required. All MALDI samples were prepared using the controlled electrospray deposition technique previously described in this thesis. The sample solutions were sprayed from a height of 20 mm and a flow-rate of 2.0  $\mu$ L/min for 2 minutes. All solutions were sprayed in triplicate and the data presented are averages of six individual accumulations of 500 summed shots for each of the three sprays. The sprayed samples were analyzed using the Bruker Autoflex III instrument and FlexAnalysis software described in Chapter 2.

### ***Solubility Measurements***

The solubility of 2,5-DHB was determined by preparing a saturated solution of 2,5 DHB in 10mL of each of the solvent combinations. Solid was added to the solvent until crystals remained after mixing and sonication. The solutions were then held at 45°C for 30 minutes, during this time if the matrix visually appeared to completely dissolve additional matrix was added to the vial until solids remained. After at least 30 minutes at 45°C the vials were transferred to a 25°C water bath for an additional 30 minutes. A 1.0mL aliquot of the supernatant was placed into a pre-massed 1.5mL micro-centrifuge tube. The tubes were placed into a Savant Speed-Vac and allowed to dry completely. The dry powder in the tubes was then massed and the amount of dissolved solid was calculated.

## **Results and Discussion**

Prior to mass spectral analysis the solubility of DHB was measured in pure solvents and several mixtures of the solvents MeOH, MeCN and chloroform. The measurements were performed as described in the experimental chapter by an undergraduate student in our research group, Francisco Guevara. The results of these studies are presented in Table 6.1. The measurements demonstrated that the solubility of DHB was greatest in pure MeOH.

Interestingly, the solubility of DHB in mixtures of MeOH and MeCN do not follow a linear trend. DHB in a 1:1 mixture of MeOH and MeCN had a solubility of 246 mg/mL, which is roughly 85% of the solubility in pure MeOH. Further in a mixture of 19% MeOH in MeCN (the azeotropic composition) the solubility of DHB is more than half of that in pure MeOH. This large increase in solubility when MeOH is a component of the solvent will be further discussed in context of the experimental results later in this chapter.

**Table 6.1: Solubility values for 2,5-DHB in MeOH, MeCN, Chloroform and mixtures. Values for the % saturation at the relevant spraying concentrations are given in the last column. The \* denotes the azeotrope if it exists for the solvent mixtures. This data was produced by Francisco Guevara.**

Solvent	Solubility (mg/mL)	% Saturation at 0.02M
Methanol	411	0.7
Acetonitrile	92	3.3
Chloroform	1.3	N/A
Methanol:Acetonitrile (19:81)*	246	2.0
Methanol:Acetonitrile (1:1)	350	0.9
Methanol:Chloroform (13:87)*	63	7.9
Methanol:Chloroform (1:1)	184	2.7

Initial MALDI response experiments were performed using Ang I/DHB samples dissolved in pure MeOH, pure MeCN, a 1:1 mixture of MeOH:MeCN and a 1:1 mixture of MeOH:chloroform. It was our intent to spray a sample prepared in pure chloroform, however, the solubility of DHB in chloroform is poor (Table 6.1) and the resultant mixture was visibly clouded, therefore only a 1:1 mixture with MeOH was studied. The mixture of MeCN and MeOH was included as a pseudo control for the chloroform preparation. If MALDI analyte signal suppression was observed for the pure MeCN preparation it would be expected that some

similar degree of suppression would occur in a mixture with a non-quenching solvent. In this way any decrease in signal for the chloroform:MeOH mixture could be similarly rationalized. The spraying conditions for the samples were held constant as were the MALDI instrument parameters (i.e., laser spot size and energy) for all samples. Figure 6.3 shows the results of the MALDI experiments.

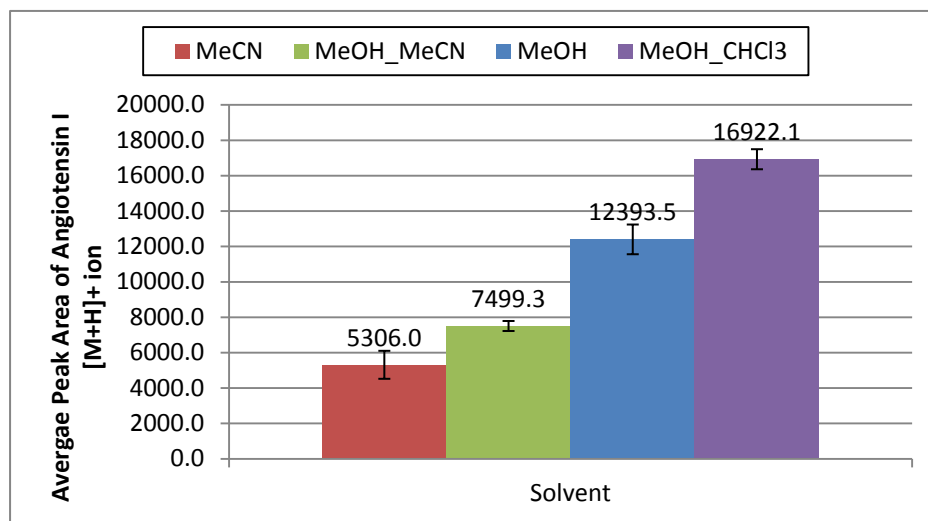


**Figure 6.3:** Plot of the average peak area for Angiotensin I molecular ion as measured by MALDI using a controlled ESD sample preparation technique. Solutions of 2,5-DHB and Angiotensin I were prepared in four different solvent compositions for spraying denoted in the legend.

There are two distinct results presented in Figure 6.3. First, there is a significant decrease in analyte signal as a function of MeCN content in the spraying solution. Second, samples prepared using chloroform did not decrease the observed analyte ion signal as was predicted from the solution fluorescence data<sup>2</sup>. This second observation is puzzling in the context of the fluorescence data, which would suggest that like the halide ions and MeCN a decreased analyte signal should be seen if residual chloroform was present in the dried particles. Possible reasons for the increased signal when chloroform is used will be discussed first.

Chloroform is more volatile than MeOH, and as such will preferentially evaporate from the droplets as they are transported from the electrospray needle to the metal surface and therefore may not be present in the final dried particle to a large extent. Note that the extent of evaporation from the droplets will be affected by atmosphere the sample is sprayed in, particularly the identity of the chamber gas, temperature and relative humidity. It is also expected that MeOH would have a greater interaction with the matrix as it can act as both a proton donor and acceptor, which would likely solvate the matrix more efficiently than the chloroform. As chloroform is lost from the droplet, the solubility of the matrix will increase as DHB is more soluble in MeOH (Table 6.1). If this occurs the increase in solubility would delay the onset of nucleation of the matrix in the droplet as it dries. Investigations into the morphology of spray dried particles can provide insight into the morphology differences that may be expected if this hypothesis were true. It has been demonstrated that air dried particles containing a solute suspended in a solvent tend to form spherical crusts<sup>10</sup>. This is due to the migration of the solute to the edges of the droplet. The rate at which this happens depends on the size of the droplet, the concentration of the solute and the partition coefficient of the solute(s) in the bulk droplet volume as compared to the charged outer rim<sup>11, 12</sup>. Once this crust has formed its integrity is also determined by the same parameters<sup>13</sup>. A solute of higher solubility in a given solvent or a decrease in solute concentration will lead to production of a denser particle and will be less likely to undergo shell collapse. This phenomenon has been shown to occur in electrosprayed droplets as well as aerosol particles as described by Leong<sup>14</sup>. If this concept is extended to our sprayed solutions, it may be that the solutions sprayed containing the mixture of MeOH and chloroform as solvent undergoes more gradual nucleation and therefore form denser and preferentially more spherical particles, which would be in contrast to the particles formed from the solution sprayed from pure MeOH. This effect would be similar to the differences shown in

the spraying height studies described in Chapter 4. The morphological differences shown in those studies appear to correlate to analyte signal. Sprays made at lower heights produced cracked shells, while those made from higher spraying distances appeared to produce intact spheres of solid. It is expected that an intact sphere would lead to more efficient desorption of material from the surface. If the spheres are cracked there are more solid boundaries and the processes of exciton diffusion or pooling will be hindered to a greater extent. A similar phenomenon has been shown to occur in organic crystals, where exciton mobility is greater for crystals with fewer defects<sup>15</sup>. This would suggest that intact particles should pool more efficiently, creating a greater number of primary ions that may result in the observation of more analyte signal. This hypothesis also suggests why the solutions containing chloroform produced the highest analyte signals.

Returning to the first observation from Figure 6.3, the presence of MeCN in the sample solution does impact the analyte signal. Solutions containing MeCN alone as a solvent generated the lowest analyte signal as compared to solutions containing MeOH or a 1:1 mixture of MeOH:MeCN. It also appears that the addition of 50% MeCN by volume decreased the analyte signal by approximately half as compared to pure MeOH. To further investigate this phenomenon, MeCN was titrated into MeOH solutions containing DHB and Ang I. The samples were then sprayed and analyzed in the MALDI instrument.

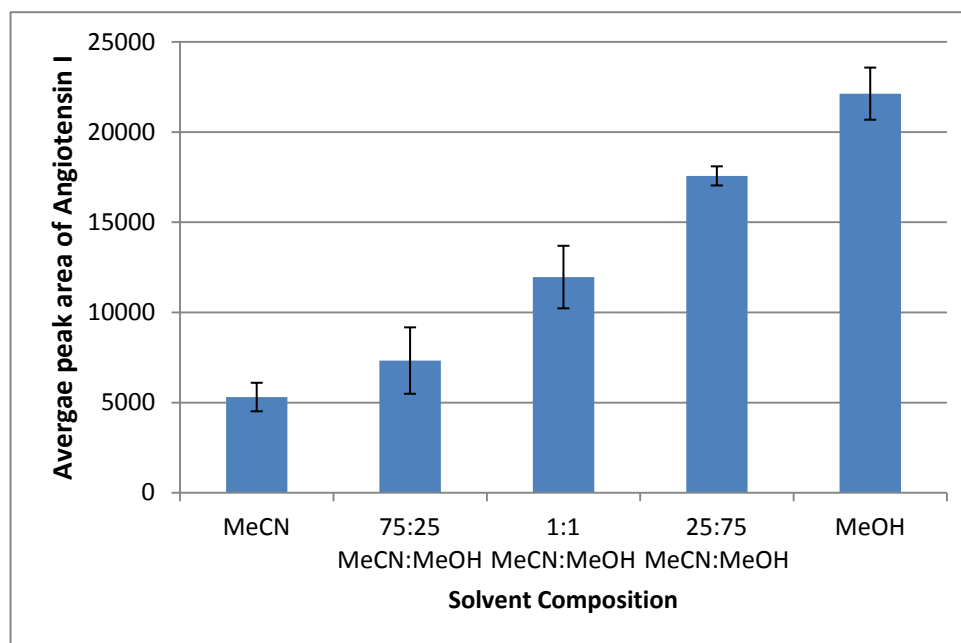


**Figure 6.4:** Plot of the average peak area of Angiotensin I molecular ion from MALDI samples prepared from different solvent conditions. The samples were prepared by controlled ESD.

Figure 6.4 shows the results from the titration of MeCN into MeOH and its effect on the analyte ion signal of Ang I. This experiment confirms the analyte signal dependence on the volume percent MeCN in ESD prepared MALDI samples. The solubility of DHB is lower in pure MeCN than in MeOH, however, DHB in a mixture of 1:1 MeOH:MeCN has a solubility that is similar to that of pure MeOH (Table 6.1). Still the solubility and nucleation of the DHB and analyte may affect the amount of trapped solvent in the dried particles and therefore may be of importance to the observed results. Crystallization rates have been shown to impact the inclusion of trapped solvents<sup>16</sup>. As the drying processes in ESD are relatively fast for the droplets it can be expected that some residual solvent will be trapped in the droplet. The presence and identity of the trapped solvent in the dried particles could impact the observed analyte ion signal. MeCN has been shown to quench DHB fluorescence in solution and therefore it is expected that if there is residual MeCN trapped in the solid particles being irradiated there is

likely to be an interaction between the matrix and the solvent in the expanding MALDI plume. The quenching of DHB via triplet state conversion has been shown to decrease analyte ionization and could explain the results presented in Figure 6.4. For this to be true the data should be able to be plotted via the Stern-Volmer equation. Figure 6.5 is a Stern-Volmer plot of the peak areas as compared to the volume percent of MeCN in the sample preparation solution.

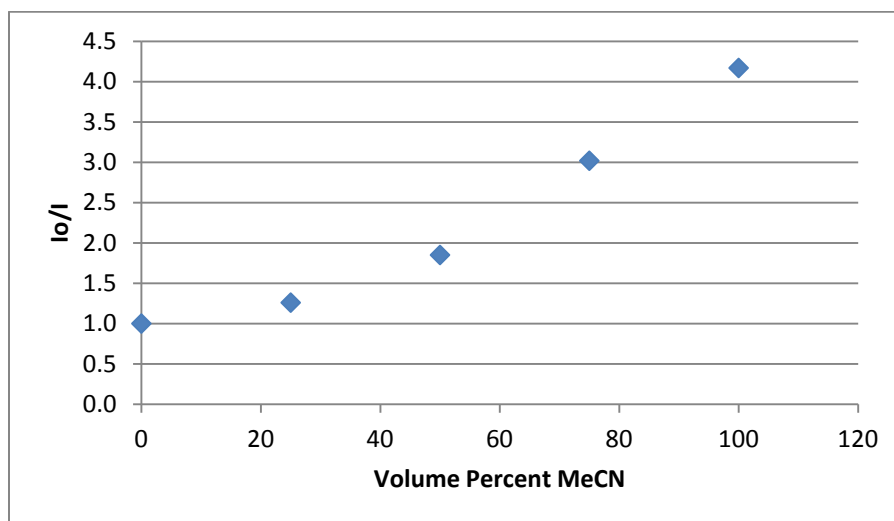


**Figure 6.5: Stern-Volmer plot of Angiotensin I peak area as a function of volume percent MeCN in the sample preparation.**

In a Stern-Volmer plot the intercept for a line drawn through the data should be 1. A plot of our data demonstrates that this is not the case and that the data are clearly not linear. A linear decrease of the analyte signal as quencher concentration increases would be expected if this were a simple Stern-Volmer interaction. However, the lack of linearity in Figure 6.5 is puzzling. A possible explanation for why the data does not fit linearly in the Stern-Volmer plot is that the relative amount of trapped solvent in the particles is likely to be small. In MALDI samples the matrix is used in large molar excess. Small amounts of solvent trapped in the particles may not have a high probability of interaction with the excited matrix molecules.



Thereby the quenching MeCN molecules may have hindered access to the excited state matrix molecules leading to the deviation from linearity that is observed in Figure 6.5<sup>17</sup>. Another cause for the deviation from linearity could arise from a competitive process in the plume other than triplet state quenching<sup>18, 19</sup>. The singlet state energy pooling of the matrix molecules will be a competitive process in the plume. The large molar excess of matrix molecules may favor the singlet state pooling process and thereby mask the effect of the MeCN quenching. Again it should be noted that these quenching measurements are being made indirectly by measuring the analyte ion signal as a surrogate for the interaction of the excited state matrix molecules and MeCN. There are other steps in the MALDI process that will affect the amount of ions observed, most notably the process of desorption. Preliminary evidence of the possible effect on analyte signal of the dried particle morphology has been presented in Chapter 4 and further discussed in this chapter. The large solubility difference of DHB in MeOH and MeCN and its affect on the particle deposited during ESD cannot be ignored in the explanation of the data in Figure 6.4.

Note that the azeotrope for MeCN and MeOH is at a ratio of 19:81 MeOH:MeCN<sup>20</sup> As MeOH is more volatile than MeCN it will be preferentially lost in the droplet until the azeotrope is reached at which point the two solvents will evaporate from the droplet together. As this occurs the droplet will become MeCN rich and the solubility of DHB will decrease. This may drive more rapid crystallization in the drying droplets of the matrix. An increased crystallization rate may impact the amount of solvent trapped in the dried particles and the particle morphology. A decrease in solubility of DHB in the droplet would be expected to produce less uniform cracked spherical particles on the surface. This would be in direct contrast to the discussion for the chloroform and MeOH sample discussed above. The less uniform particles may result in a decrease in desorption as the energy from the laser pulse cannot be effectively transported

across these types of particles. A decrease in material desorption would also lead to a decrease in the number of matrix and analyte ions in the plume for each laser pulse. This could lead to the observed analyte signal decrease shown in Figure 6.4.

A quenching mechanism cannot be confirmed from the data presented. The slope of the Stern-Volmer plot represents the bi-molecular interaction between the quenching substance and the substance being quenched. In these experiments we measure the result of more than one molecular interaction and use the outcome to infer singlet state quenching of the excited state matrix molecules. For an analyte ion to be observed by the detector it must be derived from the sum interactions of desorption from the surface followed by interaction with an ionized matrix molecule in the expanding plume. The results demonstrate that dissolution solvents, particularly MeCN affect the resultant analyte ion signal in MALDI for samples prepared by ESD.

## Conclusions

It has been demonstrated that analyte signal differences are observed for samples prepared by electrospray deposition from different solvents using DHB as the MALDI matrix. The initial motivation of this experiment was to determine if solvents that had been shown to quench the solution-phase fluorescence of DHB would also act as analyte signal quenchers in MALDI. The data presented suggest that there is an increase in analyte signal when a solution containing 50% chloroform is used to spray MALDI samples. This may not be a consequence of the molecular interaction as there may be little chloroform left in the dried droplet. It has therefore been hypothesized that the observed signal increase is likely a function of the droplet drying process. This explanation is also consistent with data presented in Chapter 5 and could be further demonstrated by imaging the samples sprayed from the different solutions using SEM.

It has also been shown that the amount of MeCN used in the dissolution solvent for MALDI sample preparation by ESD is inversely correlated to the analyte signal intensity. The exact mechanism of the signal suppression is confounded as it is difficult to separate the primary and secondary ionization pathways in MADLI. It may be that trapped MeCN molecules decrease energy pooling efficiency and impact secondary ionization mechanisms as well. Another explanation for the signal decrease when MeCN is used could be the morphology of the sprayed particles. Decreased solubility of DHB in MeCN may result in the production of less uniform cracked shell-like particles that are not desorbed as efficiently from the surface. Further work to determine the extent and the identity of the trapped solvents in the particles deposited and the resultant particle morphology when using ESD sample preparation will need to be done.

## References

1. Knochenmuss, R., Ion formation mechanisms in UV-MALDI. *Analyst* 2006, *131* (9), 966-986.
2. Holcomb, A. M. Investigation into the ionization mechanisms occurring in matrix assisted laser desorption ionization and factors affecting ion flight time in MALDI time-of-flight mass spectrometry. PhD, Drexel University, Philadelphia, 2009.
3. Olaya-Castro, A.; Scholes, G. D., Energy transfer from Forster-Dexter theory to quantum coherent light-harvesting. *Int. Rev. Phys. Chem.* *30* (1), 49-77.
4. Dow, J. C., Resonance Energy Transfer in Condensed Media from a Many Particle Viewpoint. *Phys. Rev.* 1968, (174).
5. Beavis, R. C.; Chait, B. T., Rapid, sensitive analysis of protein mixtures by mass-spectrometry. *Proceedings of the National Academy of Sciences of the United States of America* 1990, *87* (17), 6873-6877.
6. Kruger, R.; Pfenninger, A.; Fournier, I.; Gluckmann, M.; Karas, M., Analyte incorporation and ionization in matrix-assisted laser desorption/ionization visualized by pH indicator molecular probes. *Analytical Chemistry* 2001, *73* (24), 5812-5821.
7. Knochenmuss, R.; Zenobi, R., MALDI ionization: The role of in-plume processes. *Chemical reviews* 2003, *103* (2), 441-452.
8. Krüger, R.; Karas, M., Formation and fate of ion pairs during MALDI analysis: Anion adduct generation as an indicative tool to determine ionization processes. *Journal of the American Society for Mass Spectrometry* 2002, *13* (10), 1218-1226.

9. Jaskolla, T. W.; Karas, M., Compelling evidence for lucky survivor and gas phase protonation: the unified MALDI analyte protonation mechanism. *Journal of the American Society of Mass Spectrometry* 2011, 22, 976-988.
10. Leong, K. H., Morphology of aerosol-particles generated from the evaporation of solution drops. *Journal of Aerosol Science* 1981, 12 (5), 417-435.
11. Leong, K. H., Morphological control of particles generated from the evaporation of solution droplets - theoretical considerations. *Journal of Aerosol Science* 1987, 18 (5), 511-524.
12. Jorabchi, K.; Smith, L. M., Single Droplet Separations and Surface Partition Coefficient Measurements Using Laser Ablation Mass Spectrometry. *Analytical Chemistry* 2009, 81 (23), 9682-9688.
13. Leong, K. H., Morphological control of particles generated from the evaporation of solution droplets: Experiment. *Journal of Aerosol Science* 1987, 18 (5), 525-552.
14. Jeong, K. H.; Seo, J.; Yoon, H. J.; Shin, S. K., Focused Electrospray Deposition for Matrix-assisted Laser Desorption/Ionization Mass Spectrometry. *Bulletin of the Korean Chemical Society* 31 (8), 2293-2298.
15. Emelianova, E. V.; Athanasopoulos, S.; Silbey, R. J.; Beljonne, D., 2D Excitons as Primary Energy Carriers in Organic Crystals: The Case of Oligoacenes. *Physical Review Letters* 104 (20), 4.
16. Huitema, H. E. A.; van Hengstum, B.; van der Eerden, J. P., Simulation of crystal growth from Lennard-Jones solutions. *Journal of Chemical Physics* 1999, 111 (22), 10248-10260.
17. Webber, S. E., The Role of Time-Dependent Measurements in Elucidating Static versus Dynamic Quenching Processes. *Photochemistry and Photobiology* 1997, 65, 33-38.
18. Shetlar, M. D., Nonlinearity in Stern-Volmer Plots I: The case where Two Excited States are Reactive and One is Quenched. *Molecular Photochemistry* 1974, 6 (2), 167-190.
19. Shetlar, M. D., Nonlinearity in Stern-Volmer Plots II: The Case Where Two Excited States are Reactive and Both are Quenched. *Molecular Photochemistry* 1974, 6 (2), 7128-7130.
20. Lide, D., *CRC Handbook of Chemistry and Physics, 88th Edition (CRC Handbook of Chemistry & Physics)*. CRC Press: 2007.

## **Chapter 7. Future Work**

This chapter includes ideas for future experiments related to each of the major projects described in this thesis. These suggestions were developed while analyzing the data collected and during the preparation of this thesis.

### **Chapter 3**

The data presented in Chapter 3 demonstrated an interaction between the spraying distance and the electric field on the diameter of the resultant spray. In those studies the electric field was an uncontrolled variable. Our initial experiments suggested that there is a range of voltages that lead to the formation of a stable cone jet spray for a defined spraying distance and flow rate. To further elucidate the impact of the spraying distance on the spray diameter, studies should be conducted that control the voltage used at each spraying height and flow rate combination. The variables and their contribution to the observed spray diameter must be individually analyzed in order to better understand the cumulative effects of these spraying parameters on the ESD process.

It is suggested that the flow rate and spraying height be fixed and sprays made at various voltages. In this experiment the only variable being changed would be the electric field as defined by the voltage applied to the spraying needle at that spraying distance. The diameter of the sprays made by varying the voltage at the various heights would be recorded to determine the affect of the electric field. A second set of experiments that should be performed would hold the flow rate and electric field constant. The spraying distance could then be modulated to isolate its effect on the spray diameter. Combining the results of the two studies above with the data presented in this thesis could generate a better understanding of the parameters that need to be controlled in order to generate small spray diameters.

The particle morphology has been shown to depend on the solvent identity, spraying distance and flow rate. However, their effects on the sample morphology were only presented as qualitative observations. Further optimization of the AFM is needed to increase the resolution of the images acquired in order to make quantitative measurements of the solid sample droplet height, diameter and size distribution. If this is possible all sprays generated for the above studies should be quantitatively analyzed for the particle size and shape. A method has been developed by our group using ImageJ (<http://rsb.info.nih.gov/ij>) to calculate the size distribution of electrosprayed particles<sup>1</sup>. This method could be used for AFM images or SEM images taken of the sprayed samples. It is suggested that future work to analyze particle morphology and size distributions be made using short spray times (~15-30 seconds). Sprays of this length will not lead to complete coverage of the sprayed area on the surface and will make analysis of the individual particle properties easier.

The morphology of the deposited particles depends on the solubility of the matrix compound in the dissolution solvent. This has been shown in Chapter 4 for DHB sprayed from MeOH and MeCN. It is suggested that the solubility of more matrix compounds be determined in common spraying solvents and also solvent mixtures. Similarly the solution properties of sample solutions (containing matrix, analyte and solvent) need to be explored. Tang<sup>2</sup> has suggested that the dielectric constant of the solution directly impacts the size of the droplets emitted from the spraying cone. He made measurements of the dielectric constant using a set of brass rings with a piece of Teflon tubing separating them. The inner volume of the tube is filled with the solution of interest and the capacitance of the cell was measured in order to determine the dielectric constant<sup>2</sup>. A similar experimental set up could be constructed and used to determine the dielectric constants for matrix solutions. Using these measurements and particle distribution measurements from AFM or SEM images ESD sprays could lead to a better

understanding of the relationship between the initial droplet size and the size and distribution of the dried particles on the surface.

Additionally, initial droplet diameters could be measured using a Phase Doppler Anemometer (PDA), an instrument based on single particle light scattering theory<sup>2</sup>. This technique can determine both the size and velocity of a spherical particle. The PDA analysis would lead to a better understanding of the effects of the initial droplet size on the sprayed diameter. Further, the diameter and thereby the volume of the initial droplets could be measured directly using the PDA instrument. Knowledge of the initial droplet volume and matrix solubility would provide a measurement of the physical amount of matrix in each droplet. If the final solid particle diameter is known and the initial mass of the matrix per droplet can be calculated, QCM studies like those presented in Chapter 5 could provide an estimate of the fraction of dried particles present on the surface being desorbed with each laser spot in the MALDI experiment. This would help to understand the effects of the particle size on the density of the MALDI plume and the resultant signal in the instrument.

## Chapter 4

An obvious extension of the work presented in Chapter 4 would be to repeat the studies done on CHCA and Ang I for additional matrix compounds and a variety of additional analytes to determine if the findings were specific to the system studied or could be applied in a more general case to controlled ESD for MALDI sample preparation. It will also be useful to document the particle morphology of each spray using SEM. This would help to determine if the particle morphology is different for each set of spraying conditions and if the sample morphology is the main variable affecting the analyte signals. Better characterization of the particles will also provide insight into what spraying conditions make a “good” MALDI sample. Further, if solid particles of a particular diameter are found to produce greater ion yields in the

MALDI experiment the combination of the spraying variables leading to the observed morphology could be determined for each unique matrix and analyte combination. This would allow for the consistent production of precise MALDI samples with high sensitivity.

Although the exact cause for increased MALDI sensitivity for samples that are both sprayed for a longer time and from a larger spraying distance were not determined, we suspect that the particle morphology is a key variable. To further test this hypothesis, the sprays resulting in both cracked shells and solid spheres could be made on the surface of a QCM crystal, in the same manner that was done in Chapter 5. The mass desorbed per laser shot of the two samples with differing particle morphologies could then be determined. These studies would provide evidence in support of the hypothesis that the laser energy is less efficiently propagated in cracked spheres as compared to solid particles. This finding would have an impact on nearly all the data acquired in this thesis. Similarly, studies investigating the spraying height and spraying time could be carried out using the QCM. The amount of material desorbed per laser shot from these samples would also help to explain the observed increase in sensitivity as a function of material desorbed and plume density.

Another extension of the work on the controlled ESD technique is development of a novel MALDI target that can be used for high throughput MALDI sample preparations. Such a system would be amenable to the applications of HPLC-MALDI, where fractions of the column eluent are mixed, post column, with matrix solutions and spotted onto MALDI targets<sup>3,4</sup>. Some recent work has been done by coupling nano-HPLC to MALDI analysis<sup>5,6</sup>. The microliter flow rates of the nano-HPLC technique would make it suitable for our controlled ESD sample preparation technique. With this in mind, a novel sample target was created as part of these studies and used to spray in a controlled manner a solution of CHCA and Ang I onto multiple



spots of the new target. An image of the target as sprayed with the sample solution is presented in Figure 7.1.

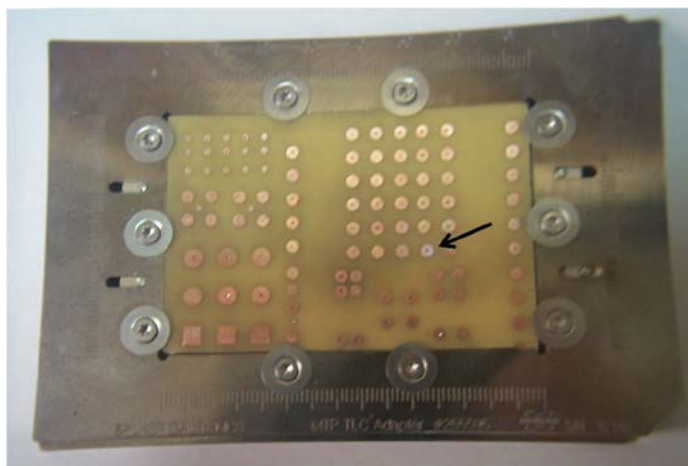


**Figure 7.1: Picture of the novel MALDI target plate set inside of a Bruker MTP TLC Adapter that had been modified to accommodate the target. The arrow indicates the location of a controlled ESD sample preparation.**

The target in Figure 7.1 is a commercially sourced printed circuit board (PCB) that contained various size copper pads printed onto an electrically insulating material that had been electrically connected to the opposite surface using copper vias printed onto the board. The vias are formed as holes in the board and for the application of ESD sample preparation the holes were filled using a lead (Pb) based solder. The metal surfaces, front and back, were then polished to obtain a generally flat surface for spraying and MALDI analysis. Samples were sprayed onto the target by electrically grounding one single metal pad at a time while spraying. The target was mounted in the ESD chamber on a custom built stage that allowed movement in both the x and y axis. The sample shown in Figure 7.1 was sprayed at a height of 20mm and a flow rate of 2.0  $\mu\text{L}/\text{min}$  for 30 seconds. After 30 seconds the stage was translated to a position where no pad was electrically connected to the high voltage supply. In this position no Taylor cone was observed at the needle tip, although the voltage was still being applied to the needle. The stage was then translated to an adjacent metal pad, at which time the Taylor cone was reformed and the sample was deposited onto the electrically connected pad. To examine if the

spray was localized to the electrically connected pad, the target was fitted into a modified Bruker MTP TLC Adapter sampling target and analyzed by on a Bruker Autoflex III MALDI TOFMS. The spectra obtained are presented in Figure 7.2-Figure 7.4.

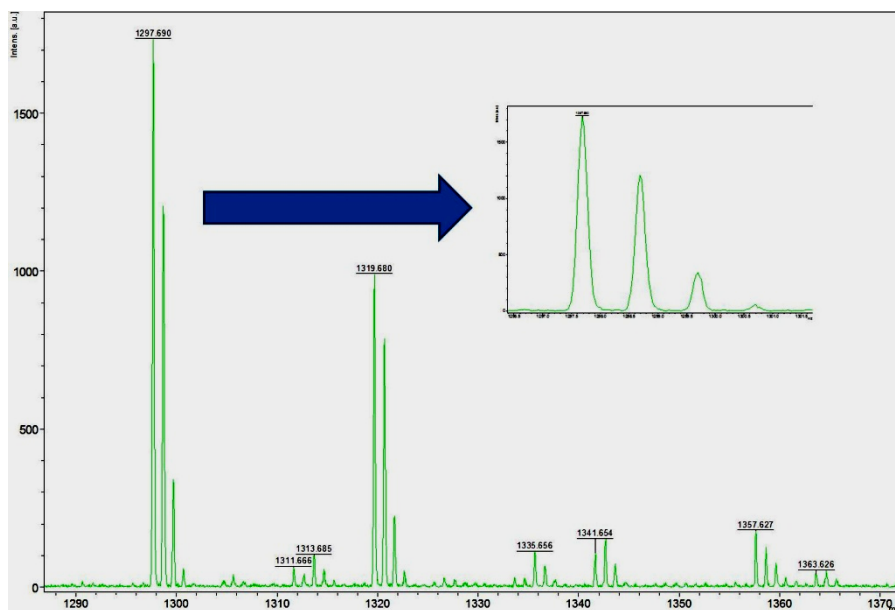


**Figure 7.2:** MALDI TOFMS spectrum of Ang I using CHCA as a matrix from the surface of the novel PCB MALDI sample target. The inset is an expansion of the  $[M + H]^+$  Ang I peak demonstrating the mass resolution.

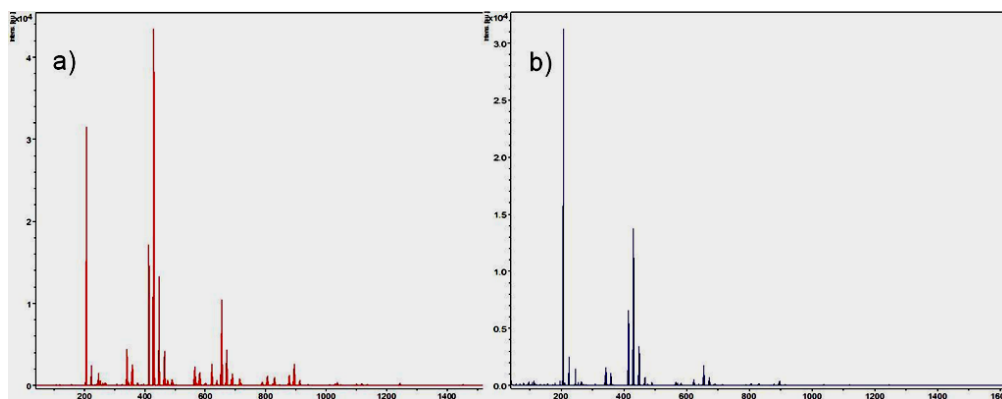


**Figure 7.3:** MALDI TOFMS spectra (a) of a clean metal pad where sample had not been sprayed; and (b) a metal pad directly adjacent to a metal pad that had been sprayed onto using a solution of Ang I and CHCA in MeOH.

The spectrum in Figure 7.2 demonstrates that the MALDI performance of samples sprayed onto the PCB is comparable to that of samples prepared by ESD. The samples were confirmed to have deposited only on the electrically connected metal pad on the PCB surface. Figure 7.3 shows two MALDI spectra, one from a clean metal pad not adjacent to the pad that was being sprayed (Figure 7.3a) and the other from a metal pad adjacent to the pad being sprayed (Figure 7.3b). Both spectra exhibit the same background peaks, and no peaks for Ang I were observed on either pad. Finally, Figure 7.4 illustrates the MALDI mass spectrum that was obtained by firing the laser onto the insulating material of the PCB. The only peak in the spectrum is a characteristic instrument peak.

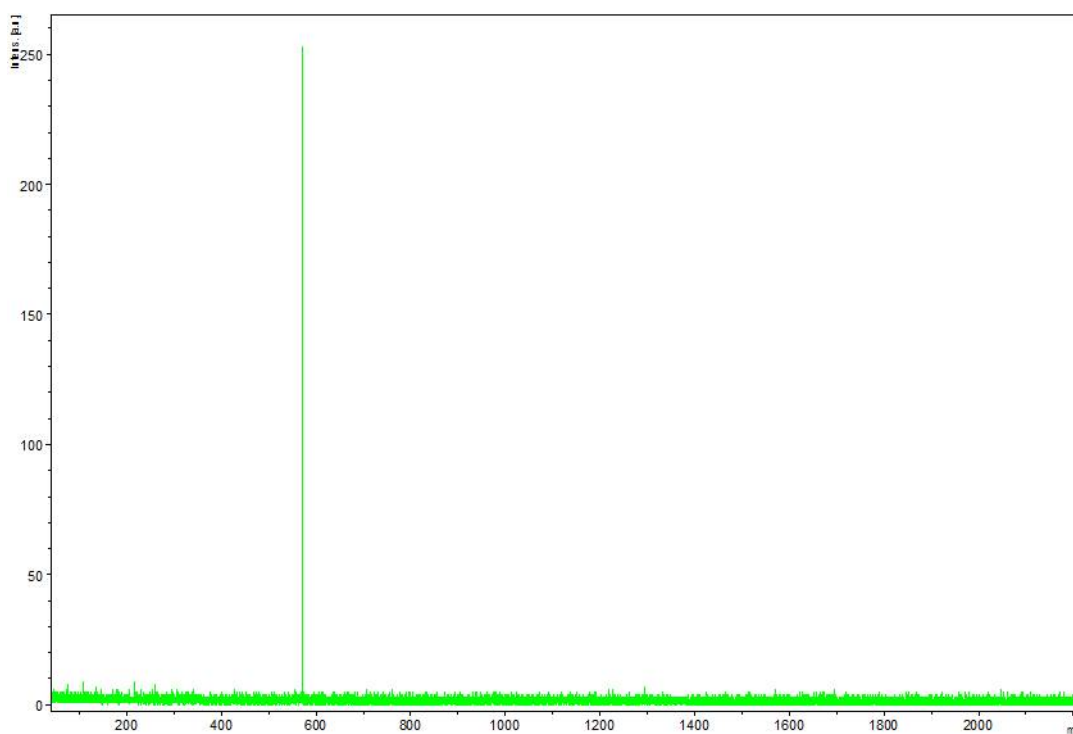


**Figure 7.4: MALDI-TOFMS spectrum taken from the insulating material on the PCB sample target. The peak observed in this spectrum is a system peak of the instrument.**

The data shown in Figure 7.2-Figure 7.4 demonstrate the feasibility of producing isolated homogeneous MALDI samples using the controlled electrospraying technique coupled with a modified PCB MALDI sampling target. Further work needs to be done to identify other suitable substrates for the sample target that would not have to be modified in-house and polished prior to use for controlled ESD. It will also be important to demonstrate that our ESD apparatus can be coupled with an HPLC system and produce controlled ESD samples in real-time from the column eluent.

## Chapter 5

The most obvious extension of the work presented in Chapter 5 would be to perform studies using the QCM on more matrix compounds and with matrix and analyte mixtures. It will be important to determine if the amount of material desorbed at 355nm is greater for all matrixes or a particular subset of matrixes. SEM images of the material sprayed onto the QCM crystal should also be investigated to determine if different particle morphologies affect the amount desorbed at the two wavelengths.

The matrix background mass spectra were collected without careful control of the laser energy being used to produce those spectra. In light of the work presented in Chapter 5 regarding the signal intensity differences between 337 and 355nm laser light, the matrix compounds should be re-examined with care taken to desorb the material with similar fluences at both wavelengths. It is also noted that those matrix samples were prepared using the dried droplet technique. Future studies should use ESD as the sample preparation technique to determine if differences in the observed background ions are obtained between the two sample preparation techniques. The cationization of the matrix molecules would be expected to be naturally enhanced for samples prepared using ESD versus dried droplet due to the better

incorporation of the alkali salts into the electrosprayed samples. Therefore the differences noted with Chapter 5 could be affected and should be studied.

The difference in the cationization of Ang I between 337 and 355nm presented in Chapter 5 is puzzling and at present cannot be explained. It is possible that the energy imparted by the lasers access different energy levels in the matrix molecules. For many matrix molecules ionization would require the absorption of three or more photons at the wavelengths used in this thesis<sup>7</sup>. Vacuum UV spectroscopy (VUV) has been used to probe higher energy photon absorption<sup>8,9</sup>. VUV spectroscopy measurements of the matrix compounds in the solid state should be made to determine if the photon energies of the two wavelengths used overlap with different excited state absorption bands of the matrix molecules. These studies may help to explain the differences in cationization observed in the M/A plots between 337 and 355nm.

## Chapter 6

All samples tested in Chapter 6 were prepared by the controlled ESD method. It would be of interest to determine if the phenomenon observed in these studies would also be observed for other sample preparation techniques, such as the dried droplet method. Kruger et al<sup>10</sup> demonstrated that residual solvents were present in samples prepared by the dried droplet method using NMR. Similar studies should be conducted on the samples prepared by controlled ESD. It should be noted that trapped residual solvent analysis in solids, and particularly crystals, is important in other areas of science as well, most notably the pharmaceutical industry<sup>11</sup>, and numerous strategies for determining the identity and amount are discussed in the literature<sup>12-14</sup>. Samples containing matrix in various solvent mixtures should be sprayed and the resultant deposited material re-dissolved and analyzed for residual solvent content and identity. Obtaining this information for controlled ESD will help to determine if enough solvent is trapped

in the dried particles to interact with matrix molecule in the expanding plume and quench the ion signals observed in the MALDI experiment.

The studies from Chapter 6 should also be repeated and the resultant sprays should be analyzed by SEM to determine the particle morphology of the samples sprayed from different solvent solutions. A direct measurement of the particle size, shape, intactness and distribution may help to explain the observed analyte ion signal. Other characteristics of the drying droplets sprayed from solvent mixtures that can be measured are the analyte solubility in the matrix and the analyte and matrix surface activity in the droplet. The surface activity of a molecule has been shown to impact the ionization of the molecule when interrogated using laser ionization<sup>15</sup>. In the experiments by Jorabachi et al<sup>15</sup>, droplets of differing solvent composition containing different peptides were deposited onto a stainless steel post and irradiated with an infrared laser. They showed that analytes with higher surface activity were preferentially observed as ions in a mass spectrometer<sup>15</sup>. In fact, the molecules with the lowest surface activity were at times not observed until the higher surface activity molecules had been depleted. Measuring the surface activity of matrix compounds and analytes in a similar manner can provide insight into the mechanisms of ionization using ESD samples in the MALDI experiment.

Determining the solubility of MALDI analytes is often challenging due to limited quantities and high cost of those analytes. Typical measurements for solubility are done with large amounts of solute; a review of several solubility determining strategies has been given by our group<sup>1</sup>. Solutes such as Ang I are expected to have low solubility in organic solvents<sup>16</sup>. While we do not expect the peptide analytes to be insoluble at the low concentrations used in a typical MALDI sample preparation, it would still be useful to know the solubility of these analytes.

Additionally, the surface activity of the analytes may affect incorporation with the matrix and therefore the MALDI signal for samples prepared by ESD.

In an attempt to measure the solubility of analytes using relatively small amounts ( $\sim\mu\text{g}$ ) of analyte dissolved in microliter volumes, we have extended the use of the QCM and controlled ESD set up described in Chapter 2. The ESD apparatus is set up in the same manner as shown in Chapter 2 Figure 2.4, with one addition. A PTFE disc 0.25" thick with a diameter equal to that of the QCM crystal holder and 2 mm diameter hole in the center was placed directly on top of the Teflon crystal holder. When ESD was performed the sprayed material was directed through the hole in the PTFE disc and onto the center of the gold coated QCM crystal sensing electrode. Dried particles collecting on the crystal were record. The slope of the line from the QCM data and the flow rate of the electrospray apparatus were used to calculate the amount of solid material deposited per microliter of a known concentration of DHB (0.02M) in MeOH as a feasibility study. The slope calculated for this experiment can be found in Figure 7.5.

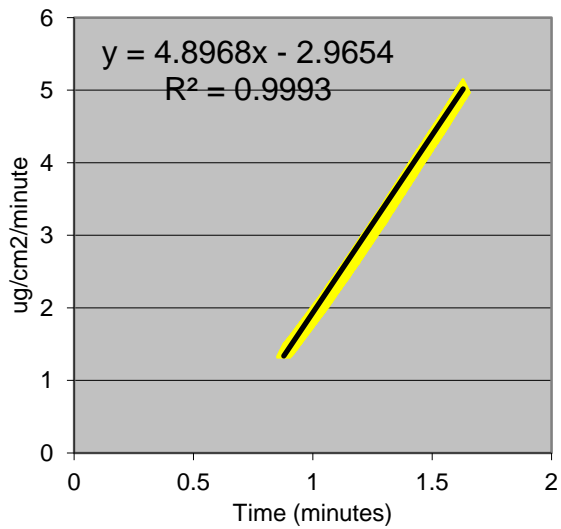


**Figure 7.5:** A plot of the mass collected on the QCM crystal as a function of time. Note that the slope of the line for this plot will have units of  $\mu\text{g}/\text{cm}^2$ .

The quantity of Ang I deposited per minute on the QCM was calculated from the slope of the line given in Figure 7.5. The flow rate was defined by the spraying conditions and therefore the amount of mass deposited per minute divided by the flow rate in  $\mu\text{L}/\text{min}$  of the spray will give the concentration of the solution sprayed in  $\mu\text{g}/\mu\text{L}$ . For this experiment the relative error in the calculated concentration was found to be  $\sim 4\%$ . This example demonstrates the feasibility of making  $\mu\text{g}/\text{mL}$  solubility measurements using a QCM incorporated into the ESD apparatus.

Further studies are needed to define the affects of spraying height, flow rate and voltage of the results obtained for known concentrations. Visually it may be difficult to determine a saturated solution on the microliter scale for some analytes. After the spraying parameters have been investigated a procedure for determining solute saturation in the solvents will need to be developed.



## References

1. Szyszka, R. Exploration of the fundamentals and quantitative applications of matrix assisted laser desorption ionization time-of-flight mass spectrometry (MALDI-TOFMS) in polymer analysis. PhD, Drexel University, Philadelphia, 2012.
2. Tang, K. The electrospray: fundamentals and feasibility of its application to targeted drug delivery by inhalation. PhD, Yale University, New Haven, 1994.
3. Gillmeister, M. P.; Tomiya, N.; Jacobia, S. J.; Lee, Y. C.; Gorfien, S. F.; Betenbaugh, M. J., An HPLC-MALDI MS method for N-glycan analyses using smaller size samples: Application to monitor glycan modulation by medium conditions. *Glycoconjugate Journal* 2009, 26 (9), 1135-1149.
4. Haddock, C. L.; Holtz, B.; Senzer, N.; Nemunaitis, J., Applications of HPLC-MALDI-TOF MS/MS Phosphoproteomic Analysis in Oncological Clinical Diagnostics. *Current Proteomics* 8 (2), 153-167.
5. Kalkhof, S.; Haehn, S.; Ihling, C.; Paulsson, M.; Smyth, N.; Sinz, A., Determination of disulfide bond patterns in laminin beta 1 chain N-terminal domains by nano-high-performance liquid chromatography/matrix-assisted laser desorption/ionization time-of-flight/time-of-flight mass spectrometry. *Rapid Communications in Mass Spectrometry* 2008, 22 (12), 1933-1940.
6. Mao, J. H.; Zhang, Q. Y.; Huang, Q. H.; Chen, Z.; Chen, Q.; Chen, S. J., Identification of protein ubiquitination by IP-2D nano-HPLC-MALDI-TOF-TOF. *Progress in Biochemistry and Biophysics* 2008, 35 (7), 839-847.
7. Knochenmuss, R., Ion formation mechanisms in UV-MALDI. *Analyt* 2006, 131 (9), 966-986.
8. Vicente, A.; Antunes, R.; Almeida, D.; Franco, I. J. A.; Hoffmann, S. V.; Mason, N. J.; Eden, S.; Dufлот, D.; Canneaux, S.; Delwiche, J.; Hubin-Franskin, M. J.; Limao-Vieira, P., Photoabsorption measurements and theoretical calculations of the electronic state spectroscopy of propionic, butyric, and valeric acids. *Physical Chemical and Chemical Reviews* 2009, 11 (27), 5729-5741.
9. Nunes, Y.; Martins, G.; Mason, N. J.; Dufлот, D.; Hoffmann, S. V.; Delwiche, J.; Hubin-Franskin, M. J.; Limao-Vieira, P., Electronic state spectroscopy of methyl formate probed by high resolution VUV photoabsorption, He(I) photoelectron spectroscopy and ab initio calculations. *Physical Chemical and Chemical Reviews* 2010, 12 (48), 15734-15743.
10. Kruger, R.; Pfenninger, A.; Fournier, I.; Gluckmann, M.; Karas, M., Analyte incorporation and ionization in matrix-assisted laser desorption/ionization visualized by pH indicator molecular probes. *Analytical Chemistry* 2001, 73 (24), 5812-5821.
11. Huitema, H. E. A.; van Hengstum, B.; van der Eerden, J. P., Simulation of crystal growth from Lennard-Jones solutions. *Journal of Chemical Physics* 1999, 111 (22), 10248-10260.
12. Yan, H.; Chang, Y. H.; Row, K. H., Multi-Residue Analysis of Four Volatile Organic Solvents in Omeprazole Materials Using Capillary Gas Chromatography. *Asian Journal of Chemistry*. 23 (7), 2961-2964.
13. Cheng, C.; Liu, S. R.; Mueller, B. J.; Yan, Z. M., A generic static headspace gas chromatography method for determination of residual solvents in drug substance. *Journal of Chromatography A* 1217 (41), 6413-6421.
14. Wang, J.; Chatrathi, M. P.; Mulchandani, A.; Chen, W., Capillary electrophoresis microchips for separation and detection of organophosphate nerve agents. *Analytical Chemistry* 2001, 73 (8), 1804-1808.

15. Jorabchi, K.; Smith, L. M., Single Droplet Separations and Surface Partition Coefficient Measurements Using Laser Ablation Mass Spectrometry. *Analytical Chemistry* 2009, *81* (23), 9682-9688.
16. Yoshikawa, H.; Hirano, A.; Arakawa, T.; Shiraki, K., Mechanistic insights into protein precipitation by alcohol. *International Journal of Biologic Macromolecules*. 2012, *50* (3), 865-871.

## Appendix A. List of Abbreviations

**AFM** Atomic Force Microscopy  
**Ang I** angiotensin I  
**CHCA**  $\alpha$ -cyano-4-hydroxycinnamic acid  
**CV** coefficient of variation  
**d** distance  
**Da** daltons  
**DHB** 2,5-dihydroxybenzoic acid  
**DI H<sub>2</sub>O** deionized water  
**E** electric field  
**ESD** electrospray deposition  
**ESPT** excited-state proton transfer  
**HPLC** high pressure liquid chromatography  
**i.d.** inside diameter  
**IPA** isopropyl alcohol  
**IS1** ion source 1  
**IS2** ion source 2  
**KE** kinetic energy  
**L** length  
**LC** liquid chromatography  
**M/A** matrix to analyte ratio  
**m/z** mass to charge ratio  
**MALDI** matrix assisted laser desorption ionization  
**MCP** microchannel plate  
**MeCN** acetonitrile  
**MS** mass spectrometry  
**MW** molecular weight  
**Nd:YAG** neodymium-doped yttrium aluminium garnet  
**Neuro** neurotensin  
**o.d.** outside diameter  
**PDA** Phase Doppler Anemometry  
**PEEK** polyaryletheretherketone  
**PEG** polyethylene glycol  
**PIE** pulsed ion extraction  
**ppm** parts per million  
**S/A** salt to analyte ratio  
**S<sub>0</sub>** singlet ground state energy level  
**S<sub>1</sub>** first excited singlet state energy level  
**SEM** Scanning Electron Microscopy  
**S<sub>n</sub>** singlet excited state energy level  
**SS** stainless steel  
**T<sub>1</sub>** first excited triplet state energy level  
**TFA** trifluoroacetic acid  
**THF** tetrahydrofuran

**TOF** time-of-flight

**UV** ultraviolet

**v** velocity

**VUV** vacuum ultraviolet

**v/v** volume to volume ratio

**z** number of charges on an ion

## Appendix B. Solution and Solid State UV Spectra of Common Matrix Compounds

Spectra for the matrix compounds CHCA, DHB and SA can be found in Chapter 5, all other spectra are contained here.

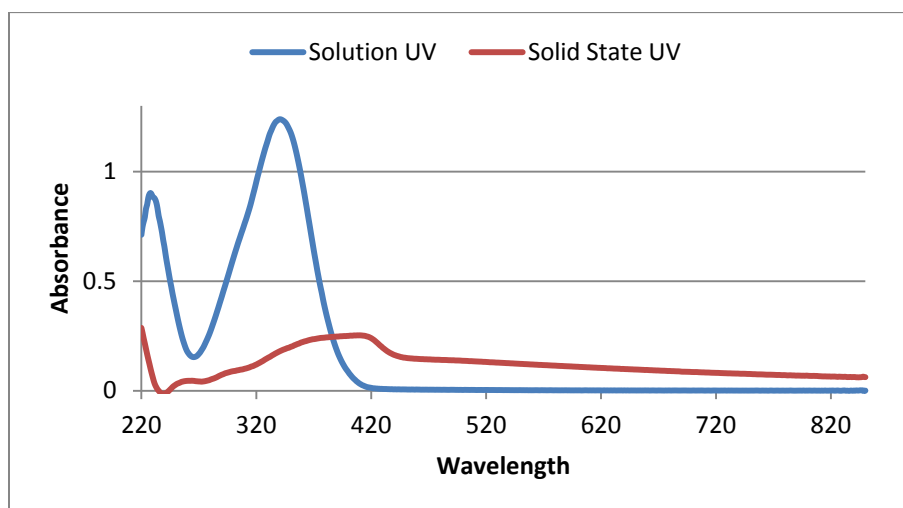


Figure B.1: Solution and Solid State UV-Vis spectra of the matrix compound ANP

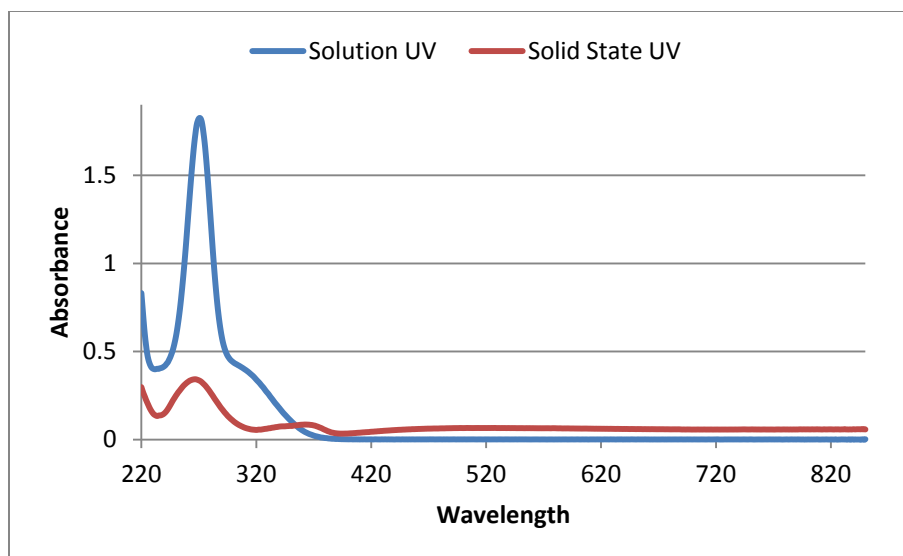


Figure B.2: Solution and Solid State UV-Vis spectra of the matrix compound ATT

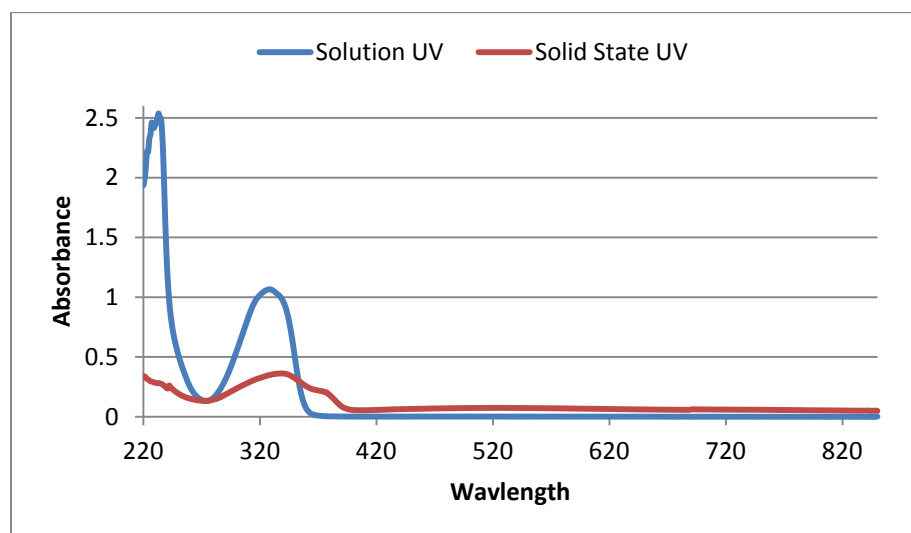


Figure B.3: Solution and Solid State UV-Vis spectra of the matrix compound 1,5-diaminonaphthalene

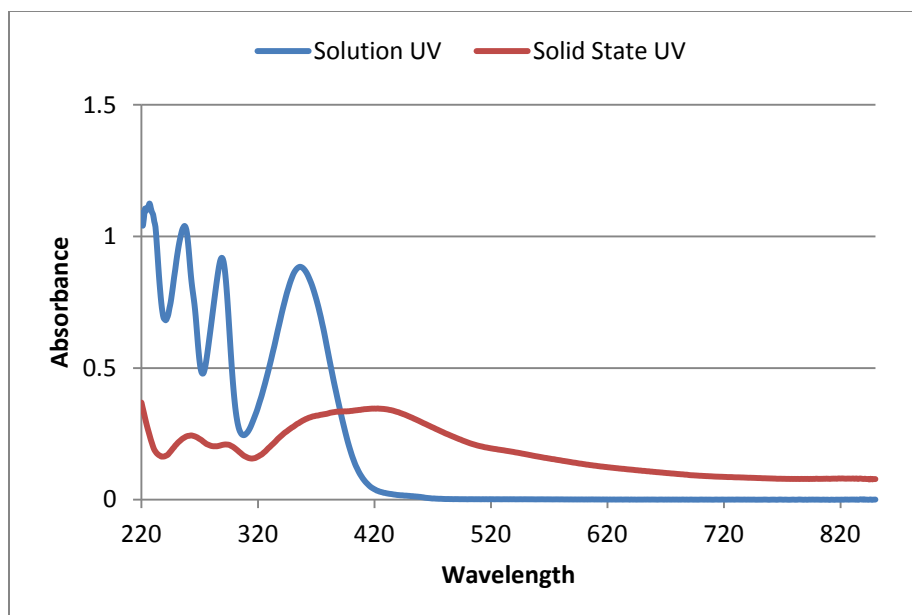


Figure B.4: Solution and Solid State UV-Vis spectra of the matrix compound dithranol

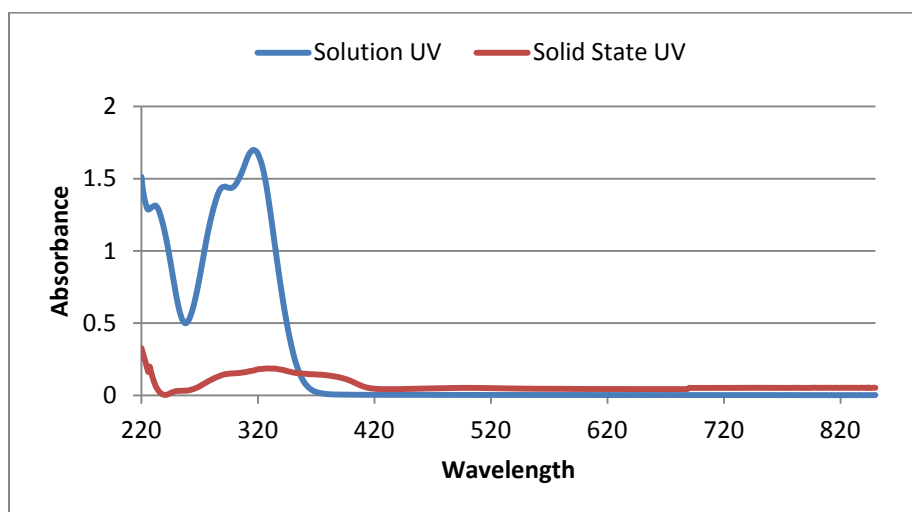


Figure B.5: Solution and Solid State UV-Vis spectra of the matrix compound FA

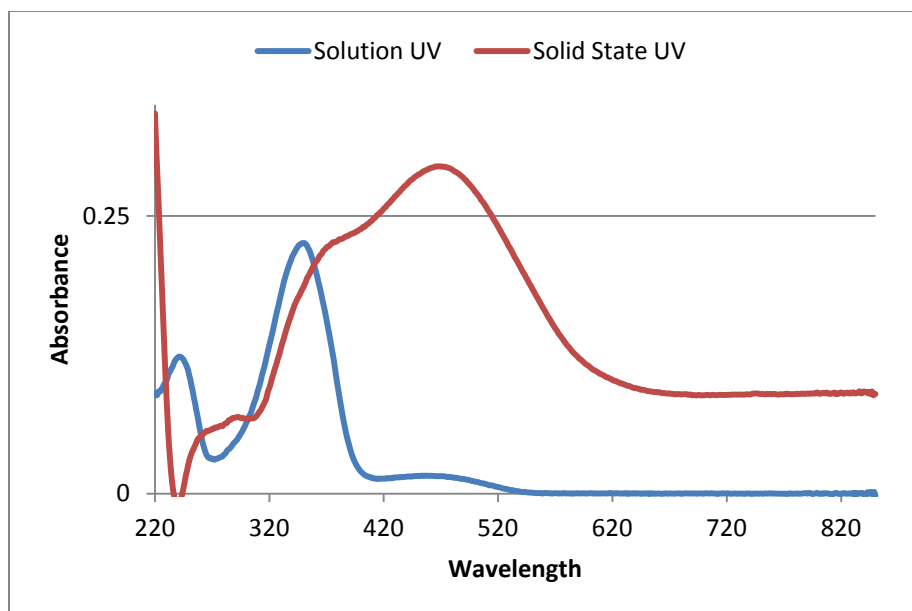


Figure B.6: Solution and Solid State UV-Vis spectra of the matrix compound HABA

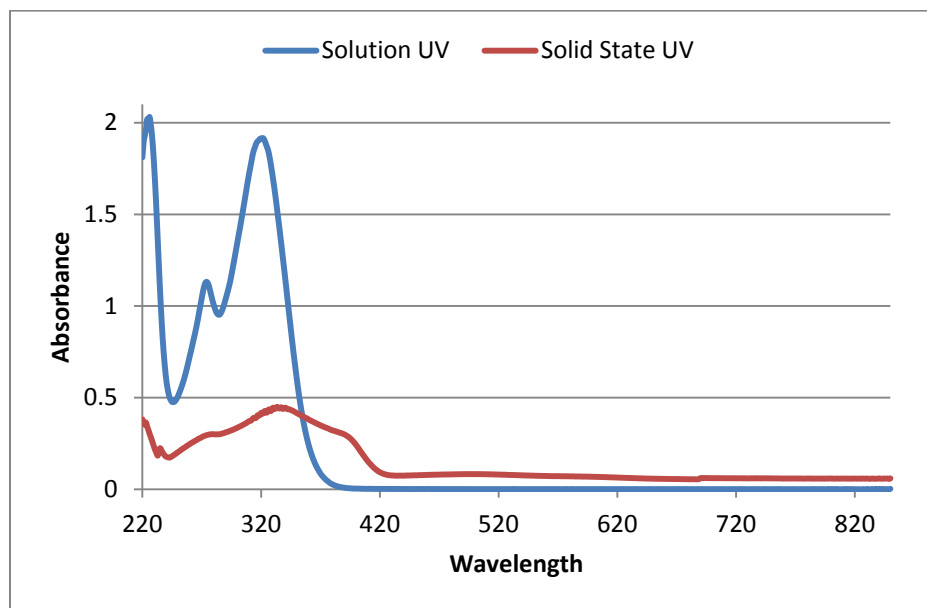


Figure B.7: Solution and Solid State UV-Vis spectra of the matrix compound IAA



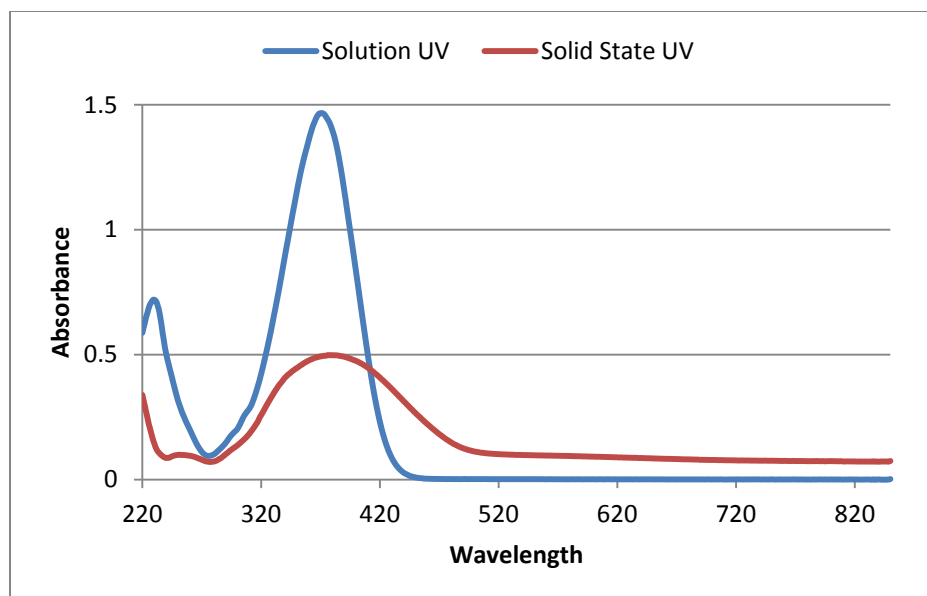


Figure B.8: Solution and Solid State UV-Vis spectra of the matrix compound 4-NA

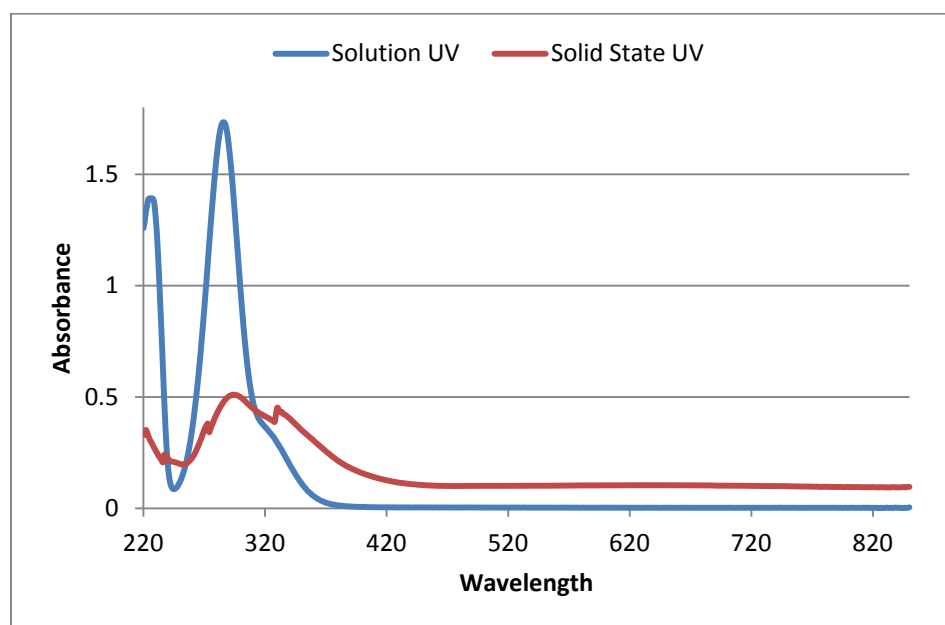


Figure B.9: Solution and Solid State UV-Vis spectra of the matrix compound THAP

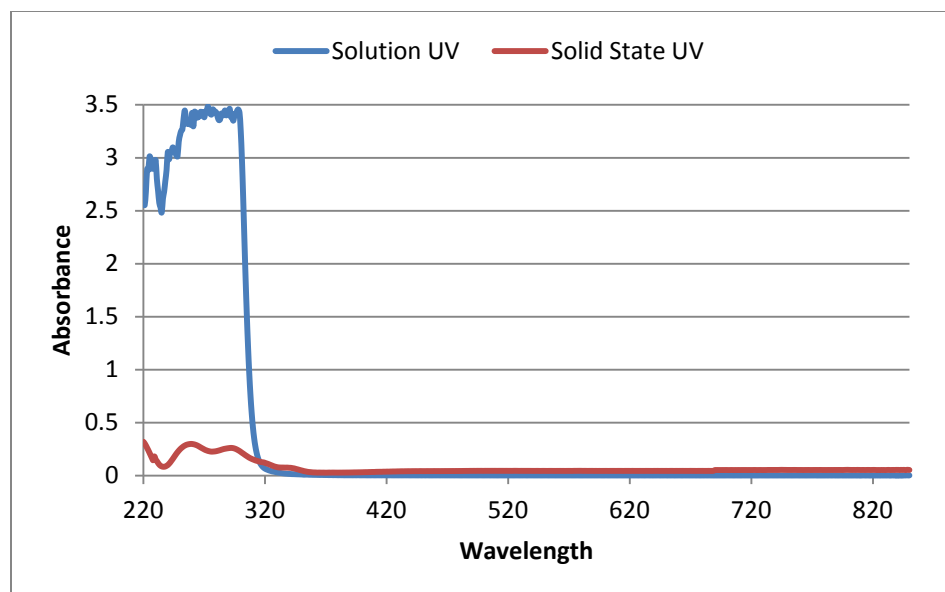


Figure B.10: Solution and Solid State UV-Vis spectra of the matrix compound vanillic acid

## VITA

### Jonathan R. Haulenbeek

**Date and Place of Birth:** October 7; Langhorne, Pennsylvania

**Undergraduate Education:**

1999-2003 Southampton College, Long Island University, New York

Degree: BS Chemistry, BS Cell and Molecular Biology

**Graduate Education:**

2007-2012 Drexel University, Philadelphia, Pennsylvania

Degree: Ph.D. Analytical Chemistry

**Publications/Presentations:**

Haulenbeek, J., Owens, K.G., "Probing the Effect of Wavelength on Matrix Compounds in the UV-MALDI-TOFMS Experiment.", Poster ASMS 2011.

Haulenbeek, J., Owens, K.G., "System and Method for Controlled Electrospray Deposition", PCT International Application No. PCT/US11/37918

Haulenbeek, J., Owens, K. G., "High Intra- and Inter-Sample Precision Obtained for Electrospray Deposited MALDI-TOFMS Samples of Controlled Spot Size.", Poster at ASMS 2010.

Mahan, A., Owens, K.G., Knochenmus, R., Haulenbeek, J., Holcomb, A., "Positive and Negative Ion Ratios of Peptides in MALDI-TOFMS: The Role of Acid/Base Properties of Matrices and Analytes.", Poster at ASMS 2010

Haulenbeek, J., Huang, M., Ray, C., Wethman, R., Wasylyk, J., "Use of Raman for API Processing Controls: Development, Implementation and Validation.", Presentation at FACSS 2007, # 122.

**Professional Experience:**

2003 – Present, Bristol-Myers Squibb Company

Research Investigator

**Member of the American Society for Mass Spectrometry (2005-present)**

